COLLOIDAL TRANSPORT IN LIQUID CRYSTALS AND CONNECTIONS BETWEEN RHEOLOGY AND DYNAMICS OF SOFT DISORDERED SOLIDS

by

Kui Chen

A dissertation submitted to Johns Hopkins University in conformity with the requirements for the degree of Doctor of Philosophy

Baltimore, Maryland

December, 2016

Abstract

In this thesis, I report experimental studies on soft matter physics. Two fields were investigated. The first part of the thesis concerns colloidal transport within liquid crystals. When a colloidal particle translates through a liquid crystal under an external force, its mobility is not only affected by viscous forces, but also by the elastic properties of the liquid crystal. For example, the anisotropic viscous and elastic interaction in the liquid crystals can make the mobility highly dependent on the direction of motion. To explore such hydrodynamics, I have performed a series of experiments examining the transport behavior of colloidal particles suspended in liquid crystals with spatially periodic order. In Chapter 3, I describe experiments of colloids transport in cholesteric finger textures. When a cholesteric liquid crystal is confined within a homeotropic cell, the helical alignment is distorted into a finger texture, which includes a periodic array of disclinations. Interactions between colloids and the defects affect the particle translation. Under an external constant driving force, such interactions, along with the anisotropic viscosity of the cholesteric, lead to highly different particle mobility along the directions parallel and perpendicular to the cholesteric pitch. We characterized experimentally this mobility, which included stick-slip motion, a built a model that accounts for it quantitatively. In Chapter 4, I report investigations of colloidal transport within nematic liquid crystals within mircrofluidic arrays of obstacles. In contrast with the behavior in isotropic liquids, the interaction between the particles and obstacles mediated by the elasticity of the liquid crystal, along with the spatially varying anisotropic viscosity of the

nematic, contributes to the mobility. A quantitative analysis distinguishes the viscous and elastic contributions to the mobility. In addition, the directional locking phenomenon was has been observed previously in isotropic liquids is shown to be altered by the liquid crystal forces, indicating a mechanism for particle separation technology.

My research in the second field is focused on the nonlinear rheology and shear-induced dynamics of soft disordered solids. Nonlinear viscoelasticity is widely observed in these systems. In particular, when an applied stress exceeds the solid's elastic limit, the solid yields, and irreversible changes to the material's structure at the nanoscale to microscale occur. As described in Chapter 5, I have applied X-ray photon correlation spectroscopy (XPCS) to interrogate how shear-induced microscopic structural dynamics connects with the macroscopic deformation and flow properties in a set of soft disordered solids including concentrated nanocolloidal gels.

This work was conducted under the supervision of Prof. Robert L. Leheny. The author also acknowledges Prof. Daniel H. Reich for his role as co-advisor.

Acknowledgements

I would like to thank Prof. Leheny and Prof. Reich for their gracious mentorship, advice and help over the past years as I worked toward completing my Ph.D. I would not have finished without their spirited and creative guide. I also want to thank former graduate students in Professor Leheny's lab, Joel Rovner and Dan Allan. They showed great patience in helping me obtain the needed experimental skills and data analysis expertise during my first several years in the lab. I would like to thank all the other team members from Prof. Leheny's group and Prof. Reich's group, including David Rivas, Linnea Metcalf, Olivia Gebhardt, Bilyana Tzolova, Ramona Mhanna, Yu Shi and Prasenjit Bose. Without their enormous help, my research would not have gone so well. Prof. Harden and Michael Rogers from University of Ottawa and Suresh Narayanan from Argonne National Lab provided much guidance and instruction in helping me with the XPCS experiments, which I appreciate greatly. And last but not least, I really want to thank my wife, Weixu Chen. Her support has been the key factor for me to reach the successful end of this great journey.

The research in this thesis was funded in part by the National Science Foundation.

Contents

List of Tables

List of Figures

Chapter 1

Introduction

The research described in this thesis deals with two major areas of soft matter physics. The first is liquid crystals. Specifically, as part of my thesis, I have performed a series of experiments examining the transport behavior of colloidal particles suspended in liquid crystals. The experiments include investigations of colloidal transport in cholesteric finger textures described in Chapter 3 and studies of microspheres translating in nematics within obstacle arrays described in Chapter 4. The second area of my research has been soft glassy materials. My research in this area has focused on the nonlinear rheology of soft disordered solids. In particular, as described in Chapter 5, I have applied advanced coherent x-ray scattering techniques to interrogate how shear-induced microscopic structural dynamics connects with the macroscopic deformation and flow properties in these materials. In this chapter, I provide a general introduction to both topics, focusing primarily on the aspects of each that are relevant to my research.

1.1 Liquid Crystals

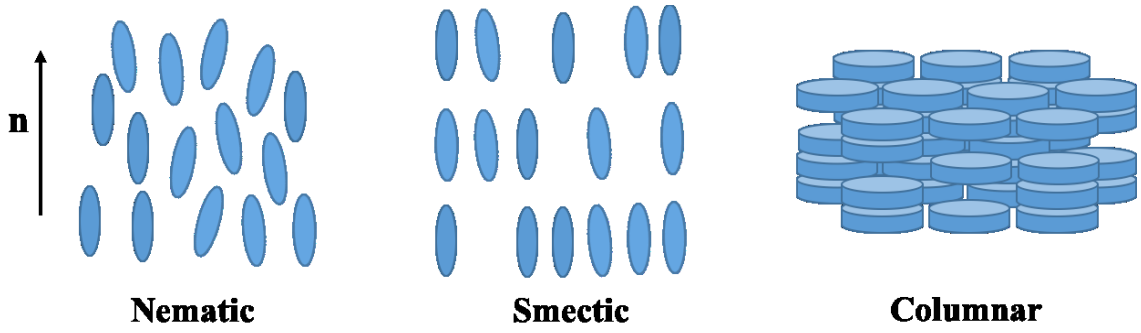

Figure 1.1: Schematics of three phases of liquid crystals. The director ***n*** representing the orientation of the orientational order is shown with the nematic. Rod-like molecules are used to form the nematic and smectic phases, while disk-shape molecules form the columnar phase.

Liquid crystals are materials that can exist in states that have mechanical and symmetry properties between those of a liquid and those of a crystal. While crystals have both three-dimensional long-range positional and orientational order, and liquids have only short-range order, liquid crystal phases can possess orientational order without long-range positional order, or with positional order in only one or two directions. Typically, liquid crystals are fluids composed of aspherical molecules, known as mesogens, and the long-range orientational order in the material is associated with the alignment of the molecules. For instance, mesogens with rod-like or disk-like shapes can form liquid crystal phases. Examples of the molecular arrangements in common liquid crystal phases are shown in Fig. 1.1. These include the nematic phase, which has only orientational order, the smectic phase, which has positional order in one direction, and the columnar phase, which has positional order in two directions [1].

Based on the thermodynamic variable that controls their phase behavior, a liquid crystal (LC) can be described as thermotropic or lyotropic. Thermotropic LCs exhibit phase transitions controlled by temperature, while lyotropic phase behavior is controlled

by the concentration of the mesogens in a solvent. In my research, I will focus on thermotropic liquid crystals, especially on the elongated organic molecule 4-cyano-4'-pentylbiphenyl (5CB), whose chemical structure is shown in Fig. 1.2. The 5CB molecule is about 2 nm long. 5CB undergoes a phase transition from a crystalline state to a nematic state at 18 °C and transitions from a nematic to an isotropic state at 35 °C [2].

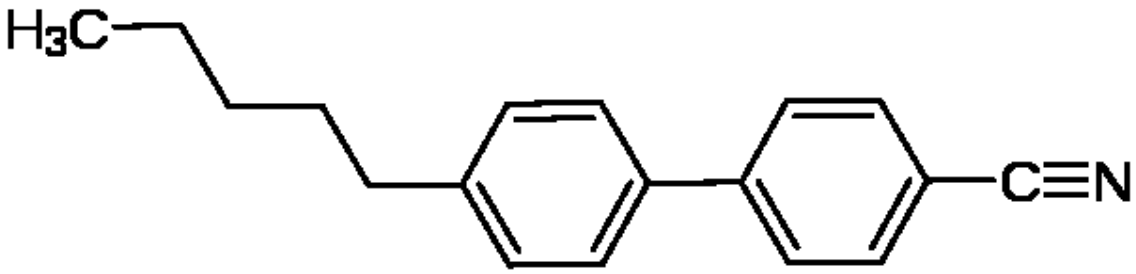

Figure 1.2: The chemical structure of the 5CB molecule.

1.1.1 Nematic Phase

In a nematic phase, the average direction of the liquid crystal molecules in a local volume defines the local director, labeled by a unit vector $\boldsymbol{n}$. The ability to define $\boldsymbol{n}$ reflects the orientional order in the fluid. In a nematic, the alignment is invariant to the ends of the mesogens (e.g., in nematic 5CB, the molecules align with the cyano groups along $\boldsymbol{n}$ and away from $\boldsymbol{n}$ with equal probability). This symmetry makes $\boldsymbol{n}$ and $-\boldsymbol{n}$ indistinguishable. Therefore, nematic order has no dipolar component, and proper description of the orientational ordering requires a traceless second rank tensor $Q_{\alpha\beta}$ [3]:

$$Q_{\alpha\beta} = \langle n_\alpha n_\beta \rangle - \frac{1}{3}\delta_{\alpha\beta} \tag{1.1}$$

where α, β are the indices specifying the Cartesian coordinates x, y, z, and $\langle \cdots \rangle$ means an average over volume. According to this symmetry, if we choose the z direction along the orientation direction, then

$$Q = \begin{pmatrix} -\frac{1}{2}S & 0 & 0 \\ 0 & -\frac{1}{2}S & 0 \\ 0 & 0 & S \end{pmatrix} \tag{1.2}$$

where we introduce a scalar S, which is the amplitude of the nematic order parameter. As a matter of fact, for uniaxial mesogens, such as 5CB, Q and thus S can completely describe the ordering [1]. In the isotropic phase, S is zero; while in a solid phase, $S = \frac{2}{3}$. Since the isotropic-nematic transition is weakly first order, S changes discontinuously at the transition [1, 4-6]. For example, S jumps from 0 to about 0.3 at the isotropic to nematic transition of 5CB [7,8].

1.1.2 Cholesteric Phase

Cholesteric liquid crystals (CLCs) are a special kind of nematic liquid crystal with both long-range orientational order and broken translational symmetry. Locally, a cholesteric is very similar to a nematic. However, the direction of the nematic order, also labeled with director $\boldsymbol{n}$, forms a helical structure in space, as depicted in Fig. 1.3(a). If the z-axis is the helical axis, then the director can be expressed as:

$$n_x = \cos(z/p + \phi) \tag{1.3$\boldsymbol{a}$}$$

$$n_z = \sin(z/p + \phi) \tag{1.3$\boldsymbol{b}$}$$

$$n_z = 0 \tag{1.3$\boldsymbol{c}$}$$

where ϕ is an arbitrary phase and p is called the pitch, representing the spatial period. To be more accurate, the pitch $\boldsymbol{p}$ is a vector, whose direction is the chiral axis and whose magnitude is the period [1]. Such alignment of molecules in space introduces strong anisotropy in the physical properties between the directions parallel to the pitch and perpendicular to pitch, which will be discussed more in Chapter 3.

When we observe a cholesteric liquid crystal placed between two plates with the helicoid axis lying in the plane of the cell, the twist of the director is revealed as a periodic texture [1,9]. Such a structure is called a finger texture, and an example is shown in Fig. 1.3(b). We will investigate the behavior of colloids in finger textures.

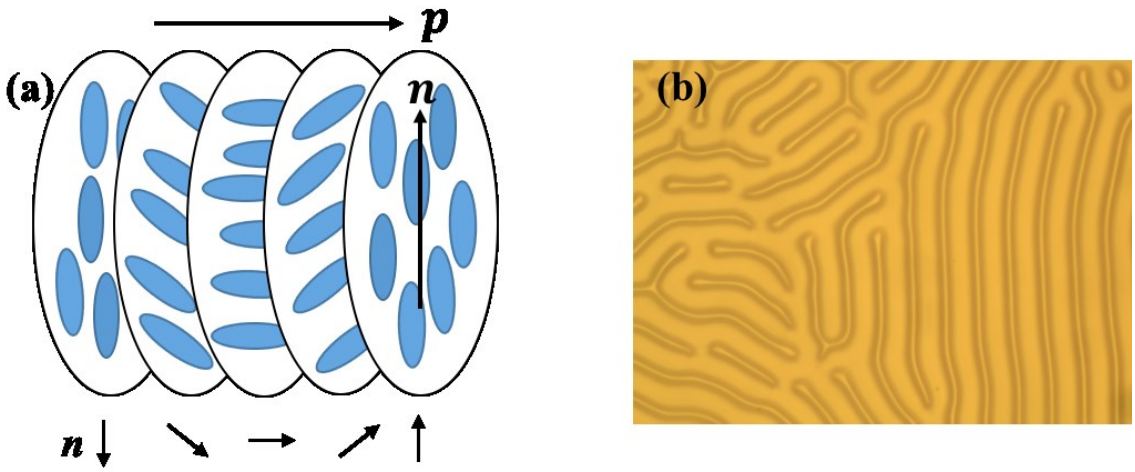

Figure 1.3: (a) A schematic diagram illustrating the director field within cholesteric liquid crystals. (b) Microscopy image of a cholesteric finger texture.

1.1.3 Elastic Energy

In a nematic liquid crystal, distortion of the orientational order, which makes the director a function of position, $\boldsymbol{n}(\boldsymbol{r})$, will lead to elastic energy stored within the fluid. Such deformation of relative orientations away from equilibrium is called curvature strains, and the restoring forces opposing these deformations are called curvature stresses.

Assuming a uniaxial liquid crystal, at position $\boldsymbol{r}$ we can introduce a local right-handed Cartesian coordinate system, with z along $\boldsymbol{n}(\boldsymbol{r})$. Then, there are six components of curvature:

$$\text{Splay: } s_1 = \partial n_z/\partial x\,, s_2 = \partial n_y/\partial y \tag{1.4}$$

$$\text{Twist: } t_1 = -\partial n_y/\partial x\,, t_2 = \partial n_z/\partial y \tag{1.5}$$

$$\text{Bend: } s_1 = \partial n_x/\partial z\,, b_2 = \partial n_y/\partial z \tag{1.6}$$

The free energy density f can be expanded in terms of these six curvature strains:

$$f = \sum_{i=1}^{6} k_i a_i + 1/2 \sum_{i,j=1}^{6} k_{ij} a_i a_j \tag{1.7}$$

where k_i and k_{ij} are the curvature elastic constants, and for a_i we have:

$$a_1 = s_1, a_2 = t_2, a_3 = b_1, a_4 = -t_1, a_5 = s_2, a_6 = b_2 \tag{1.8}$$

The symmetry of the nematic introduces some constraints on f: rotation about the z axis makes no change in the form of f. This leads to simplification of f,

$$f = \frac{1}{2} k_{11} (\nabla \cdot n - s_0)^2 + \frac{1}{2} k_{22} (n \cdot \nabla \times \mathrm{n} + t_0)^2 + \frac{1}{2} k_{33} (n \cdot \nabla n)^2 - k_{12} (\nabla \cdot n)(\mathrm{n} \cdot \nabla \times \mathrm{n}) \tag{1.9}$$

Eq (1.9) is called the Frank free energy density [1,10,11]. The four terms correspond to the four types of deformations found in liquid crystals: splay, twist, bend, and saddle-splay [12], depicted in Fig. 1.4. Under most situations, we do not consider the saddle-splay term, because it can be written as a complete derivative and expressed as a surface energy. Therefore, we ignore this term when focusing on the director field configuration within the bulk. In nematics, $f = \frac{1}{2} k_{11} (\nabla \cdot n)^2 + \frac{1}{2} k_{22} (n \cdot \nabla \times n)^2 + \frac{1}{2} k_{33} (n \cdot \nabla n)^2$,

with $s_0 = 0, t_0 = 0$. In cholesteric liquid crystals, $f = \frac{1}{2}k_{11}(\nabla \cdot n)^2 + \frac{1}{2}k_{22}(n \cdot \nabla \times \mathrm{n} + t_0)^2 + \frac{1}{2}k_{33}(n \cdot \nabla n)^2$, with zero s_0 and nonzero $t_0 = 2\pi/p$, where p is the pitch.

The elastic constants k_{11}, k_{22}, and k_{33} are important parameters for liquid crystals. For 5CB, the typical values are on the order of pN [10,13]. In most cases, these three values are similar in magnitude, and a "one-elastic-constant approximation" is often applied under the approximation that all elastic constants are equal. Within this approximation, the Frank free energy of a nematic is simplified to:

$$f = \frac{1}{2}K((\nabla \cdot n)^2 + (\nabla \times \mathrm{n})^2) \tag{1.10}$$

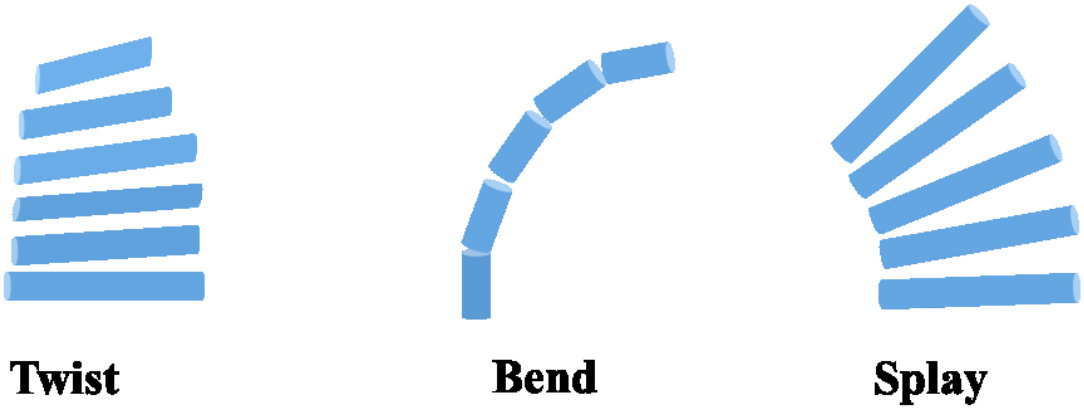

Figure 1.4: Three types of elastic deformations of a nematics: twist, bend and splay. The blue rods represent the local orientation of the director.

1.1.4 Anchoring

The orientation of the director is sensitive to interactions with bounding surfaces, and surface anchoring is a widely used technique to control the alignment of liquid crystals within the bulk. These interactions can be incorporated into the free energy of the liquid crystal though an anchoring energy contribution:

$$F_s = \int_s \frac{1}{2}(W_1 \sin^2(\theta - \theta_0) + W_2 \cos^2(\varphi - \varphi_0))\, \mathrm{d}s \qquad (1.11)$$

where θ and φ are the polar and azimuthal angle of the director with respect to the surface, θ_0 and φ_0 correspond to the minimum-energy orientation, and W_1 and W_2 are the anchoring strengths [14]. The integral is over the whole surface of the fluid. Based on the values of the anchoring strength, one can distinguish weak anchoring and strong anchoring. For strong anchoring, $W_1 > 10^{-4}\mathrm{J/m^2}$ and $W_2 > 10^{-3}\mathrm{J/m^2}$, and for weak anchoring $W_1 < 10^{-6}\mathrm{J/m^2}$ and $W_2 < 10^{-4}\mathrm{J/m^2}$. With strong anchoring, the fluid will incorporate even severe elastic distortions to keep the mesogens near the surface tightly constrained to the minimum energy orientation, while with weak anchoring, the alignment of mesogens will be decided by both the anchoring energy and bulk contributions, including importantly the Frank energy [15]. In addition, based on the orientation of the mesogens near a surface, the anchoring condition can also be divided into three types: planar (mesogens align parallel to surface), homeotropic (mesogens align perpendicular to surface) and titled (mesogens align in an oblique angle to surface), as shown in seen in Fig. 1.5.

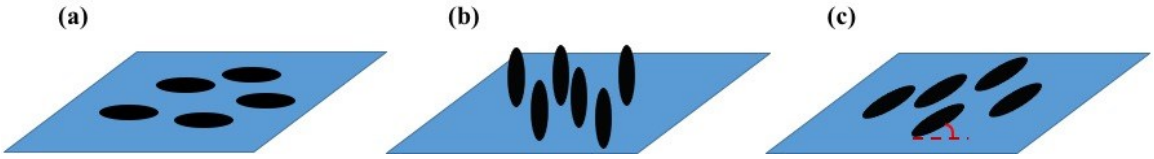

Figure 1.5: A schematic diagram illustrating the three anchoring configurations of liquid crystals molecules at a boundary. (a) planar anchoring. Liquid crystal molecules are parallel to the surface. (b) homeotropic anchoring. Molecules are perpendicular to the surface. (c) titled anchoring. Molecules are at an oblique angle with the surface.

1.1.5 Defects in Nematics and Cholesterics

When there exist regions within a liquid crystal where the director field cannot be well defined, topological defects form [1,16,17]. Defects can take the form of points, lines, or walls, as shown in Fig. 1.6. Because the states $\boldsymbol{n}$ and $-\boldsymbol{n}$ are indistinguishable in nematics, the topological charge of defects can be integers or half-integers. For point defect, only integer defects are observed in experiment. Line disclinations, with strength of +1/2 and -1/2, are also often commonly observed experimentally. When the director is constrained to be spatially varying, for example by anchoring conditions, defects can appear to minimize the free energy. Consider, for example, the two-dimensional cross-section of a line defect and describe the system using an XY model. When the director field lies in a plane, as it does in this situation, it can be parameterized with a single variable $\varphi(x, y)$ as $n_x = \cos\varphi(x, y)$ and $n_y = \sin\varphi(x, y)$. Under a one-elastic-constant approximation, the Frank free energy density then has the simple form:

$$f = \frac{1}{2}K(\nabla\varphi)^2 \tag{1.12}$$

Minimizing f is thus equivalent to solving Laplace's equation: $\nabla^2\varphi = 0$. The nontrivial solution is $\varphi(x, y) = N \cdot arctan\left(\frac{y}{x}\right) + \varphi_0$, where N represents the defect's strength (or topological charge) and φ_0 is a constant. Near the origin, the gradient of φ diverges, thus causing the Frank energy density to blow up. To avoid this divergence, the nematic can instead transform to the isotropic phase within a radius of the origin, thereby substituting the Frank energy cost with the free energy cost of melting. To calculate the total free energy, we should thus limit the integral of the Frank free energy density to outside a small circle with radius r_c, which is often called the defect core, and add the contributsion to melting the volume within this radius [1, 17-19]. For example, for our cross section around the line defect, the total energy is

$$F_d = L[\frac{1}{2}\int_{r_c}^{R}\int_{0}^{2\pi} K(\nabla\varphi)^2\, r dr d\theta + \sigma_c \pi {r_c}^2]$$

$$= \pi K L N^2 \ln\left(\frac{R}{r_c}\right) + \pi\sigma_c {r_c}^2 L \qquad (1.13)$$

where σ_c is the energy density of melting. Here, we assume that the length of the defect line is L, and the bulk dimension is R. From Eq (1.13), we find that the free energy consists of two parts: the Frank free energy and defect's core energy. On one side, the Frank free energy term is proportional to the square of defect's charge. Therefore, defects with small charges are preferred. For example, a +1 line disclination would split into two +1/2 line disclinations to reach a lower-energy configuration [17]. On the other side, to minimize the total energy, r_c is approximately $\sqrt{\frac{K}{\sigma_c}}$, which does not depends on the system size R. A similar analysis can also be made for point defects.

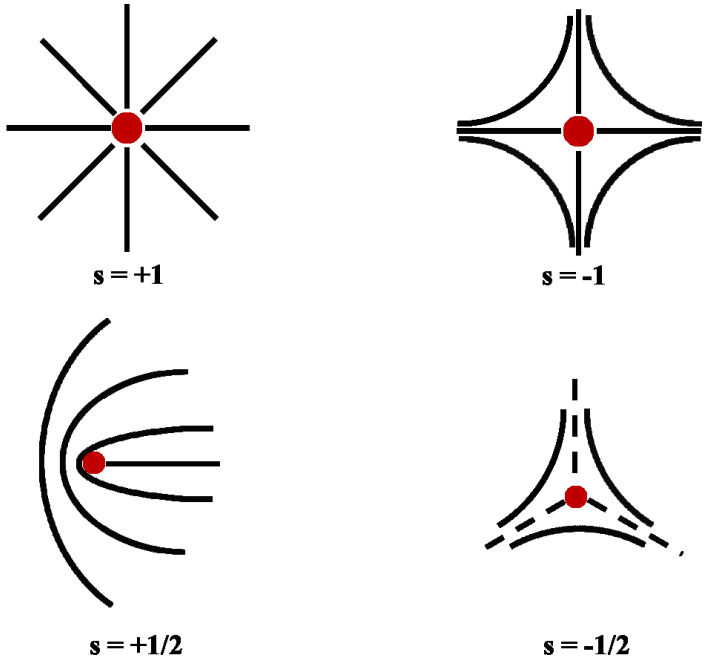

Figure 1.6: A schematic diagram of point defects and line defects. The top two configurations are point defects, with +1 and -1 charge. The bottom two are line defects, with +1/2 and -1/2 charge. For line defects, the diagram only shows their cross section.

1.1.6 Colloids in Liquid Crystals

A major goal of my research has been to understand the behavior of colloidal particles suspended in liquid crystals. The boundary conditions created by the anchoring of the director at the surface of a colloid will in general introduce distortions and defects in the director field, with corresponding costs in the free energy [20-23]. The minimization of these energy costs can, in turn, engender forces on the particles that lead to striking and unexpected results, such as the levitation of particles in opposition to gravity and the formation of stable colloidal crystals [24].

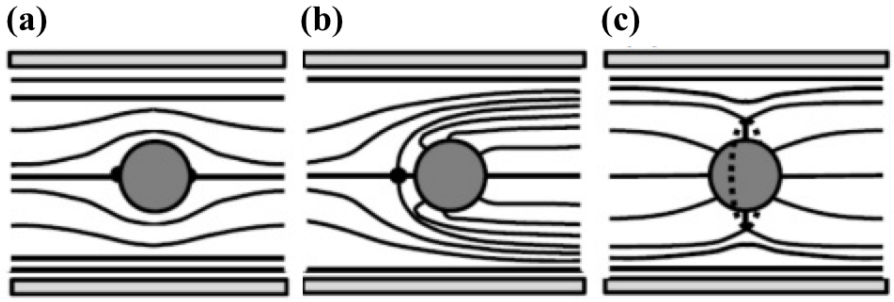

Figure 1.7: A schematic diagram of three director field configurations around a colloidal sphere. (a) a sphere with planar anchoring. Two +1 point defects known as boojums lie on the north and south pole of the sphere (b) A hedgehog around a homeotropic sphere. The -1 point defect lies in front of sphere about $1.3R$ away from the center. (c) Saturn ring around a homeotropic sphere. The ring is a -1/2 defect line. (From Stark, 2001 [20])

For example, consider a spherical particle in a nematic liquid crystal; studies have shown that different anchoring conditions on the particle surface lead to at least three different possible director field configurations, as shown in Fig. 1.7. In Fig. 1.7(a), the sphere surface imposes a planar anchoring condition. As a result, two +1 point defects called boojums are located at the north and south poles of the sphere [23]. However, when the sphere surface imposes a homeotropic anchoring condition, there exist two possible configurations [20]. In Fig. 1.7(b), the defect structure consists of one -1 point

defect, called a hedgehog, that forms about $\sim 1.3R$ away from the center of the sphere, where R is the sphere radius. Fig. 1.7(c) displays an alternative solution to the director field around the sphere with homeotropic anchoring in which a -1/2 "Saturn ring" line defect encircles the sphere. Whether the dipole configuration with the hedgehog defect or the configuration with the Saturn ring, which has quadrupolar symmetry, is the minimum energy configuration depends on the sphere size, the anchoring strength, and the elastic constant of liquid crystals. For example, Saturn rings tend to form around small size spheres and under conditions of weak anchoring.

1.1.7 Viscosity in Liquid Crystals

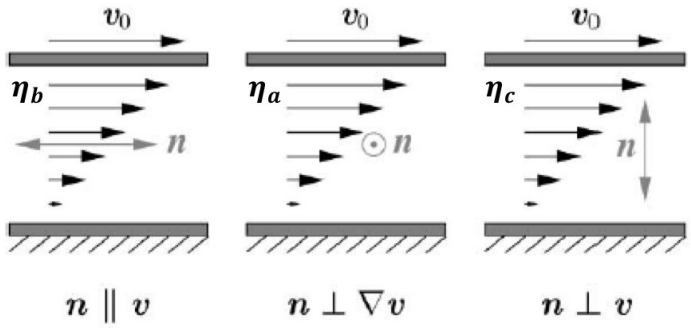

Figure 1.8: A schematic diagram of a Miesowicz experiment. Liquid crystal is sheared between two plates, with the top plate moving at constant velocity $\boldsymbol{v_0}$ and the bottom plate stationary. The director field $\boldsymbol{n}$ is uniform between the plates. The flow velocity gradient is constant and in the vertical direction. (from Stark, 2001 [20])

A particular interest in my work has been to understand the dynamic behavior of colloids moving in liquid crystals. In this case, we must consider not only the storage of elastic energy but also the hydrodynamic forces and the corresponding dissipation of energy through viscous drag. The shear viscosity of a fluid is defined as a measure of its

resistance to flow by shear stress. Specifically, the viscosity is given by the ratio of the shear stress to the strain rate. If the viscosity is independent of the stress, the fluid is called Newtonian, otherwise, it is called non-Newtonian. At high flow rates, the director in a nematic can be altered due to the shear stresses, which leads to non-Newtonian behavior. The importance of such effects is parameterized by the Ericksen number, which is the ratio of the elastic to viscous forces and is explained in more detail below. At small Ericksen number, the viscosity of liquid crystals such as 5CB can be approximated as constant. However, due to their anisotropic structure, the flow behavior still cannot be characterized by a single viscosity, but rather the response to stress depends on the orientation of the stress field with respect to the director. In 1946, Marian Miesowicz investigated the viscous behavior of nematic liquid crystals, and he defined three different viscosities, now known as the Miesowicz viscosities, that characterize the nematic's resistance to flow when the stress field is commensurate with different high-symmetry directions within the nematic, as shown in Fig. 1.8 [25, 26]. η_a is identified as the viscosity when the flow velocity $\boldsymbol{v_0}$ and its gradient are both perpendicular to the director $\boldsymbol{n}$, η_b corresponds to when the flow $\boldsymbol{v_0}$ is parallel to the director while flow velocity gradient is perpendicular to $\boldsymbol{n}$, and η_c corresponds to when the flow $\boldsymbol{v_0}$ is perpendicular to $\boldsymbol{n}$ while flow velocity gradient is parallel to $\boldsymbol{n}$. For rod-like mesogens, $\eta_b < \eta_a < \eta_c$. Although the Miesowicz viscosities cannot be used directly when dealing with colloidal motion with nematics, since the flow field around a moving colloidal will not correspond exclusively to shear along a high symmetry direction, often they still provide a point of reference for interpreting with measured drag forces. For 5CB at room

temperature, the values of the Miesowicz viscosities are: $\eta_a = 37\ cP, \eta_b = 23\ cP$, and $\eta_c = 130\ cP$ [27].

1.1.8 Ericksen Number

Under low Reynolds number conditions, the hydrodynamic force acting on a moving particle in a Newtonian fluid simplifies to the viscous Stokes drag [28]. A simple case is that where a sphere translates with velocity $\vec{v}$ inside an isotropic fluid, in which case the drag force is:

$$\boldsymbol{F} = -D_s \eta \boldsymbol{v} \tag{1.14}$$

where $D_s = 6\pi R$ is the sphere's geometric coefficient, and η is the viscosity of the fluid. In the case of nematic liquid crystals, hydrodynamic forces couple to the nematic order and its corresponding anisotropic viscous behavior, which a makes complete description complicated, even in the low Reynolds number limit. The Erickson-Leslie equations, which are comprised of eight coupled differential equations [29-32], describe the hydrodynamic behavior or nematics, but their complicated form limits their utility. Generally speaking, to analyze most experimental situations, we do not need to solve the complete Ericksen-Leslie equations. Since the viscosity of the nematic is anisotropic, an important consideration in nematohydrodynamics is whether viscous forces of the flow are sufficiently strong to overwhelm the elastic forces and alter the director field away from its equilibrium (static) configuration, thus leading to non-linear effects. Analogous to the Reynolds number, the Ericksen number is a dimensionless parameter that provides a measure of the relative sizes of the viscous and elastic forces:

$$Er = \frac{\eta v a}{K} \tag{1.15}$$

where η is the average viscosity of the liquid crystal, v is the average speed of the flow, K is the average elastic constant, and a is the physical size of the flow. For example, in considering the flow field created by a colloidal particle moving in a nematic, a would be the particle size. Low Ericksen number means that the viscous forces are too weak to distort the director field. Therefore, the director field is assumed to be static. The assumption of $Er \ll 1$ puts a constraint on a colloidal particle's speed v. In the case of 5CB, η is about $0.06\ Pa \cdot s$, and K is about $10\ p$N. Therefore, for a colloidal particle 10 μm in size, low Er is achieved when

$$v \ll 10 \frac{\mu m}{s} \tag{1.16}$$

This constraint on the speed is easily to achieved in an experiment. For example, in the classic falling ball experiment, the stable speed when gravity of the particle is balanced by Stokes drag is determined by:

$$6\pi\eta a v = \frac{4\pi}{3} a^3 (\rho - \rho_{5CB}) g \tag{1.17}$$

Using the values above and the density of silica for the sphere, $v \sim 1\ \mu m/s$, which satisfies the constraint of Eq (1.16). Therefore, under such conditions, we can apply a linear Stokes drag to approximate the viscous force.

1.1.9 Stokes Drag in A Nematic Environment and Effective Viscosities

Although under many situations the viscous forces acting on moving particles through nematic liquid crystals can be expressed simply as Stokes drag, the anisotropic viscosity of the nematic leads to some interesting consequences [33]. For example, the drag force will be different if a particle moves perpendicular versus parallel to the

nematic director, and in general a tensorial form of the Stokes equation is required to describe the drag [34]. Also, as described above, different anchoring conditions at a particle's surface lead to different director field configuration and defect structures in the surrounding nematic, thus leading to drag forces that depend on the surface anchoring conditions and hence surface chemistry. In particular, a defect moving through a nematic induces dissipation [20], and therefore the presence of defects around colloids contributes to the drag they experience. In addition, as discussed by Stark, the streamlines bending around the particle also contributes to increasing the drag. Under these circumstances, the Stokes equation can still describe the viscous force, but the viscosity that enters the equation is an effective viscosity that includes the contributions from these effects. Stark summarized theoretical results for the effective viscosities of the Stokes drag in 5CB for three different director configurations, as seen in Table 1.1[20].

Table 1.1. The effective drag viscosities in 5CB for three different director configurations and for motion parallel and perpendicular to the director. As a reference, the three Mesowicz viscosities are included. Data is from Starks, 2001 [20].

	5CB: $\eta_a = 0.374\,\mathrm{P},\ \eta_b = 0.229\,\mathrm{P},\ \eta_c = 1.296\,\mathrm{P}$		
	Uniform $\boldsymbol{n}$	Dipole	Saturn ring
$\eta_{\mathrm{eff}}^{\parallel}$ (P)	0.381	0.532	0.501
$\eta_{\mathrm{eff}}^{\perp}$ (P)	0.754	0.869	0.848
$\eta_{\mathrm{eff}}^{\perp}/\eta_{\mathrm{eff}}^{\parallel}$	1.98	1.63	1.69

This anisotropic drag leads to an interesting phenomenon when the force driving the colloid through the nematic is applied at an oblique angle to the director. In this case, as predicted by Ruhwandl and Terentjev [35] and demonstrated experimentally by Rovner et al. [24], the colloid experiences a so-called nematic lift, such that the colloid's

velocity acquires a component normal to the force. Rovner et al. found that that a model based on a tensorial Stokes equation accounted quantitatively for magnitude of the lift and hence the direction of the velocity.

1.2 Soft Glassy Materials

Disordered complex fluids and soft solids, such as glassy colloidal suspensions, gels, and pastes, are ubiquitous in nature. These materials differ from simple liquids or solids due to hierarchical structure on the nanometer or micrometer scale. This structure instills these materials with elaborate mechanical properties, such as shear thinning, shear thickening, and thixotropy [36-38]. Underlying this nonlinear macroscopic deformation and flow behavior are shear-induced changes to the microstructure and microstructural dynamics. Identifying and understanding the connections between these microscopic structural dynamics and the macroscopic rheological properties remain a central goal for the fields of soft matter and colloidal science. This effort is made more challenging by the out-of-equilibrium nature of many disordered soft solids.

In recent years, x-ray photon correlation spectroscopy (XPCS) has emerged as a powerful probe for gaining insight into the microstructural dynamics that are relevant to the rheology of disordered complex fluids and soft solids. As part of my thesis research, I have participated in an effort to expand the potential of XPCS to probe microstructural dynamics associated with nonlinear rheology through the development of capabilities that combine coherent x-ray scattering with *in situ* shear. In the following chapters, I describe the basics of the technique and the results of my research employing it to study soft

glassy materials. Although the experiments I performed involved several soft glassy solids, including nanocolloidal gels, nanoemulsions, and clays gels, in this thesis, I focus on the results of the study of the nanocolloidal gels. In the sections below, I present a brief introduction to some of background concepts relevant to these studies.

1.2.1 The Fluid-Gel Transition

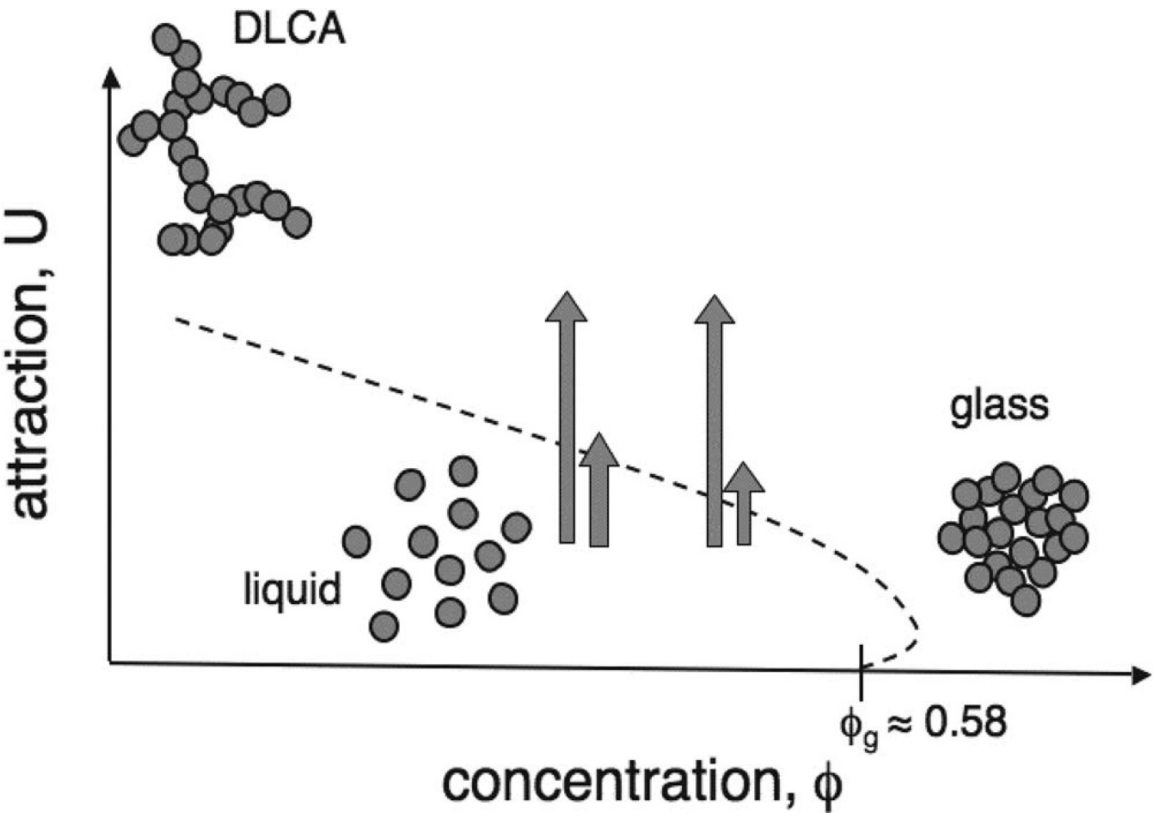

Figure 1.9: Schematic phase diagram depicting the boundary between the ergodic fluid state and nonergodic disordered solid states of colloidal suspensions with concentration φ and short-range attraction U. At high concentration, suspensions form a glass, while in the limit of dilute concentration and strong attraction, they form a gel through diffusion-limited cluster aggregation. The arrows refer to the experimental protocol of quenching moderately concentrated suspensions through the ergodic-nonergodic boundary by the sudden initiation of a short-range attraction of varying strength. Figure adapted from Reference [39].

Colloidal suspensions can transform between fluid and disordered solid states as a function of the colloidal volume fraction and the strength and nature of the colloidal interactions [39,40]. Control of this process is crucial to numerous technologies in a diverse range of areas including ceramics, food processing, and pharmaceuticals. As colloidal suspensions are among the simplest and most accessible materials for the study of ergodic to nonergodic transitions in soft condensed matter, they have also served as important models for addressing the fundamental physics of such transformations. For example, repulsive hard-sphere colloids undergo a glass transition at a colloid volume fraction ϕ near $\phi_g = 0.58$, and characterization of this process has led to insights relevant to the glass transition in molecular liquids and other materials. When a short-range, attractive interaction between the colloids is introduced, ergodicity breaking can occur at smaller volume fractions, as the colloids gel into long-lived network structures. In the limits of strong attraction and low concentration, the colloids create gels via the process of diffusion-limited cluster aggregation [41]. Such dilute gels have provided useful examples for understanding the formation and properties of materials with self-similar, fractal structures. Furthermore, at volume fractions slightly above ϕ_g, suspensions can display re-entrant glassy behavior with increasing attraction, providing evidence for an attractive glass transition [42-46]. A schematic phase diagram shown in Fig. 1.9, which depicts the fluid-to-solid boundary of suspensions of colloids with short-range attraction U, captures these different scenarios. As described below, the XPCS experiments on nanocolloidal gels under shear focused on gels with volume fractions around 0.3, which is intermediate between the dilute limit of fractal aggregates and the jammed limit of colloidal glasses.

1.2.2 Depletion Force

The interparticle attraction in the nanocolloidal gels that I studied was controlled by a depletion interaction. Here, I explain briefly the origin of this interaction. The depletion force arises when large colloidal particles are in a solution of smaller ones and are sterically constrained to avoid them [47]. The physical origin of the depletion force is that the overlap of the excluded volumes around the large particles increases the volume accessible to the small ones, thus raising the entropy by an amount ΔS and lowering the free energy F by $F = -T\Delta S$.

The depletion force is widely used in colloidal suspensions. In the samples I studied, the large particles were nano-sized silica spheres, and they were suspended in a solution of the non-absorbing polymer polystyrene, which acted as the depletant. To formulate the depletion interaction between the colloids, we can approximate the polymers as hard spheres of diameter σ, as shown in Fig. 1.10. When the depletion zones with thickness $\sigma/2$ around the colloidal particles with radius R overlap, a net force arises between the particles. This is because when the distance r between the centers of the colloidal particles is smaller than $2R_d = 2R + \sigma$, the small spheres cannot enter the gap between the colloids, leading to an osmotic pressure difference between the two sides of each sphere. Based on the symmetry, the depletion force points toward the centers of the spheres, and the only pressure on the surfaces that is not balanced is acting between $\theta = 0$ and $\theta_0 = arc\cos(\frac{r}{2R_d})$, as seen in Fig. 1.10. Therefore, the net force on each sphere is:

$$\mathrm{F(r)} = -2\pi\left(\mathrm{R} + \frac{\sigma}{2}\right)^2 \int_0^{\theta_0} P \sin\theta \cos\theta \, d\theta = \begin{cases} -\pi n_b kTR_d^2\left[1 - \left(\frac{r}{2R_d}\right)^2\right], & \boldsymbol{2R \le r < 2R_d} \\ 0, & \boldsymbol{r \ge 2R_d} \end{cases} \tag{1.18}$$

Here, the surface pressure is $P = n_b kT$, according to Van't Hooff law, where n_b is the polymer number density, and the negative sign indicates the force is attractive. This result is known as the Asakura-Oosawa model. Based on the form of the force, the depletion potential is written as:

$$\mathrm{V} = \frac{\pi}{6} n_b kT(\sigma - h)^2 \left(3R + \sigma + \frac{h}{2}\right) \tag{1.19}$$

where $h = r - 2R$ is the separation between two spheres, as seen in Fig. 1.9. In the limit of $\frac{\sigma}{2} \ll R$, the depletion force and potential simplify to:

$$F(h) = -\pi n_b kTR(\sigma - h) \tag{1.20}$$

$$\text{and } V(h) = -\frac{\pi}{2} n_b kTR(\sigma - h)^2 \tag{1.21}$$

.

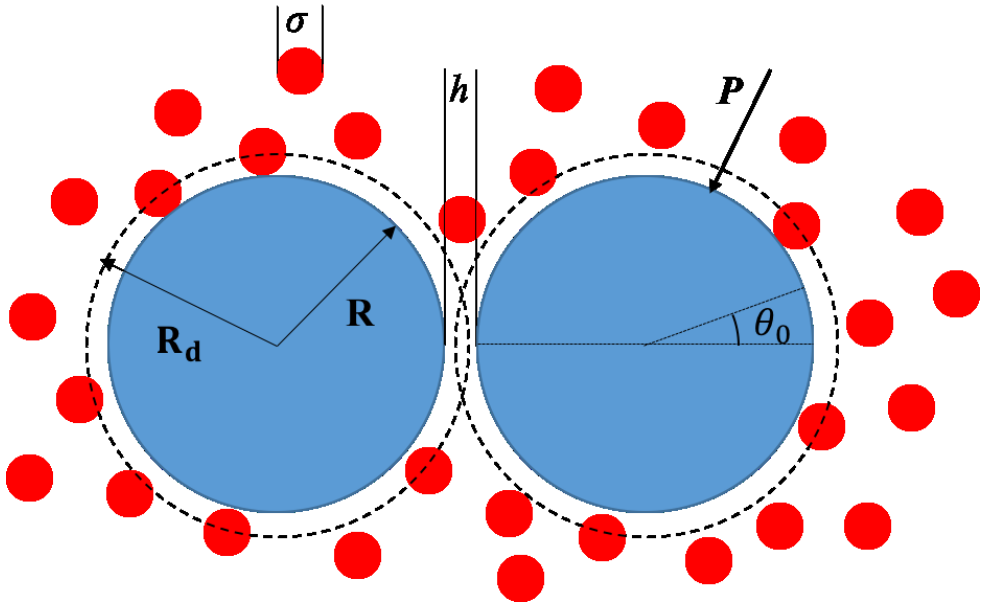

Figure 1.10: The schematic diagram of two colloids spheres (blue) immersed in small hard spheres (red) solution with separation h. The dashed circles represent the effective depletion radius. The unbalanced pressure (***P***) acting on each colloidal sphere leads to the attractive depletion force.

1.2.3 Rheology

1.2.3.1 Linear Rheology and Viscoelasticity

Rheology is the study of deformation and flow of materials. It deals with the relations between the microscopic structure and macroscopic mechanical response, and the relations between deformation and applied forces. Based on materials' strain response to stress, we can identify two limits, those of an ideal solid and Newtonian liquid. An ideal solid is fully elastic, and the deformation is reversible without dissipation. In a Newtonian liquid, the deformation is irreversible and all mechanical energy is lost through viscous dissipation. However, materials in the real world generally behave as partially elastic and partially viscous. In rheology, we are interested in these viscoelastic materials.

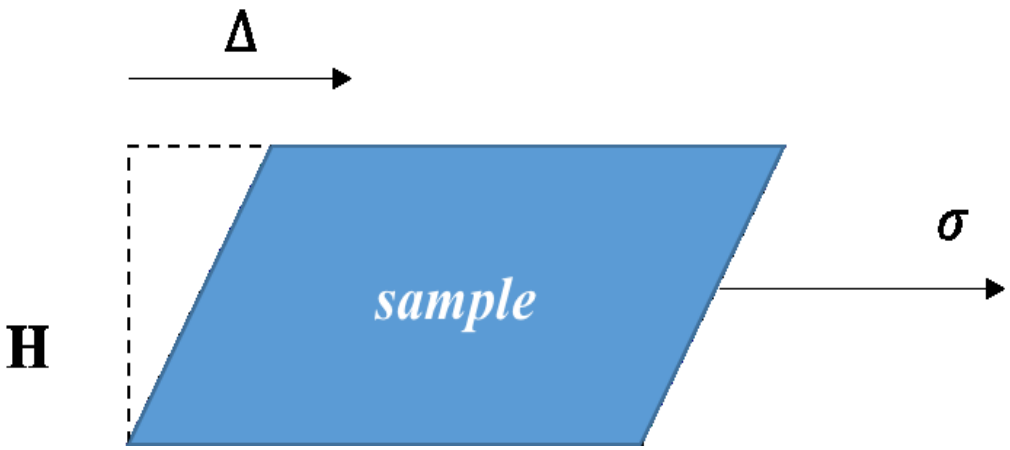

Figure 1.11: Material with thickness H deforms by an amount d under the stress σ. $\gamma = d/H$ is the strain.

Shear stress and strain are the central concepts in rheology. The shear stress σ is defined as the shear force F per unit area A: $\sigma = \frac{F}{A}$, while the strain $\gamma = \frac{\Delta}{H}$ is defined as the ratio of the displacement of the surface subjected to the shear force to the sample thickness, as seen in Fig. 1.11. For an ideal solid, γ and σ simply follow Hooke's law:

$\sigma = G\gamma$, where G is the shear modulus. For an ideal fluid, $\sigma = \eta\dot{\gamma}$, where η is the viscosity and $\dot{\gamma}$ is the shear rate. For a viscoelastic material, whose response has both viscous and elastic components, the stress response is more complicated, and the modulus G is a complex function of frequency (or time) consisting of two parts: the storage and loss moduli. Specifically for a applied small oscillatory shear stress $\sigma = \sigma_0 e^{i\omega t}$, the strain response in the linear regime is $\gamma = \gamma_0(\omega)e^{i(\omega t+\delta)}$, where δ is the phase shift. Therefore, the modulus G can be written as:

$$G(\omega) = \frac{\sigma}{\gamma} = G'(\omega) + iG"(\omega) \tag{1.22}$$

where $G'(\omega) = \frac{\sigma_0}{\gamma_0(\omega)}\cos\delta(\omega)$ is the storage modulus and $G"(\omega) = \frac{\sigma_0}{\gamma_0(\omega)}\sin\delta(\omega)$ is the loss modulus. Clearly, for an ideal solid $\delta = 0$, and for a Newtonian liquid $\delta = \frac{\pi}{2}$. The general case for viscoelastic materials, $0 < \delta < \frac{\pi}{2}$.

1.2.3.2 Non-linear Viscoelasticity

When the viscoelasticity is linear, the material satisfying two conditions: (i) the creep is a function of the entire loading history and (ii) each increment of load makes an independent and additive contribution to the total deformation [48]. A simple picture of linear viscoelasticity is to assume that the material response has two separable components: an elastic component and a viscous component. Based on this picture, several models including the Maxwell model, Kelvin-Voigt model and standard linear solid model have been developed to describe linear viscoelasticity.

As part of my thesis, I have been interested in materials that exhibit non-linear viscoelasticity, for example, the attractive colloidal gels in Chapter 5. For these gels, the

response to small shear stress is linear and primarily elastic, and their response to stress near or above a yield stress becomes nonlinear. Such nonlinear viscoelasticity will be discussed more in Chapter 5.

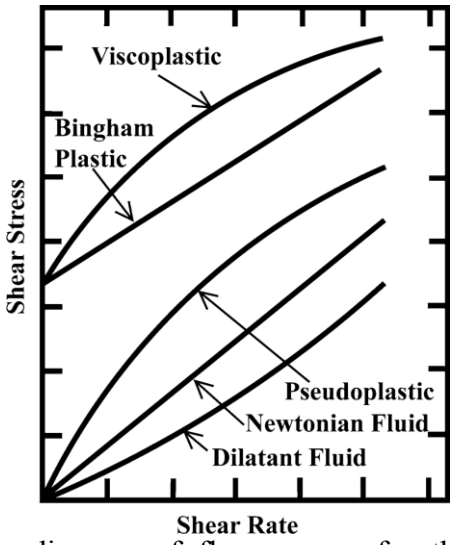

Figure 1.12: A qualitative diagram of flow curves for the different types of both Newtonian and non-Newtonian fluids. (from reference [48])

In general, fluids exhibiting non-linear or non-Newtonian behavior can be categorized according to the time dependence of the stress-shear-rate behavior as either time-independent fluids or time-dependent fluids. For the time-independent fluids, the stress σ at a given time can exclusively determine the value of $\dot{\gamma}$, regardless of history, and vice versa. Based on the form between σ and $\dot{\gamma}$, shear thinning, visco-plastic, and shear thickening materials can be identified. Shear thinning behavior means that the viscosity η decreases with increasing shear rate; while shear thickening is the opposite. A visco-plastic fluid behaves like an elastic solid when the external stress is below the yield stress σ_0 while it behave like a Newtonian fluid or shear thinning fluid when the external stress is above σ_0. Furthermore, when a visco-plastic fluid exhibits Newtonian behavior

above the yield stress, it is called a Bingham plastic fluid. According to this definition, the model of Bingham plastic behavior can be formulated as:

$$\sigma = \sigma_0 + \eta\dot{\gamma} \qquad \sigma > \sigma_0 \qquad (1.23(\boldsymbol{a}))$$

$$\dot{\gamma} = 0 \qquad \sigma < \sigma_0 \qquad (1.23(\boldsymbol{b}))$$

where σ is the external applied stress. On the other hand, if the behavior above yield stress is shear thinning, the visco-plastic fluid is called yield-pseudoplastic. Fig. 1.12 summarizes the flow curves of Newtonian and non-Newtonian fluids. The nanocolloidal gels that are the subject of the work discussed in Chapter 5 can be characterized as visco-plastic materials.

Chapter 2

Experimental Methods

As discussed in the Introduction, the research in this thesis deals with two major areas of soft matter physics: liquid crystals and soft glassy materials. In this chapter, I describe some of the experimental methods used in the research and provide some details regarding experimental procedures. The research into liquid crystals employed primarily polarization microscopy, and an essential component of the experiments involved creating sample cells that introduced the desired anchoring conditions (whether uniform or patterned) for the nematic director. Therefore, I describe the procedures for fabricating these cells in some detail. The research into soft glassy materials employed x-ray photon correlation spectroscopy (XPCS), a technique that utilizes coherent small-angle x-ray scattering to characterize the structural dynamics in disordered materials at nanometer length scales. In particular, a goal of the research was to integrate *in situ* shear deformation of materials into XPCS experiments; thereby gaining insight into the shear-induced microscopic dynamics that underlie the materials' rheological response. Hence, in this chapter, I briefly review both XPCS and rheology.

2.1 Liquid-Crystal Cell Fabrication

2.1.1 Making The Planar and Homeotropic Cell Device

Most sample cells employed in the liquid crystals experiments were comprised of two optical quality glass plates separated by small spacers, often called a sandwich structure, as depicted in Fig. 2.1. On the inner surfaces, we could dictate the desired anchoring conditions to control the alignment of the liquid crystals molecules near the surface, thereby controlling the alignment directions within the bulk, as described in Chapter 1. We created cells with surfaces treated to promote both planar anchoring and homeotropic anchoring.

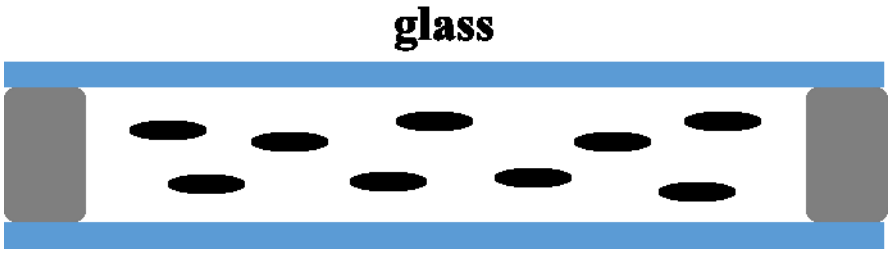

Figure 2.1: The "sandwich" structure of liquid crystal cells. Blue plates are glass slides; grey represents the spacers; and the black rods denote the liquid crystals molecules.

2.1.1.1 Planar Cell

Planar anchoring refers to alignment of liquid crystals molecules at a surface parallel to the surface. If the anchoring has no energetic preference for any direction within the plane parallel to the surface, it is called the degenerate planar anchoring; if the anchoring promotes alignment in a single direction, it is called the uniform planar anchoring. The widely used method to achieve uniform planar anchoring on glass slides is to employ a polymer coating. By rubbing certain polymer films with a cloth such as felt, an anisotropy in the film structure at the nanometer scale may be introduced that causes the liquid crystals molecules in contact with the film to align parallel to the

surface. In our experiment, we employed this method using films of polyimide 2555 (PI-2555, HD Microsystems) that we spin-coated onto the glass slides.

To create glass slides with polyimide films for planar anchoring, the glass was first cleaned thoroughly using the following procedure: (i) add concentrated Hellmanex solution into DI water at 1%−2% by volume; (ii) heat the diluted Hellmanex solution just below boiling; (iii) place the glass slides, which have been cut to the proper size, into the prepared solution, and sonicate for about 10 mins; (iv) rinse the glass slides with DI water several times; and (v) dry the glass slides with nitrogen gas.

The next step was to coat the cleaned glass slides with PI-2555. To improve the adhesion of the PI-2555 to the glass, the slides were pretreated by promoter VM651. VM651 was diluted with DI water at a volume ratio 1:999, and the glass slides were immersed into the diluted solution for about 1 minute. The slides were then dried with nitrogen air flow. For the spin coating the concentrated PI-2555 solution received from the manufacturer was diluted with the solvent 1-Methyl-2-pyttolidinone to achieve a desired viscosity. Specifically, the ratio of PI-2555 and 1-Methyl-2-pyttolidinone should be adjusted until the mixture displays a light yellow coloration. The mixture was then spread on the pretreated glass slide surface and subjected to spinning. The typical spinning rate was about 2000−3000 rpm, leading to films with thicknesses around 2.5 − 3.5 μm. Following spin coating, the slides were hard baked to stabilize the polyimide film by leaving the coated slides on a 200 °C hot plate for at least 2 hours.

After coating was finished, we needed to introduce the uniform planar anchoring by rubbing the polymer film. We did so by placing the coated glass side facing down to a flat board covered with fine-pile velvet, and sliding the glass in one direction about 5 or 6

times. The preferred anchoring orientation for the nematic is then induced parallel to the sliding direction. As a matter of fact, the induced orientation is not exactly parallel to rubbing direction. Instead, it has a small tilt angle to the plane, as depicted in Fig 2. Therefore, when assembling two slides to construct a cell with uniform planar anchoring, we have two different ways to arrange the slides: "parallel" (Fig. 2.2(a)) and "anti-parallel" (Fig. 2.2(b)). I typically applied the "parallel" method to build planar cells.

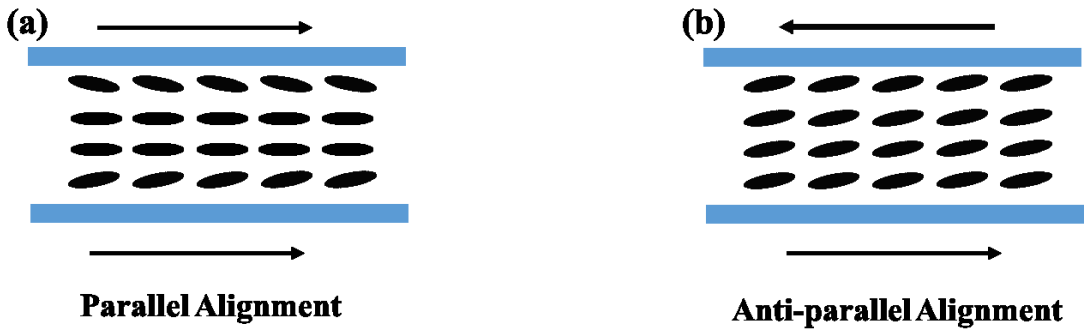

Figure 2.2: Two arrangements for the planar anchored slides. The arrow represents the rubbing direction on this surface. (a) Parallel alignment. (b) Anti-parallel alignment.

The final step in creating a planar cell involved securing two treated slides parallel with the desired separation. To set the separation, I glued small pieces of plastic film with the correct thickness to the slides. To fill the cells, I placed them on a hot plate at 40 ℃ (above isotropic-nematic transition of 5CB) and introduced the 5CB into cell through a pipet from one side. Capillary action caused the liquid crystal to fill the cell spontaneously. The typical volume of 5CB to fill a cell was about 30~50 μl. Once a cell was filled, I turned off the hot plate and allowed the cell to cool slowly through the nematic phase to room temperature so that a defect-free uniform nematic texture was achieved.

2.1.1.2 Homeotropic Cell

The fabrication of a cell with surfaces promoting homeotropic anchoring is relatively simple. The common method is to introduce self-assembled monolayers onto the glass slides using silane coupling agents as depicted in Fig. 2.3. The agents have a hydrolyzable group, which reacts with the substrate to form a chemically stable bond, and a long linker (or organic functional group), which promotes perpendicular orientation of the liquid crystal molecules at the surface. In my experiments, I employed the silane coupling agent N,N-Dimethyl-N-octadecyl-3-aminopropyltrimethoxysilyl chloride (DMOAP), which is a quaternary amine functional silane, as illustrated in Fig. 2.4(a). The silane sites of DMOAP can bond to glass (silica) surfaces, while the long $(CH_3)_n$ linkers interact with liquid crystals molecules to orient them parallel to the chains and hence perpendicular to the substrate.

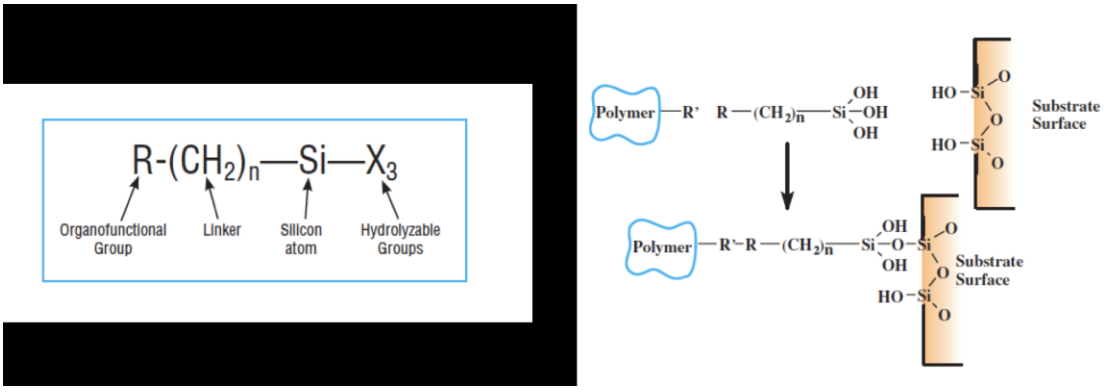

Figure 2.3: Structure of silane coupling agents. (a) four groups commonly exist inside a silane coupling agent. (b) silane coupling agent functionalization between substrate surface and in-solution polymer. (pictures from website: www.gelest.com)

The formation of homeotropic anchoring with DMOAP is illustrated in Figs. 2.4(b) to (d). DMOAP adheres to the glass when the slides are immersed in an aqueous

solution of the coupling agent. When the slides are immersed in water, the –OH groups on the glass surface are ionized with negative charge. Therefore, not only do the silane groups bind to the surface, but also positively charged N-sites are attracted to the –OH group, leaving the linker $(CH_3)_n$ perpendicular to surface. If the density of linkers is appropriate, liquid crystal molecules will inter-digitate and adopt the perpendicular orientation, leading to, homeotropic anchoring. The spacing of the linkers can be controlled by the concentration of DMOAP in the aqueous solution.

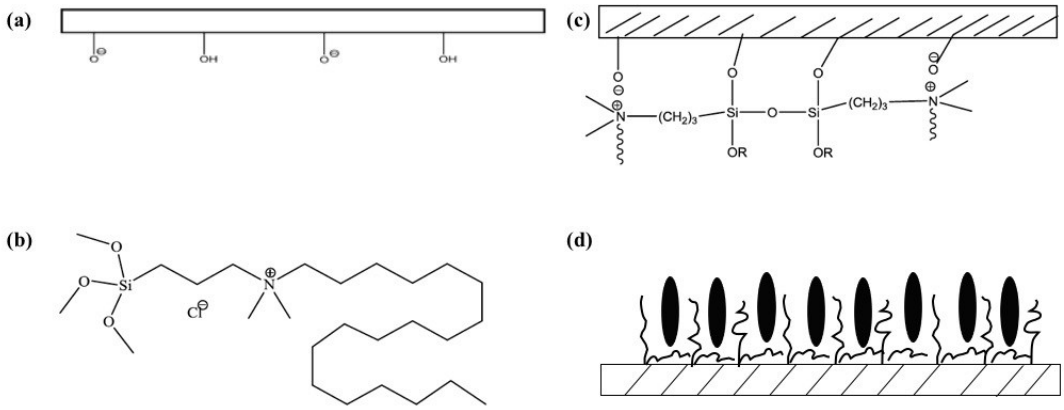

Figure 2.4: Structure of DMOAP and schematic of formation of homeotropic anchoring condition. (a) The surface group at wet glass surfaces. (b) Structure of DMOAP (c) DMOAP reacting with substrate surface. (d) Liquid crystals mesogens (black rods) inserting into spaced formed by DMOAP to achieve homeotropic anchoring. (from reference [49])

To create homeotropic cells, the first step is to clean the glass slides following the same procedure as in making planar cells. Second, one dilutes the DMOAP by mixing it into DI water at a mass ratio of 2:98. Then, the slides are immersed in the DMOAP solution for about 5 minutes so that the DMOAP molecules can bond to the slide surface. Finally, the glass slides are dried with nitrogen gas flow. To fabricate a homeotropic cell

from such treated slides, one can follow the same procedure as in fabricating a planar cell.

2.1.2 Making PDMS Microfluidic Devices

In my thesis, I studied the behavior of colloids within nematic liquid crystals confined to the interstitial spacing in an array of microfluidic posts. The process of making these devices involves photolithography, PDMS molding, PDMS bonding, and surface treatments, as shown in Fig. 2.5. In this section, I describe each of these procedures in turn.

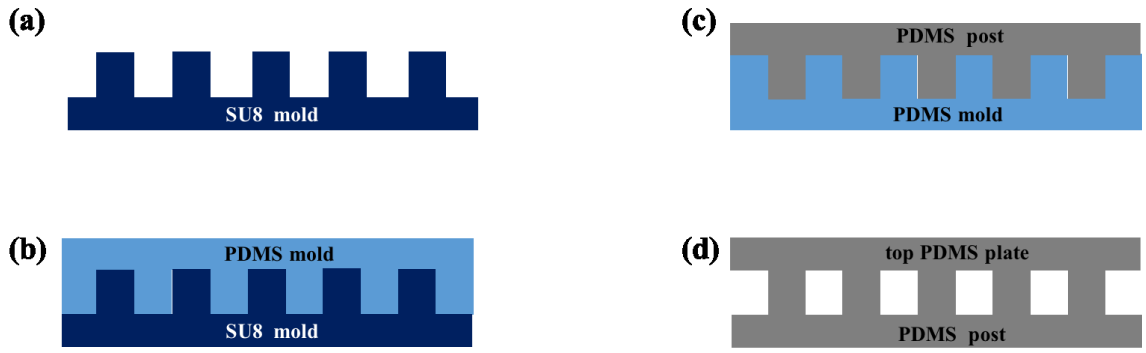

Figure 2.5: A schematic diagram of PDMS microfluidic device fabrication. (a) SU8 mold created via photolithography. (b) PDMS mold created from the SU8 template mold. (c) PDMS post array formed from the PDMS mold. (d) Post array bonded with a PDMS plate to form enclosed microfluidic device.

2.1.2.1 Photolithography

Photolithography is a process of microfabrication that uses UV light to transfer a geometric pattern from a photomask to a light-sensitive chemical called photoresist on a substrate. Photoresist consists of two types: positive resists and negative resists. A positive resist is a type of photoresist in which the portion of the photoresist that is

exposed to light becomes soluble in the photoresist developer, and the portion of the photoresist that is unexposed remains insoluble, as depicted in Fig. 2.6(a). Alternatively, with a negative resist, the areas that are exposed to light become insoluble to the developer, and the unexposed regions are dissolved by the developer, as in Fig. 2.6(b). Commonly used positive resists are the S1800 series (Shipley) and AZ series (MicroChemicals), while a commonly used negative resist is the SU-8 series (MicroChemicals). Generally speaking, positive resists can have a feature resolution as small as 1 μm, but require small film thickness less than 10 μm; negative resists have lower resolution, but allow larger film thickness between 10 μm to several mm. In my thesis, I used SU8-2050 negative photoresists. In addition, Fig. 2.7 displays the photomask (Mylar, Fineline Image) used in the experiment.

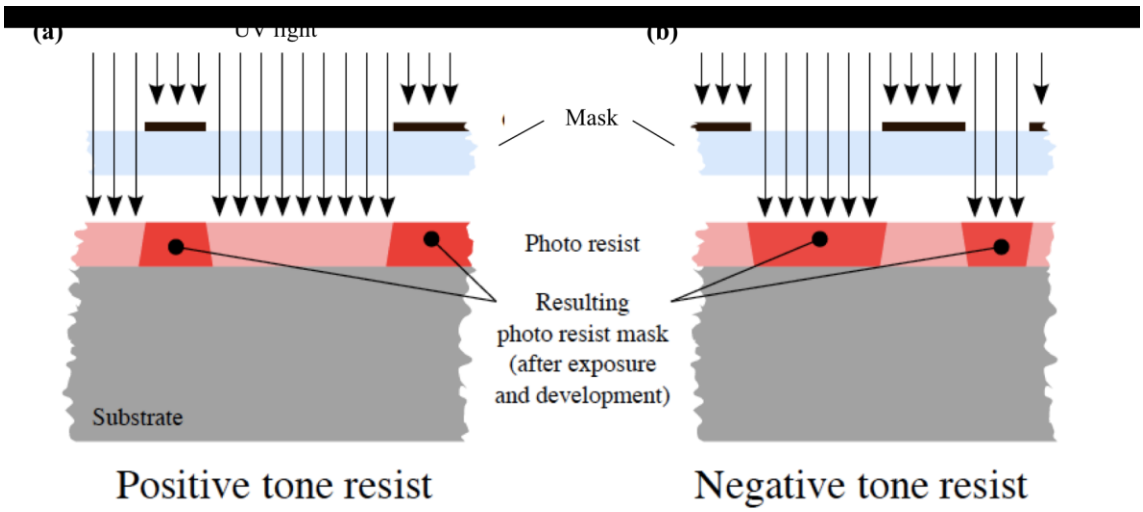

Figure 2.6: The comparison between types of photoresist. (a) Positive resist. The exposed resist becomes dissolvable by developer. (b) Negative resists. The unexposed resist becomes dissolvable by developer. (pictures by Cepheiden, 2010)

For the photolithography process, I employed a silicon wafer as the substrate. The procedure I followed was: (i) I cut the wafer to the desired shape and cleaned it with Hellmanex solvent; (ii) I rinsed the wafer with DI water for 30 seconds, air dried it, and left it on a hot plate at 115 °C to evaporate remaining water molecules; (iii) I allowed the wafer to cool to room temperature and placed it on the spinner; (iv) I spread SU8 2050 to cover the whole surface. (Because the temperature may affect the spreading behavior of SU8 2050 resist, maintaining both the wafer and SU8 at room temperature is necessary.) (v) Following the published SU8 2050 spinning curve, I used 2000 rpm for about 1min to obtain a 60 μm thick film. (vi) I soft baked the film for 3 minutes at 65 °C and 9 minutes at 95 °C and then allowed the wafer to cool to room temperature prior to UV exposure. (vii) To apply a typical exposure for a 60 μm thick SU8 2050 film of about 100 mJ/cm^2 using the aligner in the P&A clean room, I exposed for 4.5s. (vii) I applied a two-step

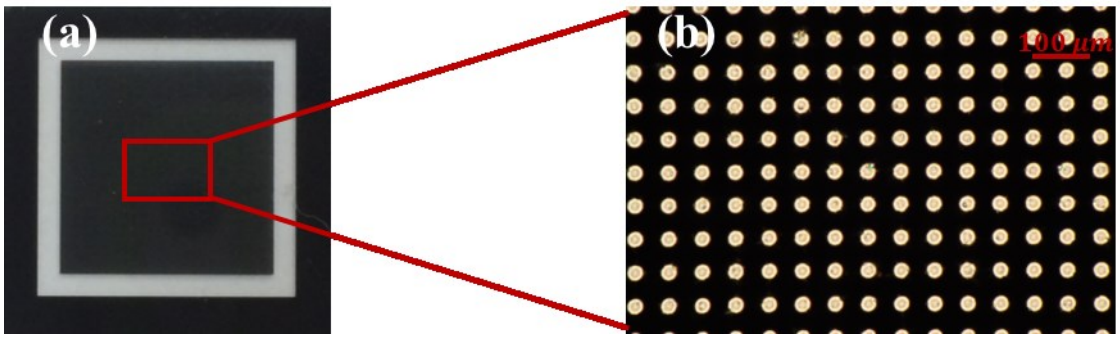

Figure 2.7: (a) Photomask (b) Photomask under microscope.

post-baking of 60 °C for 1 minute and 95 °C for 7 minutes and then let the wafer cool to room temperature. (viii) To develop the exposed SU8, I placed the wafer in developer solution and stirred using a magnetic stir bar at a moderate rate (a setting of 3.5-4.5 on

the magnetic stirrer in the clean room) for about 20 minutes. (ix) I then removed the wafer from the developer and rinsed with isopropyl alcohol. (x) If a white film appeared on the waver, I concluded the SU8 was under developed, and developed for additional time. (xi) Once developing was complete, I dried the wafer with nitrogen gas flow, and checked the structure under a microscope. (xii) I applied hard baking at 180 °C for 10 minutes to enhance the adhesion between the wafer and SU8 film, heal any cracks on the surface, and make the film more uniform. A typical resulting film structure obtained by confocal microscopy is shown in Fig. 2.8.

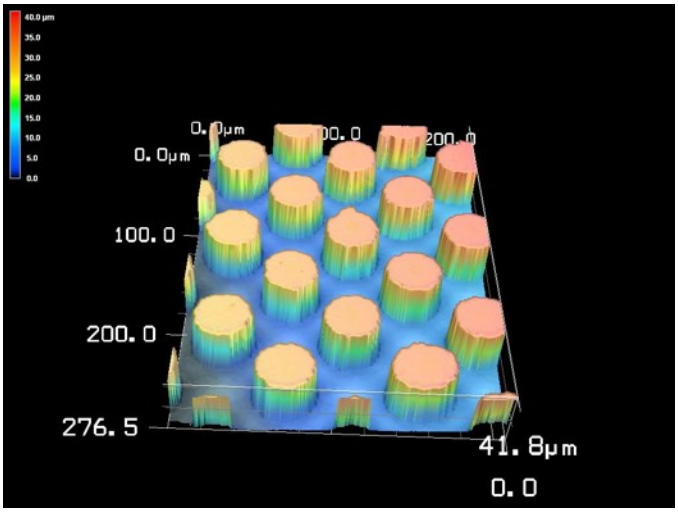

Figure 2.8: Confocal image of SU8 mold used to make post arrays. The height of the posts is about 40 μm, the diameter is about 35 μm and the distance between two nearest post centers is about 60 μm.

2.1.2.2 PDMS Molding

Due to degradation by thermal stress during the curing process and by de-molding forces, repeated use of an SU8 mold is limited. Therefore, I created PDMS molds from the SU8 molds to increase the lifetime of the molds. PDMS consists of two components:

the agent and the kit. To create a PDMS mold, I followed these procedures: (i) Mix the agent and kit at a mass ratio of 10:1. (For PDMS with a larger elastic modulus, the ratio should be lowered and vice versa.) (ii) Stir the mixture for at least 10 minutes. (iii) Pour the mixture onto the wafer with the SU8 pattern, (iv) Place in a vacuum oven and degas for about 30 minutes until all bubbles disappear. (v) Break vacuum in the oven and cure the PDMS at 80 ℃ for about 2 hours. (A higher curing temperature will decrease the time; however, the resulting structures will be more prone to defects.) (vi) Peal the PDMS from the patterned SU8 wafer. (vii) Perform plasma-based surface modification of the PDMS to achieve anti-sticking behavior needed for PDMS-PDMS molding. To do so, apply oxygen plasma (available in the Microfabrication Lab) to the PDMS surface at 0.4 Torr, and 25W for 45 seconds. (viii) Place the PDMS in the vacuum oven along with several drops of Trichloro (1H,1H,2H,2H-perfluoro-octyl) silane solution. Pumping a vacuum in the oven accelerates the evaporation of the silane, which forms a thin layer on the PDMS surface that acts as an anti-stick film during subsequent PDMS-PDMS molding.

2.1.2.3 PDMS Bonding

After the PDMS mold is ready, it may be employed to create PDMS-based microfluidic devices using the following procedures: (i) mix the PDMS agent and kit again and pour the mixture onto the PDMS mold. (ii) Cure at 80 ℃ for another 2 hours. (iii) Peal the PDMS device from the PDMS mold. (iv) Bond another, flat PDMS sheet to the PDMS patterned sheet to form an enclosed microfluidic device. (v) Bond the two PDMS pieces using oxygen plasma. With the oxygen plasma, the Si-O bonds at the

PDMS surfaces will be opened and will transform to O-Si-O bonds between the surfaces, leading to a permanent bonding. Note this same method can be used to bond other surfaces with Si-O bonds, such as PDMS and glass. In addition, oxygen plasma is also widely applied for dry etching. For example, realizing photolithography of SU8 on glass is often difficult because of the weak adhesion of SU8 to glass. To improve the adhesion, the glass can be pre-treated by strong oxygen plasma. The typical treatment condition is 100 W and 0.5 Torr for 10 minutes.

If the PDMS device is to be used in liquid-crystal studies like those described in this thesis, two additional steps before the plasma process are needed. First, holes must be punched through the top PDMS sheet to form channels for injecting the liquid crystal. Second, to achieve the desired anchoring conditions at the PDMS surfaces, the surfaces must be functionalized. Untreated PDMS promotes degenerate planar anchoring. For homeotropic anchoring, the surfaces can be coated with DMOAP by following the same procedure as coating glass slides before the plasma bonding. Since the DMOAP functionalization will be destroyed by the plasma process used to bond the PDMS, only areas of the PDMS where the bonding is to occur should be exposed to the UV during the plasma treatment. Therefore, I covered the area of the device containing the posts with a black paper, thus preserving the homeotropic coating on the PDMS surface, and left uncovered the area around the edges to bond to the top PDMS sheet. The final steps to complete the bonding and the device fabrication were (i) Place the top PDMS sheet with punched holes and the treated PDMS posts with center covered into oxygen plasma chamber at 30 W and 0.3 Torr for 30 s, and (ii), Soft bake the device at 80 ℃ for 5 minutes in order to enhance the bonding.

2.1.3 Growth of Cholesteric Figure Textures in a Homeotropic Cell

As a part in my thesis, I investigated colloidal transport within cholesteric figure textures. The cholesteric finger textures were created in homeotropic cells by mixing nematic 5CB with the chiral dopant CB15. In the dilute limit, the cholesteric pitch p was adjusted by varying the weight concentration c of CB15 following the formula $p = \frac{1}{f \cdot c}$, where $f = 7.3\ \mu m^{-1}$ is the macroscopic helical twisting power. In my experiment, I controlled the concentration of CB15 to adjust the pitch and applied external electric and magnetic fields to control the growth rate and direction of the cholesteric finger texture, using methods first employed by Ishikawa et al [9]. The procedure was as follows:

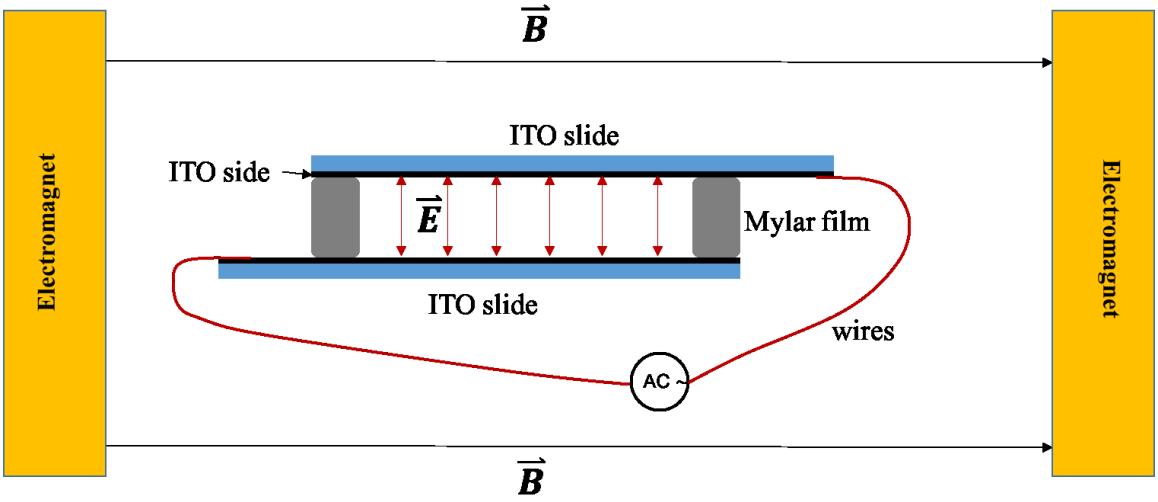

Figure 2.9: Schematic of approach for growing cholesteric finger textures. The dark line represents the conductive side of ITO glass slide.

First, I built a homeotropic cell with two flat ITO covered glass slides. ITO-glass slides were used because the ITO coating is conductive but transparent. Homeotropic anchoring was achieved following the same process described above. I then placed the

conductive sides of the ITO-glass slides face to face and separated them by Mylar film to form a sandwich structure. In order to obtain a uniform finger texture, the cell thickness d, which is set by Mylar film thickness, should be approximately equal to the pitch, $d/p \sim 1$. The glass slides also need to be staggered about $5\,mm$ to each other, so that electric cables have enough space to connect to the ITO surface, as depicted in Fig. 2.9. UV-cured glue was used to stabilize the connection between the Mylar film and ITO glass slides.

Then the cholesteric mixture of CB15 and 5CB with appropriate molecular ratio was injected into the cell. I then placed the cell at the center of an electromagnet, which applied about 1T field. In the presence of the in-plane magnetic field, I quickly applied an electric field across the cell in order to null the initial random fingerprint texture by reorienting 5CB molecules along the field normal to the plates. An AC power supply with frequency of 1Hz and magnitude of 10V was used. After 10 minutes, I slowly turned off the electric field and left the sample in the magnetic field for another 1 hour. The result was macroscopically aligned finger textures.

2.1.4 Preparation of Colloid-Dispersed Liquid Crystals

As discussed in Chapter 1, the behavior of micrometer-sized colloids suspended in liquid crystals depends highly on the anchoring condition at the colloid surface. The research described in this thesis involves colloids composed of two materials, silica and nickel. (As fabricated, nickel colloids possess a thin surface layer of nickel oxide.) In both cases, untreated colloids in 5CB impose planar anchoring. Homeotropic anchoring requires chemical modification of the surfaces, which can be achieved with DMOAP

functionalization. The procedure is quite similar to the treatment of glass. In summary, I first prepared a DMOAP solution in DI water in 2:98 mass ratio. I then added the colloids into the DMOAP solution and sonicated for several minutes. After sonication, I added more DI water to dilute the unreacted DMOAP. I then usually let the colloids sediment to the bottom of the container, extracted the supernatant with a pipet, and repeated 3 to 4 times. To accelerate this step, centrifugation can be applied, or for the nickel particles, a magnet can be placed underneath the vial. Following the last step of removing the supernatant, I dried the colloids on a hot plate at 80 °C. It is important to leave the colloids on the hot plate for enough time to ensure that most water molecules are evaporated. I then added 5CB to the dried colloids and sonicated for 10 minutes to disperse the colloids.

2.1.5 Image Analysis: Particle Tracking and Line Tracking

Video microscopy is widely used in the experiments in this thesis. Therefore, I developed several image analysis techniques to track the position of colloidal particles and other objects, such as disclination lines, from sequences of video images.

The core algorithms for particle tracking are based on the work from previous graduate student Daniel Allan, who wrote the Python code "trackpy", which focuses on identifying circular objects in video images and connecting their positions frame-to-frame. Details about the software can be found in Dr. Allan's Github webpage[1]. This tracking method is quite efficient and accurate and can be applied in various environments. For example, in the research described in Chapter 3 and Chapter 4, I applied it to track the

[1] *https://github.com/soft-matter*

motion of disks in cholesteric finger textures and the motion of spheres in nematics within obstacles arrays. Example tracking results are displayed in Fig. 2.10(a)-(b). Another feature I tracked through image analysis was the shape and position of line defects over the time, as be described in Chapter 3. Defect lines usually have a stronger brightness compared with the background. Based on this color feature, we could locate the defect lines through code written in Mathematica. Example results are displayed in Fig. 2.10(c).

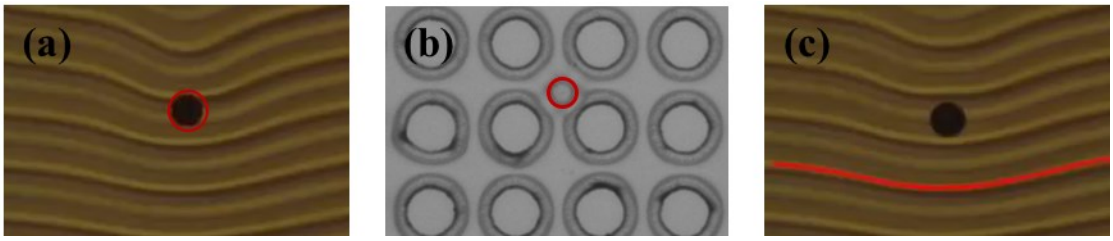

Figure 2.10: Examples of particle tracking and defect tracking. Red lines represent the results. (a) and (c) Nickel disks in cholesteric finger texture. (b) Silica spheres in a nematic within an obstacle array.

2.2. X-ray Scattering

2.2.1 Static X-ray Scattering

Following their discovery by Wilhelm Rontgen in 1895, x-rays quickly developed into a means to characterize the microscopic structure of materials. X-rays are broadly defined to have a wavelength ranging from 0.01 to 10 nanometers, corresponding to a frequency between 3×10^{16}Hz and 2×10^{19}Hz. In an x-ray scattering experiment, the incident beam interacts with the electrons of the atoms in a material, causing the electrons to resonate and emit photons that form the scattered light. By measuring the intensity patterns of the scattered light, we may infer structural information about the materials.

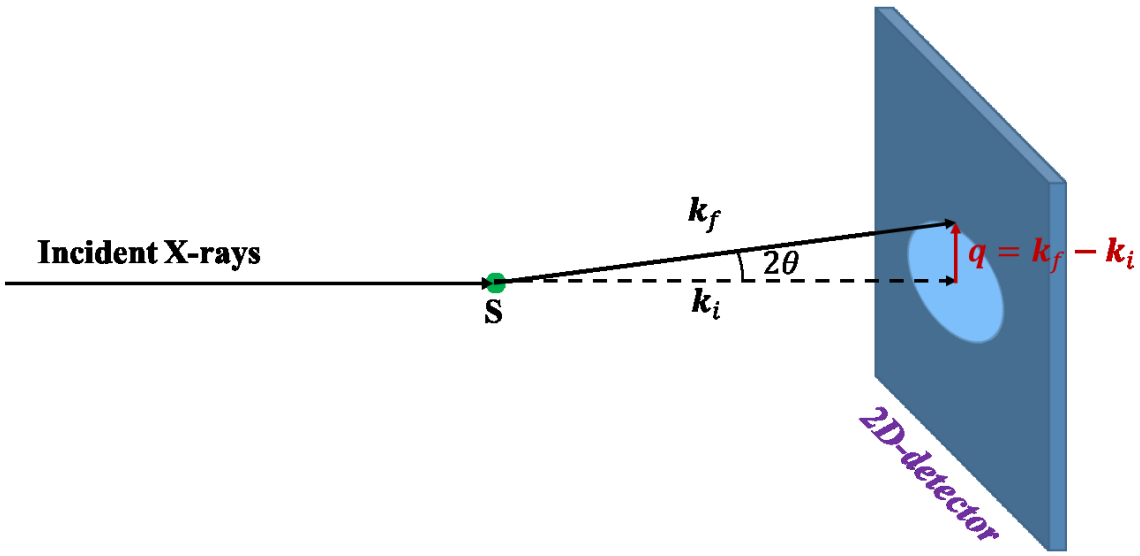

Figure 2.11: A schematic diagram of X-ray scattering. An incident X-ray is scattered by a scatterer S (green sphere). 2D detector collects the intensity patterns over $\boldsymbol{q}$.

Assume the incident beam has a wave vector $\boldsymbol{k}_i$, and the scattered light has a wave vector $\boldsymbol{k}_f$. Under a quasi-elastic approximation where the energy change is small, we can take $|\boldsymbol{k_i}| = |\boldsymbol{k_f}|$. To build the general theory of x-ray scattering, let's consider the case as shown in Fig 2.11. The scattering amplitude is:

$$A(\boldsymbol{q}) = \sum f_n e^{-i\boldsymbol{q}\cdot\boldsymbol{r}_n} \tag{2.1}$$

where $\boldsymbol{q} = \boldsymbol{k}_f - \boldsymbol{k}_i$, f_n is the atomic scattering factor of the n^{th} atom at position $\boldsymbol{r_n}$ and the summation is over all the scatterers. Therefore, the intensity $I(\boldsymbol{q})$ can be written as:

$$I(\boldsymbol{q}) = |A(\boldsymbol{q})|^2 = \left(\sum f_n e^{-i\boldsymbol{q}\cdot\boldsymbol{r}_n}\right)\left(\sum f_m^* e^{i\boldsymbol{q}\cdot\boldsymbol{r}_m}\right) \tag{2.2}$$

If the material consists of many identical scattering units, then

$$I(\boldsymbol{q}) = |F(\boldsymbol{q})|^2 \cdot \sum_{m,n} e^{-i\boldsymbol{q}\cdot(\boldsymbol{r}_n - \boldsymbol{r}_m)} \tag{2.3}$$

where $F(\boldsymbol{q})$ is called the form factor, which represents the scattering from a single unit, in this case the atom. Furthermore, the second term can be written as:

$$S(\boldsymbol{q}) = \sum_{m,n} e^{-i\boldsymbol{q}\cdot(\boldsymbol{r}_n - \boldsymbol{r}_m)} = \int < \rho(\boldsymbol{r}_1)\rho(\boldsymbol{r}_2) > e^{-i\boldsymbol{q}\cdot(\boldsymbol{r}_1 - \boldsymbol{r}_2)} d\boldsymbol{r}_1 d\boldsymbol{r}_2 \qquad (2.4)$$

where $S(\boldsymbol{q})$ is called the static structure factor, and $< \rho(r_1)\rho(r_2) >$ is the density-density correlation function, which is the conditional probability of finding a scatterer at position $\boldsymbol{r}_2$ when there is a scatterer at position $\boldsymbol{r}_1$. If the material is homogenous, $\langle \rho(\boldsymbol{r}_1)\rho(\boldsymbol{r}_2) \rangle = \langle \rho(|\boldsymbol{r}_1 - \boldsymbol{r}_2|)\rho(0) \rangle$; therefore,

$$S(\boldsymbol{q}) = V \int < \rho(r)\rho(0) > e^{-i\boldsymbol{q}\cdot\boldsymbol{r}} d\boldsymbol{r} \qquad (2.5)$$

From Eq (2.5), we see that the structure factor is the direct Fourier transformation of density-density correlation function. More details can be found in Warren's book [49].

2.2.2 Coherent and Incoherent Scattering

In the above discussion on x-ray scattering theory, which closely follows the standard description provided in textbooks, an important assumption is made about the coherence properties of the incident x-ray beam. Specifically, the beam must be coherent over length scales in which the density-density correlation function displays features, so that scattered waves over this length scale interfere. However, since the correlation function is a thermodynamic quantity, the measurement must average over numerous correlation regions to sample an ensemble. These features are achieved by the x-ray beams created at a typical synchrotron, where at the sample position the transverse coherence lengths are usually of order ten micrometers while the beam is of order a millimeter across. Hence, the scattering volume contains many thousands of coherence volumes that produce coherent scattering patterns that add incoherently at the detector to provide the ensemble average.

2.2.3 X-ray Photon Correlation Spectroscopy

However, if the incident beam is restricted in size to only a few coherence volumes, then the scattering intensity will be proportional to the amplitude squared of the fourier transform of instantaneous electron density distribution inside the material (and not an ensemble average). Taking advantage of the high brightness of third-generation synchrotron radiation sources, measurements can indeed restrict incident beams to this size. For a disordered material, the resulting scattering is a highly mottled interference pattern of bright and dark spots known as speckles. One example of speckle is displayed in Fig 5.2, Chapter 5. Under some circumstances one can invert such a speckle pattern to recover information about the atomic positions in a material (and not simply their statistical average). This is the principle of the technique of coherent diffraction imaging. Furthermore, however, if the scatterers in the material are moving, the intensity fluctuations of speckle patterns will vary over time, providing information about the microscopic structural dynamics within the material. Analyzing such time dependence to infer dynamics is the principle of x-ray photon correlation spectroscopy (XPCS) [50,51], which is the technique I employed in the research described in Chapter 5. XPCS is a powerful probe to gain direct insight into the microstructural dynamics that are relevant to soft materials' rheology. Specifically, when applied in a small angle x-ray scattering (SAXS) geometry, XPCS usually measures the low frequency dynamics ($10^3 - 10^{-3}$ Hz) in a q range corresponding to length scales of nanometers to tens of nanometers. This combination of length and time scales is well matched to those of the structural dynamics that figure prominently in the rheological behavior of many soft materials. This capability has led to efforts to connect the microscopic information about structural

dynamics obtained from XPCS to the macroscopic mechanical response in a host of materials with interesting and complicated rheology [52]. The research I describe in Chapter 5 is an effort to build on this idea by using XPCS to investigate the structural dynamics of soft disordered materials undergoing *in situ* shear. In the following sections, I briefly review previous work in this area.

2.2.3.1 XPCS under Flow

In XPCS experiments the normalized intensity autocorrelation function plays a central role:

$$g_2(\boldsymbol{q},t) = \frac{<I_{ij}(\boldsymbol{q},t_w)I_{ij}(\boldsymbol{q},t_w+t)>}{<I_{ij}(\boldsymbol{q},t_w)><I_{ij}(\boldsymbol{q},t_w+t)>} \tag{2.6}$$

Here $I_{ij}(\boldsymbol{q},t_w)$ is the scattering intensity measured at the (i,j) pixel on the CCD detector at scattering vector $\boldsymbol{q}$ and at waiting time t_w. t is the delay time and $<\cdots>$ means averaging over all pixels with nearly the same $\boldsymbol{q}$ value and all waiting time t_w. $g_2(\boldsymbol{q},t)$ is a quantity we can determine directly from the measurement. In the case of homodyne scattering, $g_2(\boldsymbol{q},t)$ is related to the dynamic structure factor $g_1(\boldsymbol{q},t)$ through the Siegert relations:

$$g_2(\boldsymbol{q},t) = 1 + \beta|g_1(\boldsymbol{q},t)|^2 \tag{2.7}$$

where $g_1(\boldsymbol{q},t)$ is the dynamic structure factor, which is another principal quantity that describes the structural dynamics in materials. For a system containing N scatterers,

$$g_1(\boldsymbol{q},t) \propto \sum_{n=1}^{N}\sum_{m=1}^{N} < \boldsymbol{b}_n^*(\boldsymbol{q},0)\boldsymbol{b}_m(\boldsymbol{q},t)\exp\left[-i\boldsymbol{q}\cdot\left(\boldsymbol{r}'_n(0)-\boldsymbol{r}'_m(t)\right)\right] > \tag{2.8}$$

where is the, $\boldsymbol{b}_n(t)$ is the scattering length of particle n in the material at time t and $\boldsymbol{r}'_n(t)$ is this particle position in the presence of flow at time t. When we focus on

homodyne SAXS measurements on dilute colloidal suspensions where the particles can be assumed to be non-interacting and uncorrelated, $g_1(\boldsymbol{q}, t)$ is simplified as:

$$g_1(\boldsymbol{q}, t) \propto \sum_{k=1}^{N} < \boldsymbol{b}_k^*(0)\boldsymbol{b}_k(t) \exp\left[-i\boldsymbol{q} \cdot \left(\boldsymbol{r}'_k(0) - \boldsymbol{r}'_k(t)\right)\right] > \tag{2.9}$$

In considering the motion of particles under flow, the difference of particle position at different time can be expressed by:

$$\boldsymbol{r}'_k(0) - \boldsymbol{r}'_k(t) = \underbrace{\boldsymbol{r}_k(0) - \boldsymbol{r}_k(t)}_{term\ 1} + \underbrace{\boldsymbol{v}_0 t}_{term\ 2} + \underbrace{\delta\boldsymbol{v}t}_{term\ 3} \tag{2.10}$$

Here $\boldsymbol{r}_k(t) - \boldsymbol{r}_k(0)$ is the change in the kth particle position caused by diffusive motion over the time interval t, $\boldsymbol{v}_0$ is the average particle flow velocity over the incident beam area, and $\delta\boldsymbol{v}$ is the flow velocity difference between positions $\boldsymbol{r}_k(t)$ and $\boldsymbol{r}_k(0)$. These three terms in Eq (2.10) contribute to the decay of the intensity autocorrelation function $g_2(\boldsymbol{q}, t)$ with different mechanics [53, 54]:

(i) Particle Diffusion: the characteristic decay time scale is $\tau_D = (Dq^2)^{-1}$, where D is the diffusion coefficient.

(ii) Transit effect: the decay of intensity autocorrelation function can also be caused by the nonzero net flow where particles exit and new particles enter the illuminated volume. In this case, the characteristic time is $\tau_T = L/v_0$, where L is the transverse beam size and v_0 is the average flow speed.

(iii) Shear effect: a shear gradient can introduce the velocity gradient between two different positions that causes a decay in the correlation function. . The physics behind this shear-induced effect is that the frequencies of the x-rays scattered by particles which are moving with different velocities are Doppler-shifted, therefore the scattering from pairs of such particles are phased shifted. The characteristic

time is $\tau_S = (q\dot{\gamma}Hcos\theta)^{-1}$, where $\dot{\gamma}$ is the magnitude of local velocity gradient, H is the sample thickness and θ is the angle between local velocity and the scattering wave vector. .

Provided that the characteristic times of these three processes are well separated, the intensity autocorrelation function can be factorized into three terms based on the above three contributions:

$$|g_1(\boldsymbol{q},t)|^2 = \left|g_{1,D}(\boldsymbol{q},t)\right|^2 \cdot \left|g_{1,T}(\boldsymbol{q},t)\right|^2 \cdot \left|g_{1,S}(\boldsymbol{q},t)\right|^2 \tag{2.11}$$

For a non-flowing isotropic sample, particle diffusion follows the standard form, leading to:

$$\left|g_{1,D}(\boldsymbol{q},t)\right|^2 = \exp(-2Dq^2t) \tag{2.12}$$

However, when a shear is applied, the diffusion can become anisotropic and dependent on the shear rate $\dot{\gamma}$:

$$\left|g_{1,D}(\boldsymbol{q},t)\right|^2 = \exp\left[-2Dq^2t\left(1 - \frac{q_\parallel q_\perp}{q^2}\dot{\gamma}t + \frac{1}{3}\frac{q_\parallel^2}{q^2}(\dot{\gamma}t)^2\right)\right] \tag{2.13}$$

here $q_\parallel$ and $q_\perp$ are the components of wave vector parallel to the flow and perpendicular to the flow [55].

As mentioned above, the transit term, given by the term $\left|g_{1,T}(\boldsymbol{q},t)\right|^2$, decays on a time scale set by its characteristic time $\tau_T = L/v_0$. Under most situations, τ_T is much larger than characteristic times of the other terms, and $\left|g_{1,T}(\boldsymbol{q},t)\right|^2$can be approximated as a constant.

The shear-induced term $\left|g_{1,S}(\boldsymbol{q},t)\right|^2$ can be obtained by sum over all pairs of particles within the scattering volume:

$$\left|g_{1,S}(\boldsymbol{q},t)\right|^2 = \frac{1}{V^2}\iint_V \cos(\boldsymbol{q}\cdot\delta\boldsymbol{v}(\boldsymbol{r}_1,\boldsymbol{r}_2)\,t)\mathrm{d}r_1{}^3\mathrm{d}r_2{}^3 \qquad (2.14)$$

where $\delta\boldsymbol{v}(\boldsymbol{r}_1,\boldsymbol{r}_2)$ is the velocity difference between position $\boldsymbol{r}_1$ and $\boldsymbol{r}_2$.

2.2.3.2 XPCS under Steady Shear

Recently, Burghardt *et al.* reported XPCS experiments on colloidal suspensions under homogeneous steady shear flow (i.e. flow with a time-independent and spatially uniform velocity gradient) [56]. In these experiments, the incident beam was parallel to the shear gradient direction, so that in the small-angle-scattering limit of the measurements the scattering wave vectors lay in the flow-vorticity plane. In this case, Eq (2.14) can be rewritten as:

$$\left|g_{1,S}(\boldsymbol{q},t)\right|^2 = \frac{1}{H^2}\int_0^H\int_0^H \cos[q_\parallel\dot{\gamma}(y_2-y_1)t]dy_1dy_2 = \frac{\sin^2\left(\frac{q_\parallel\dot{\gamma}Ht}{2}\right)}{\left(\frac{q_\parallel\dot{\gamma}Ht}{2}\right)^2} \qquad (2.15)$$

where the incident beam direction is taken to be the y-direction. Again, since $\left|g_{1,S}(\boldsymbol{q},t)\right|^2$ depends only on the component of the wave vector parallel to the flow, by analyzing $g_2(\boldsymbol{q},t)$ along different wave-vector directions, Burghardt *et al.* were similarly able to characterize independently the velocity gradients of the shear flow and colloidal diffusion along the vorticity direction. However, a key observation that they made was that the ability to resolve the colloidal diffusion was restricted to measurements at relatively low shear rates. At higher rates, the decay in the transit term $\left|g_{1,T}(\boldsymbol{q},t)\right|^2$ becomes a dominant effect along $q_\perp$. Also, due to the need to average over pixels that subtend a finite range of scattering angles to obtain $g_2(\boldsymbol{q},t)$, measurements nominally along $q_\perp$ must also include contributions with a small component along $q_\parallel$, and hence the shear term becomes also

appreciable at high rates. In particular, Burghardt *et al.* concluded that measurements at sufficiently high Peclet number ($Pe = \dot{\gamma}R^2/D$, where R is the particle radius) to observe shear-induced perturbations to the intrinsic dynamics would be unfeasible in the scattering geometry they employed, although other geometries might offer improvements [56]. In Chapter 5, I describe experiments in which XPCS in combined with large-amplitude oscillatory shear (LAOS). One motivation for this work was to investigate whether such measurements could overcome some of the limitations that steady shear has in accessing shear-induced structural dynamics. Also, as I describe in Chapter 5, coherent scattering in conjunction with LAOS can uncover unique information about the particle rearrangements and other microscopic processes that underlie yielding and plastic flow in soft disordered materials.

Chapter 3

Colloidal Transport in Cholesteric Liquid Crystals

3.1 Introduction

An important area of soft matter concerns the mobility of colloidal particles within structured fluids. Typically, the drag forces and other interactions that a particle experiences in a structured fluid are significantly subtler and more complicated than the Stokes drag from a simple Newtonian fluid [57-59]. The resulting dynamics can provide insightful, microscopic perspectives into the properties of the fluid. They can also form the foundation for new technologies in areas such as self-assembly, separations, and sensing. Although much research has concerned colloids within nematic liquid crystals, distortions to cholesteric order imposed by a suspended particle may lead to interparticle interactions and colloidal assemblies not seen in nematics, in part because the distortion to the order depends not only on the anchoring conditions at the particle surface but also on the size of the particle relative to the pitch [60,61]. Further, recent studies have shown how the size dependence affects dynamics, specifically by making the drag force on a sphere moving through a cholesteric a nonlinear function of the sphere radius in contrast with Stokes law [60, 62]. In this chapter, I report an experimental investigation of the mobility of discoidal colloidal particles in frustrated cholesterics known as finger textures that are characterized by a periodic array of disclinations in the order.

As introduced in Chapter 1, as a special type of liquid crystal with helical structure, cholesteric liquid crystals (CLCs) can form finger textures when sandwiched between two glass slides. As described below, finger textures are actually the result of distorting the cholesteric structure by confining it between plates with homeotropic anchoring, which creates a boundary condition incompatible with the cholesteric director field given by Eq. (1.3). Previous research indicated an elaborate phase diagram of CLCs finger textures controlled by the relative size of the cell gap thickness d and pitch p, the applied voltage U, and the dielectric and elastic properties of the CLC [63,64]. What's more, the geometrical frustration that leads to the distorted director structure also imposes the formation of topological defects, and one difference among the finger texture phases that can form is the various configurations of defects that each possesses. Exploring motion in these frustrated cholesteric enables me to investigate both colloidal mobility in a fluid with broken translational symmetry and the effect of interactions between defects in the order and the colloids on the colloid dynamics.

3.2 Experimental Methods

Figure 3.1 displays a schematic of the experimental arrangement. We followed the procedures described in Chapter 2 to create homeotropic ITO glass cells containing mixtures of 5CB and CB15 to form the finger textures. Fig. 3.2 displays one sample with $d = 24\ \mu m$ and $p = 24\ \mu m$. Silica spheres and nickel disks were premixed into the 5CB in order to introduce them into the system. The mobility of the colloidal particles in the finger textures was characterized by classic ‘‘falling ball’’ experiments in which the drag

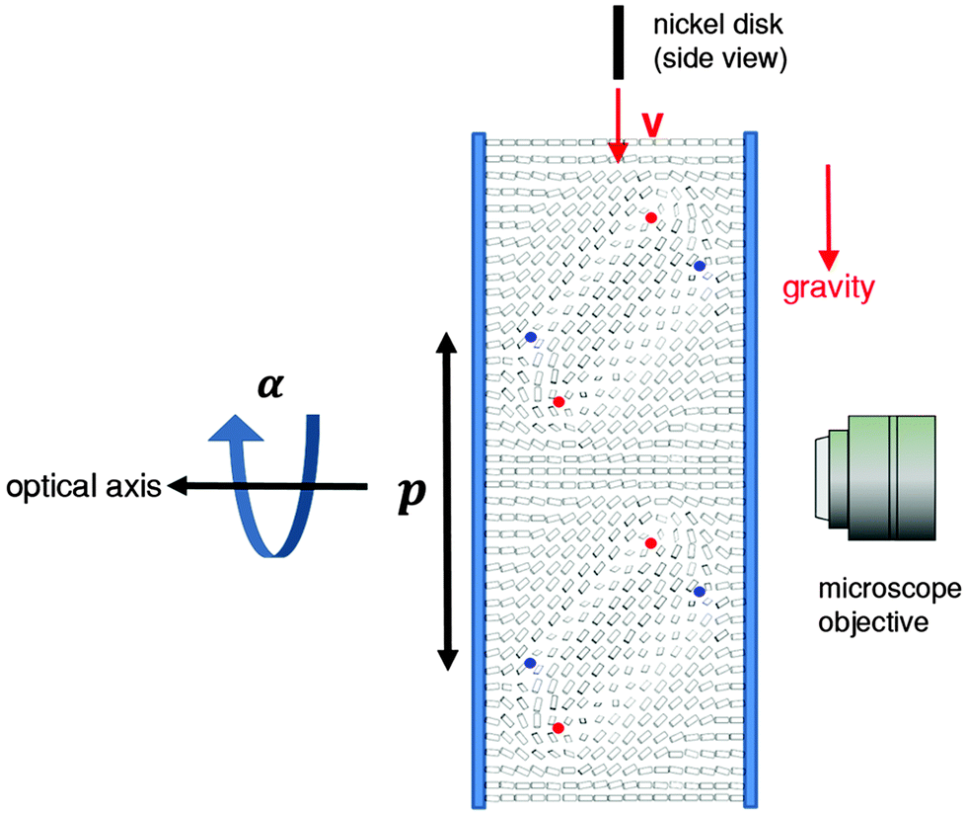

Figure 3.1: Schematic of the sedimentation experiments. The microscope was tilted 90° to make the driving force (gravity) parallel to the focal plane. Strong homeotropic anchoring at the surfaces of the glass slides (blue) caused the cholesteric liquid crystal with pitch p to assume a distorted CF-1 finger texture. The local director orientation within the texture, which is depicted by the cylinders, includes nonsingular +1/2 (red dots) and -1/2 (blue dots) disclinations (schematic of finger texture adapted from reference [10]).

on a particle with a density larger than that of the surrounding fluid is measured by balancing it with gravity, as illustrated in Fig. 3.1. Two types of micro-size particles are studied: untreated silica spheres with $10\,\mu m$ diameter, and planar nickel disks with $40\,\mu m$ diameter and $300\,nm$ thickness. In order to decrease the interaction between the particles and substrate, the optical microscope was tilted by 90° to make gravity parallel to the focal plane (also the sample plane), as depicted in Fig. 3.1. The in-plane angle α was adjusted by rotation of the sample stage; I define $\alpha = 0$ to be parallel to the cholesteric pitch.

The chiral structure of the cholesteric is frustrated by the homeotropic anchoring condition at the substrates. As a result, the director field assumes a distorted configuration that nevertheless preserves the periodicity of the cholesteric. Four different metastable textures, or finger textures, have been identified for cholesterics in homeotropic cells. As mentioned above, the prevalence of each depends on parameters such as the strength of the anchoring, the elastic constants of the liquid crystal, and the strength of any external electric field. The texture that has the lowest energy under most conditions and hence is the most commonly observed is known as CF-1 [63], and the conditions in our experiment led to the formation of this texture. In the CF-1 texture, the cholesteric axis orients parallel to the substrates, and each period contains two pairs of closely positioned non-singular $\lambda^{+1/2}$ and $\lambda^{-1/2}$ disclinations that run perpendicular to the cholesteric axis, as depicted schematically in Fig. 3.1.

3.3 Experimental Results

3.3.1 Silica Spheres within Cholesteric Finger Texture

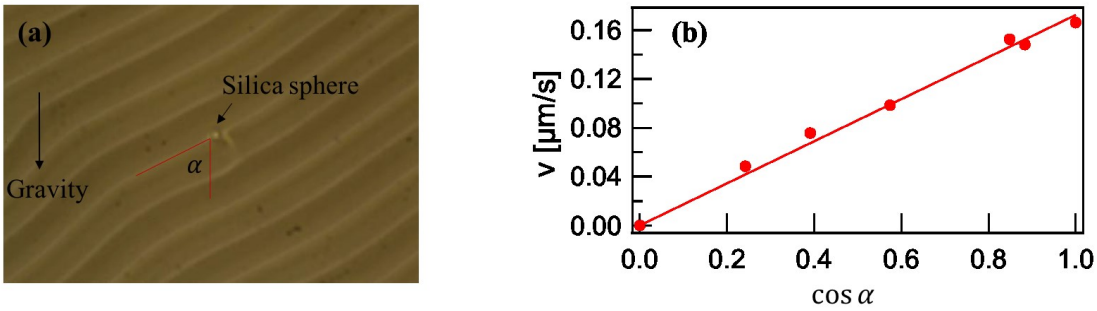

Figure 3.2: Silica sphere translated through cholesteric liquid crystals responding to gravity. (a) Sphere moves exclusively parallel to disclination direction under different rotational angle α. (b) Plotting of sphere speed with different α. $\cos\alpha$ is proportional to driving force along disclination direction. Perfect linearity between v and $\cos\alpha$ indicates a constant effective drag viscosity.

I observed that silica spheres moving under the force of gravity through the finger textures were unable to cross the disclination lines. As a result, the spheres remained trapped within one period of the texture and translated exclusively parallel to the lines, as depicted in Fig. 3.2(a). The velocity $\boldsymbol{v}$ of a sphere as a function of the in-plane angle α is shown in Fig. 3.2(b). The velocity varies linearly with the $\cos\alpha$, which is proportional to the component of gravity perpendicular to the pitch (parallel to the disclination lines) and hence parallel to the velocity. This linear relationship indicates that the spheres experience a simple viscous Stokes drag in this direction:

$$\boldsymbol{F}_{Drag} = 6\pi R\eta\boldsymbol{v} \tag{3.1}$$

where R is the radius of the silica spheres, and η is the effective drag viscosity. Meanwhile, the component of the gravitational force parallel to the pitch (perpendicular to the disclination lines) is balanced by an elastic force associated with deformation of the lines that impedes any motion in this direction. To obtain a value for the effective drag viscosity, we can equate the drag with the gravitational force:

$$6\pi R\eta v = G\cos\alpha \tag{3.2}$$

where $G = \frac{4}{3}\pi R^3(\rho_{silica} - \rho_{5CB})g$, and ρ_{silica} and ρ_{5CB} are densities of silica and 5CB respectively. Interestingly, we find that the effective viscosity is anomalously large, around $720\ mPa\cdot s$, which is several times larger than the largest Miesowicz viscosity of nematic 5CB. As described below, we observed similarly large drag viscosities on the nickel disks translating through the finger textures. A discussion of this effect is given below.

3.3.2 Nickel Disks within the Cholesteric Finger Texture

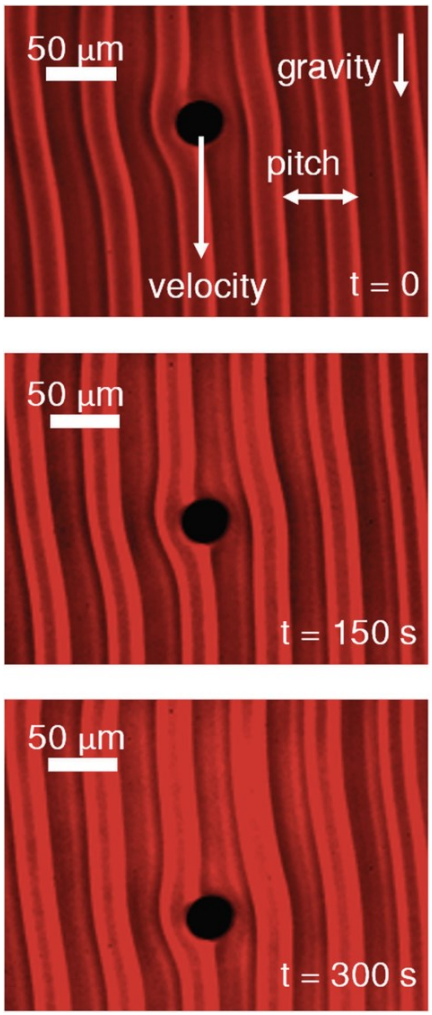

Figure 3.3: Images of a Ni disk sedimenting through a cholesteric finger texture with a 62 mm pitch. The disk velocity is parallel to gravity, which is perpendicular to the cholesteric axis. The texture distorts in the vicinity of the moving disk, increasing the drag. The time interval between successive images is 150 s.

The mobility of the disks in the cholesteric finger textures showed a strong dependence on the size of the pitch. At small pitch ($p < 40\,\mu m$), the disk motion was exclusively perpendicular to the cholesteric axis regardless of the orientation of the applied force, and a force parallel to the axis resulted in no motion. Thus, the elastic forces associated with distortions of the texture balanced the component of gravity along the cholesteric axis. However, in textures with larger pitch, the dynamics were complex as the gravitational force was sufficient to overcome the elastic retardation along the axis, leading in some cases to stick-slip motion. In the sections below, we describe the nature of the motion for various conditions of pitch size and direction of applied force that illustrate this highly anisotropic and pitch-dependent mobility, and we present a model that describes the stick-slip dynamics.

A. Sedimentation force perpendicular to cholesteric axis

The simplest behavior was observed when the gravitational force was oriented perpendicular to the cholesteric axis and hence parallel to the disclinations ($\alpha = \pi/2$). In this case, the disks moved at a constant velocity *v* parallel to the force. Fig. 3.3 displays a series of bright-field micrographs showing a disk moving in this direction in a texture with $p = 62\,\mu m$. Since the motion was at low Reynolds number ($R_e \sim 10^{-6}$), this constant velocity implied that drag forces from viscous dissipation $\boldsymbol{F_d}$ balanced gravity, $\boldsymbol{F_d} = -\boldsymbol{F_g}$. For a disk translating in a simple isotropic liquid, the drag force would be given by Stokes law,

$$\boldsymbol{F_d} = -\zeta \boldsymbol{v} = -\frac{32}{3} R\eta \boldsymbol{v} \tag{3.3}$$

where $\zeta = \frac{32}{3} R\eta$ is the drag coefficient for a disk, and η is the liquid's shear viscosity.

From the velocity of the sedimenting disk in the cholesteric, one can employ Eq (3.3) to obtain an effective drag viscosity η_{eff} that characterizes the dissipation. We stress that the application of Eq (3.3), with $\zeta = \frac{32}{3} R\eta_{eff}$ to describe the drag on the disk in the cholesteric, is not strictly valid. Due to the broken orientational and translational symmetry of the cholesteric, the flow field around the disk and hence the nature of the drag are more complicated than those of an isotropic liquid for which Stokes law is derived. In particular, as discussed further below, the disk mobility depends strongly on the relative size of R and p, indicating a distinctly non-Stokesian character to the motion. Nevertheless, we employ the Stokes form to describe the drag since it provides a measure of the drag in a familiar form that allows easy comparisons of the dissipation experienced under different circumstances. For example, for the motion depicted in Fig. 3.3, we obtain $\eta_{eff} = 420\, mPa \cdot s$. Similar values were found for disks moving perpendicular to the cholesteric axis in textures with different p. As with the motion of the spheres described above, this effective drag viscosity is strikingly large compared with that describing colloidal motion in nematic 5CB where, depending on the direction of motion with respect to the nematic director and the anchoring conditions at the particle surface, drag viscosities vary between $25\, mPa \cdot s$ and $110\, mPa \cdot s$, which fall in the range of the Miesowicz coefficients of 5CB. We attribute the anomalously large drag in the finger textures to dissipation associated with motion of the disclination lines, which must deform in the vicinity of the disk as it falls, as illustrated in Fig. 3.3. As mentioned above, this result is similar to the experiment on silica spheres translating through the finger textures. In contrast, in an experiment of on nickel, wires with longitudinal surface anchoring [65], which oriented with their axis perpendicular to the cholesteric axis and

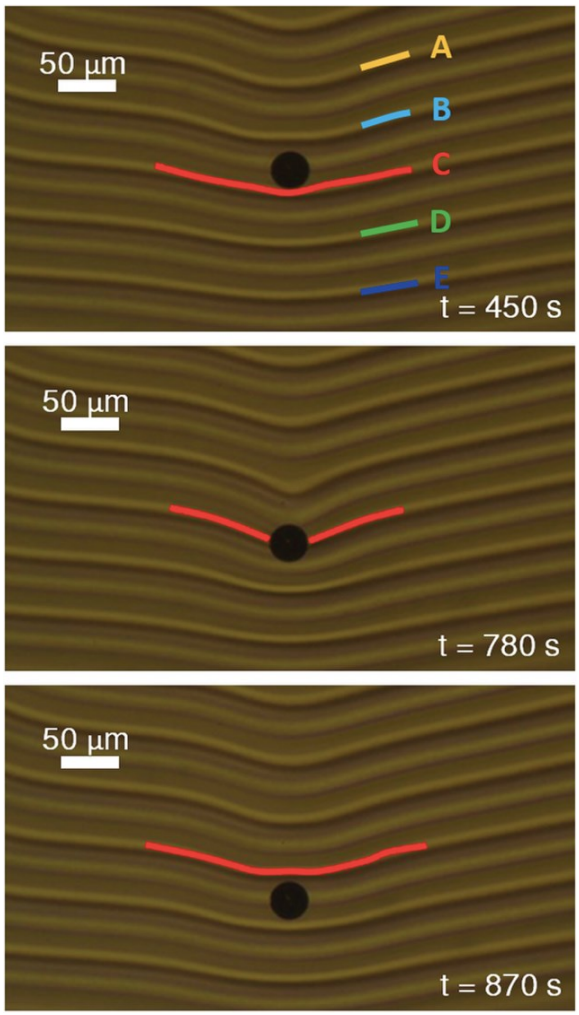

Figure 3.4: Images of a Ni disk sedimenting through a cholesteric finger texture with 60 μm pitch in response to gravity parallel to the cholesteric axis. Five sets of disclination lines are labeled A through E in the top image. The contour of one set, labeled C, is depicted in red in all three images to illustrate the time-dependent distortion of the texture as the disk undergoes stick-slip motion. The time of each image matches the time axis of Fig. 3.5.

created no observable distortion of the texture, the wires sedimented with an effective drag viscosity that was similar to the values in pure 5CB. Specifically, the effective drag viscosity experienced by a $10\,\mu m$ long Ni wire with diameter $350\,nm$ translating in $70\,\mu m$ pitch texture was approximately $150\,mPa \cdot s$.

B. Sedimentation force parallel to cholesteric axis

When the force of gravity was oriented parallel to the cholesteric axis ($\alpha = 0$), the viscous response of the texture was accompanied by spatially varying elastic contributions whose strength depended on the cholesteric pitch. In textures with small pitch ($p < 40\,\mu m$), the disks remained stationary ($v = 0$). We interpret this lack of motion as due to a balance between the elastic forces associated with distortion of the texture and gravity. In textures with larger pitch, the elastic forces, while still present, were insufficient to balance gravity and instead the disks underwent periodic stick-slip motion. Fig. 3.4, which displays a series of bright-field micrographs of a disk in a texture with $60\,\mu m$ pitch, illustrates this motion. A set of disclination lines in each micrograph is highlighted in red. As the disk passed through the disclinations they temporarily attached to the disk. As a result, the disk distorted the texture, stretching the disclinations as it fell. Eventually, the disk detached from the disclinations, allowing the texture to recover from the distortion. As the disk stretched the disclinations, its motion was increasingly retarded. Then, when it detached, it briefly moved relatively unencumbered until it encountered the next set of disclinations, and the process repeated. Fig. 3.5(a) displays the height and velocity as a function of time of a disk undergoing this motion as it traversed three periods of the texture with $p = 60\,\mu m$. During each period, the velocity

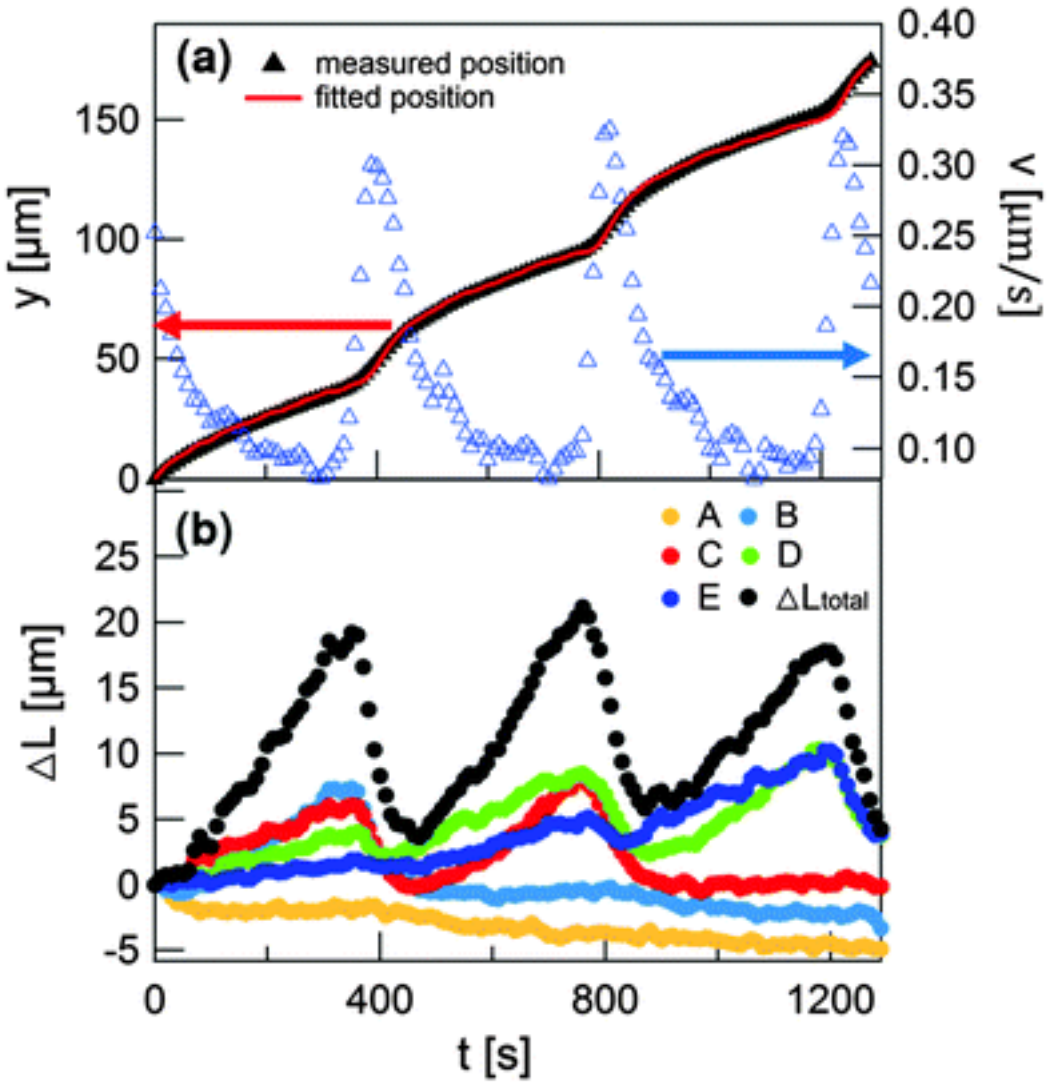

Figure 3.5: (a) Position (solid triangles) and velocity (open triangles) of the disk shown in Fig. 3.4 sedimenting through a 60 μm pitch figure texture in response to gravity parallel to the cholesteric axis. Downward in the images in Fig. 3.4 is taken as the positive *y* direction. The solid red line is the result of a fit to the position using the model described in Section **3.3.3**. (b) The lengths of the disclination lines labeled in the top image in Fig. 3.4 in excess of their undistorted lengths along with the sum of the excess lengths.

steadily decreased, corresponding to when the disk stretched the disclinations, and then suddenly jumped to a larger value, signaling detachment. In the following section, we present a model that describes this periodic stick-slip motion.

C. Sedimentation force at oblique angle to cholesteric axis

When the gravitational force was oriented at an oblique angle to the cholesteric axis, the resulting disk motion contained elements of the behavior seen in both the perpendicular and parallel configurations, and the nature of the motion depended both on the pitch size and on the angle α between the force and the axis. In textures with large p at small,α the motion was similar to that when the force was parallel to the axis: the disks translated parallel to the driving force with periodic stick-slip motion. However, at large α the component of gravity parallel to the cholesteric axis was sufficiently small that the elastic forces associated with distorting the texture could balance it. The resulting motion in this case is illustrated in Fig. 3.6, which displays a series of micrographs of a disk in a texture with $p = 60\ \mu m$ and $\alpha = 70^{\circ}$. Instead of undergoing stick-slip motion, the disk remained near one set of disclinations and moved parallel to the disclinations (and hence at an angle $\pi - \alpha$ to the applied force) at constant velocity. Assuming that the force causing this motion was the component of gravity perpendicular to the cholesteric axis (parallel to the disclinations), we can again interpret the constant velocity as the result of a balance between the driving force and drag forces from viscous dissipation, $\boldsymbol{F_d} = -\boldsymbol{F_g} \sin\alpha$. Further, to quantify this dissipation we can again adapt Stokes law, Eq (3.3), to obtain an effective drag viscosity. From the velocity of the disk in the texture with $p = 60\ \mu m$ and $\alpha = 70^{\circ}$ shown in Fig. 3.6, we obtain a very large value, $\eta_{eff} = 1080\ mPa \cdot$

s. (We again stress that this quantity should not be considered literally as the shear viscosity of the cholesteric but rather as a measure of the dissipation for comparison with other sedimentation conditions.) As before, we interpret this large dissipation as the consequence of contributions from motion of the disclination lines, which experience considerable deformation by the moving disk at this orientation of the texture.

The range of angles α at which the disks either displayed stick-slip motion or moved at a constant velocity parallel to the disclinations depended on the size of the pitch. For small pitch, where no stick-slip motion was observed even at $\alpha = 0$ the disk velocity was parallel to the disclinations at all α (except at $\alpha = 0$ where the component of gravity parallel to the disclinations was zero and hence the velocity was zero). For larger pitch and at intermediate α, the disk dynamics could be considered a hybrid of the two types of motion seen at large and small α. That is, during their motion the disks moved parallel to the disclinations and hence at an angle to the applied force at times, but the texture also periodically yielded so that the disks could traverse the texture from one period to the next. Fig. 3.7, which displays a series of bright-field micrographs of a disk in a texture with $p = 114\ \mu m$ at $\alpha = 42^{\circ}$, illustrates this motion. Fig. 3.8(a) shows the zigzag trajectory made by the disk depicted in Fig. 3.7, while Fig. 3.8(b), which shows its time-dependent velocity as it traversed two periods of the texture, illustrates its stick-slip motion. Notably, the disk's direction of motion as it traversed each period of the texture unencumbered by the disclinations was not strictly vertical and parallel to gravity but instead was oriented farther toward the cholesteric axis. We attribute this deflection of the velocity from the direction of the applied force to a lift force created by the anisotropic drag in these regions of the texture.

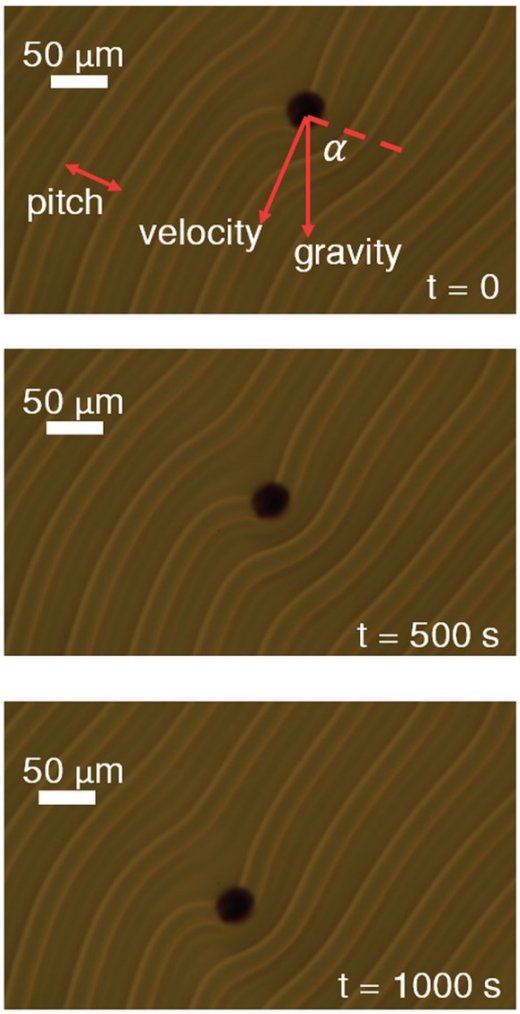

Figure 3.6: Images of a Ni disk sedimenting through a cholesteric finger texture with 60 µm pitch in response to gravity oriented at an angle $\alpha = 70°$ to the cholesteric axis. The disk moves perpendicular to the axis. The time interval between successive images is 500 s.

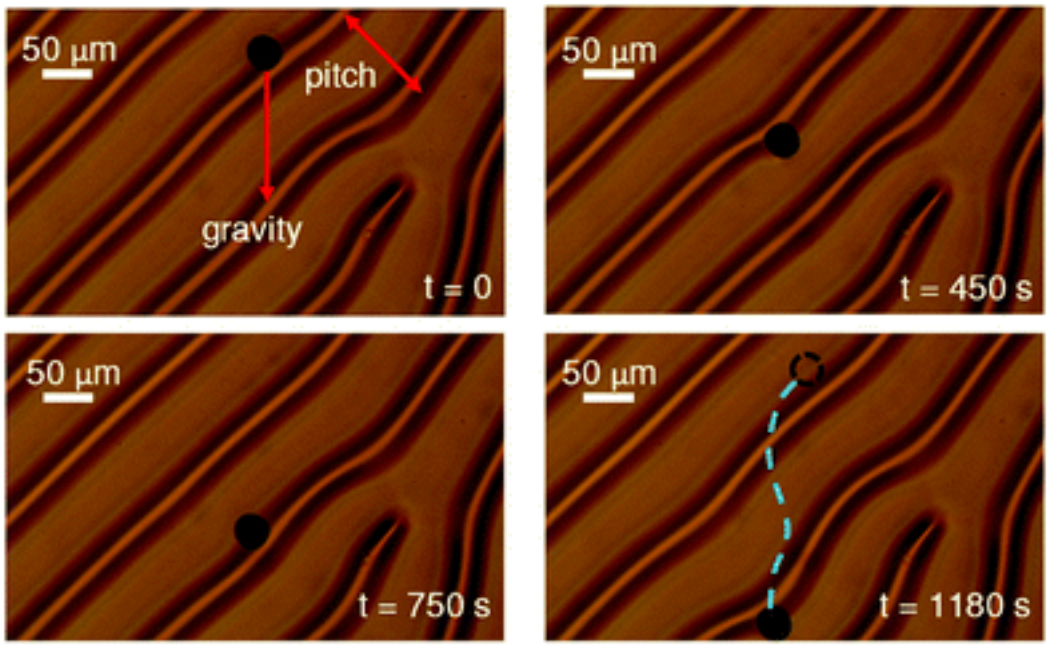

Figure 3.7: Images of a Ni disk sedimenting through a cholesteric finger texture with 114 µm pitch in response to gravity oriented at an angle $\alpha = 42°$ to the cholesteric axis. The time in each image matches the time axis of Fig. 3.10(b). The dashed line denotes the trajectory of the disk.

3.4 Model for Stick-Slip Motion

As the descriptions above illustrate, the response of the cholesteric finger texture to colloidal motion is highly anisotropic and non-Stokesian. A key ingredient of this response is the behavior of the periodic array of disclinations, whose distortion gives rise to the anomalously large drag and to the stick-slip motion. To model the forces that create the stick-slip motion, we characterized the distortions in the texture by measuring the length and positions of the sets of disclinations in the vicinity of sedimenting disks undergoing the motion. From these measurements we identified two contributions to the elastic energy cost of distorting the texture: one from stretching the disclinations and one from compressing the cholesteric pitch. However, as described below, in modeling the effect of these energy costs on the disk motion, we found that the contribution from the compression could be neglected. For simplicity, we therefore focus on the stretching energy, which we approximate as

$$U_s = T \sum_i \Delta L_i = T \Delta L_{total} \tag{3.4}$$

where ΔL_i is the excess length of the ith set of disclinations, and T is the energy per unit length, or line tension, of the disclinations. For example, Fig. 3.5(b) depicts the time-dependent length ΔL in excess of the undistorted length of the five sets of disclinations labeled in the top image in Fig. 3.4 along with their sum ΔL_{total}. This energy cost leads to a force on a disk,

$$F_e = -\frac{dU_s}{dy} = -T\frac{d(\Delta L_{total})}{dy} \tag{3.5}$$

where y is the vertical position of the disk. Fig. 3.9 displays the results for ΔL_{total} from Fig. 3.5(b) plotted as a function of y. We note that the oscillating nature of ΔL_{total} implies that the direction of F_e similarly oscillates. In contrast, one might expect that this

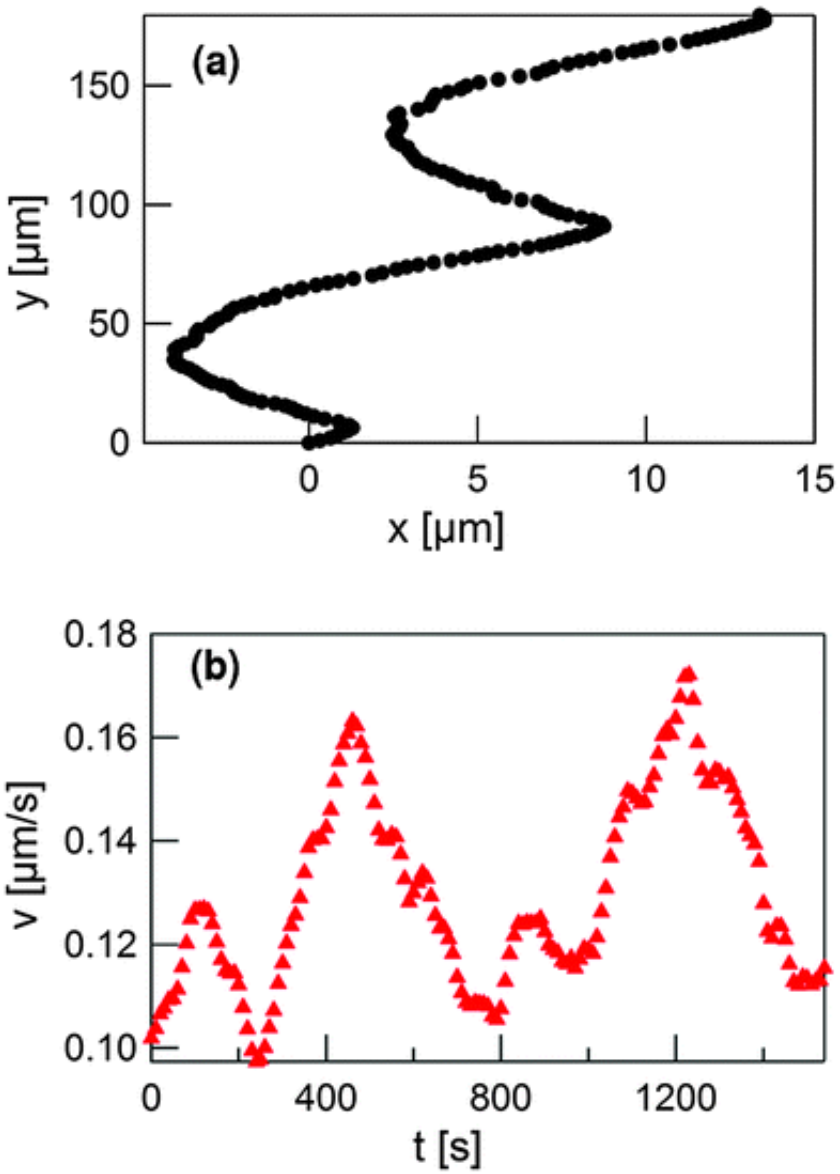

Figure 3.8: (a) Trajectory and (b) magnitude of velocity of the nickel disk in Fig. 3.7 sedimenting through a cholesteric finger texture with 114 μm pitch in response to gravity oriented at an angle α= 42° to the cholesteric axis. Note the positive-y direction is defined as downward (parallel to gravity).

force, which is associated with stretching the disclinations, acts on a disk only when it is actually stretching the disclinations and ΔL_{total} is increasing, and that all the elastic energy stored in the disclinations is lost to viscous dissipation as they retract. However, measurements of the stick-slip motion in textures with large p, where the motion of the disks when they were not touching any disclinations could be clearly resolved, showed that during this part of the motion the disks actually accelerated, suggesting the presence of an increasing downward force working in conjunction with gravity. The oscillating nature of ΔL_{total} captures both the retarding nature of the disk's interaction with the disclinations due to stretching and this downward force.

In addition, we model the viscous dissipation during the stick-slip motion by a Stokes drag, Eq (3.3). At low Reynolds number, the gravitational force on the disk is hence balanced by these elastic and drag forces, leading to an equation of motion for the disk,

$$F_g = F_d + F_e = \frac{32}{3} R\eta_{eff}\boldsymbol{v} + T\frac{d(\Delta L_{total})}{dy} \tag{3.6}$$

In principle, one can solve this equation to obtain a prediction for the position of the disk as a function of time. However, because of the scatter in ΔL_{total}, direct differentiation of the data to obtain F_e is impractical. Therefore, to compare the model with the data, we integrate Eq (3.6) to obtain:

$$y_2 - y_1 = \frac{32R}{3F_g}\eta_{eff}\int_{y_1}^{y_2} v dy + \frac{T}{F_g}[\Delta L_{total}(y_2) - \Delta L_{total}(y_1)] \tag{3.7}$$

where y_1 and y_2 are two values of the disk's position. Using the values of the disk velocity from Fig. 3.5(a) and the excess length of the disclinations from Fig. 3.9 as inputs, we fit Eq (3.7) to the data for the disk position with η_{eff} and T as free parameters.

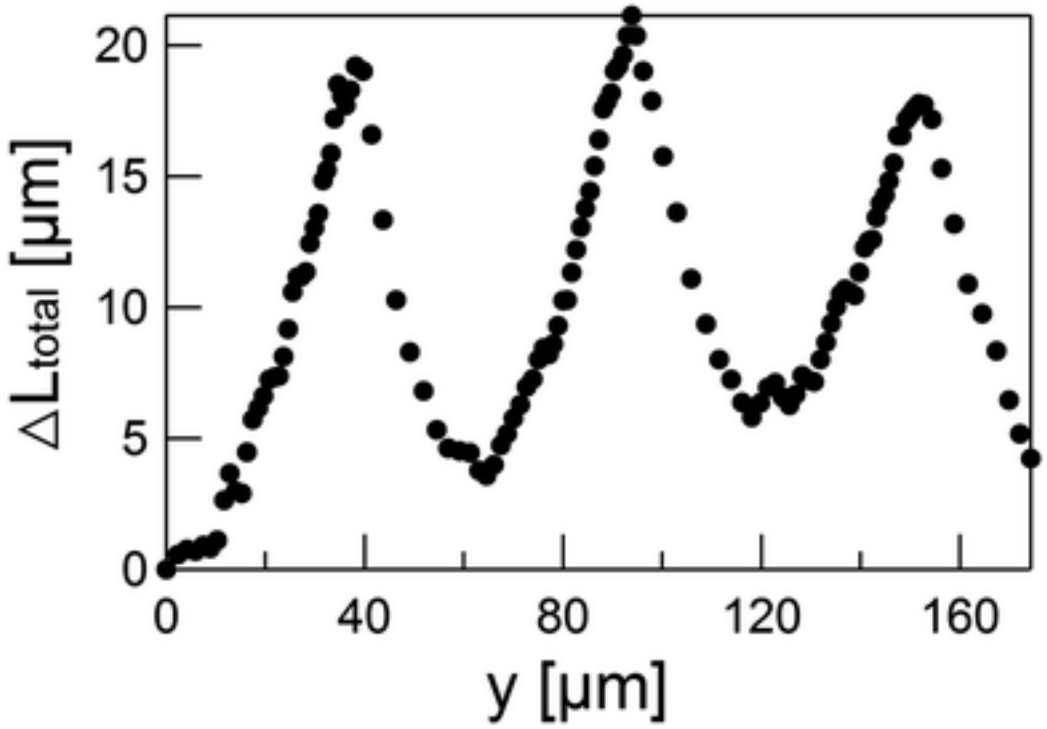

Figure 3.9: Total excess length of the disclinations ΔL_{total} from Fig. 3.5(b) plotted as a function of disk height.

The result of the fit, shown by the solid red line in Fig. 3.5(a), agrees closely with the measurements. The best fit value for the effective viscosity, $\eta_{eff} = 680\, mPa \cdot s$, again indicates an anomalously large drag reflecting the dissipation associated with motion of the disclinations. The best fit value for the disclination line tension, $T = 13.6\, pN$, can be compared with the theoretically expected tension of the four (nonsingular) λ-disclinations in each period of the finger texture:

$$T = 4\pi K s^2 Ln\left(\frac{L}{r_c}\right) \tag{3.8}$$

where $K \approx 5\, pN$ is the average Frank elastic constant of 5CB [66], $s = 1/2$ is the strength of the λ disclinations, L is the effective size of the system, and r_c is the disclination core radius. The core radius of the λ-disclinations is approximately the pitch p [17]. Taking L to be the spacing between the substrates, we hence expect $Ln(\frac{L}{r_c})$ to be of order one, and hence the tension to be a few times K, which is in good agreement with the fit result. Further, from T and estimates of $\frac{d(\Delta L_{total})}{dy}$ at the yield points, we find that the maximum stretching force at yielding is approximately $12 \pm 2\, p$N for $p = 60\, \mu m$. This yield force, which depends on the pitch, derives from several factors including K and the strength of the anchoring at the particle surface. Its important feature is its similarity to the sedimentation force F_g, which leads to the complex dynamics displayed by the disks.

As the remarkable agreement between the model for the stick-slip motion (Eq (3.7)) and the measured results for the disk position demonstrates, the model appears to capture the key ingredients involved in causing the periodic motion through the finger texture. This agreement is perhaps surprising given the simplicity of the model and the

approximations that it makes. For example, by approximating the viscous dissipation in terms of a single effective viscosity through Stokes law, the model neglects the full complexity of viscous drag in liquid crystals. As mentioned in the Introduction, the drag on a colloidal particle moving in a liquid crystal depends on its direction of motion with respect to the surrounding director field. Since the orientation of the director varies as a function of position within each period of the finger texture, the viscous drag on the disk should similarly vary with position. This spatial variation is compounded by the contribution to the dissipation from the motion of the disclinations, which also varies as the disk traverses each period in the stick-slip motion. In addition, due to the spatial variation of the director field in the cholesteric texture, the distortion imposed on the director by the disk beyond stretching the disclinations should vary with position, and hence the elastic energy cost of that distortion should also vary. Such a gradient in distortion energy should further give rise to a force on the particles [65, 67, 68]. As mentioned above, the form of F_e includes both a retarding force when the disks are attached the disclinations and stretching them as well as an accelerating force during detachment, and this accelerating component could be serving to approximate some of these effects. Nevertheless, the good agreement between the model prediction and the data in Fig. 3.5(a) demonstrates that the overwhelming contribution to the forces on the disk in the finger texture that creates the stick-slip motion is from interactions with the disclinations.

3.5 Discussion on Compression Energy in Stick-Slip Model

A noteworthy feature of the disk's effect on the texture was that not only did the

disclinations attached to the disk change length as the disk fell but so did nearby disclinations. For instance, during the time the set of disclinations labeled C in Fig. 3.4 were in contact with the disk (the time interval 420 s to 800 s in Fig. 3.5(b)), not only did ΔL of that set of disclinations go through a maximum as the disk stretched them and then detached but so did ΔL for the set of disclinations immediately below the disk, labeled D, and to a lesser extent the next set below, labeled E. We associate the distortion of these neighboring disclinations with the tendency of the finger texture to maintain a preferred periodicity. This preference implies an energy cost to compressing (or expanding) the texture, which we approximated as

$$U_{compress} = B \sum_i \int (h_i(s) - p)^2 ds \tag{3.9}$$

where the integral is along the contour of each set of disclinations, $h_i(s)$ is the perpendicular distance from the local contour of set i of disclinations to the next set, $i + 1$, and B is a coefficient setting the compression energy. As mentioned above, in modeling the effect of the energy costs associated with distorting the texture on the disk motion, we found that the contribution from this compression energy could in fact be neglected. That is, the quality of fits using the model to describe the data was statistically indistinguishable when we set $B = 0$ and when we allowed B to be a free parameter.

3.6 Conclusion

In conclusion, these experiments to investigate the mobility of discoidal particles in cholesteric finger textures have illustrated the novel behavior that can occur as part of sedimentation within structured fluids. The broken translational symmetry of the finger

textures and the organized array of defects that are inherent to the textures provide a means to spatially modulate mobility in a way that is sensitive to the size of the particles relative to the structural length scales that characterize the fluid. Further, the ability of the disclinations in the texture to redirect the disks away from the direction of externally applied forces (such as gravity) illustrates the potential of such particle–defect interactions for manipulating colloids. In particular, while the ability to channel colloidal particles through their interactions with defects, for example in microfluidic environments, has been demonstrated previously [69], the present work highlights the varied behavior that can occur when these interactions compete with other forces. Experiments that explore the possibility of similar phenomena in colloidal transport within other structured fluids with broken translational symmetry and ordered defects, such as the blue phase of liquid crystals and smectic liquid crystals in wedge samples, would test the generality of this behavior and its potential for applications.

Chapter 4

Colloidal Transport within Nematic Liquid Crystals with Arrays of Obstacles

4.1 Introduction

When colloidal particles are suspended in a liquid crystal, the anisotropic viscous and elastic properties of the liquid crystal introduce a host of novel phenomena. For example, in a nematic liquid crystal, the boundary conditions created by the anchoring of the nematic director at the particle surface introduce distortions and defects in the surrounding director field, with corresponding costs in the free energy of the liquid crystal [20,65,70-76]. The minimization of these energy costs can, in turn, engender forces on the particles that lead to remarkable and unexpected results, such as the levitation of particles in opposition to gravity [58,65,67,77] and the formation of stable colloidal crystals [78-81]. In addition, the anisotropy of the nematic, and the effects of flow on the orientational order, can make the mobility of inclusions both velocity and direction dependent, and can cause striking dynamical phenomena not seen in isotropic fluids [24,58,59,67,82-95]. Such observations have made inclusions in liquid crystals valuable for exploring fundamental issues of liquid-crystal viscoelasticity and interfacial phenomena, particularly as they relate to topological defects. They have also motivated interest in employing the interactions within liquid crystals as a mechanism for colloidal

manipulation [68,69,85,91,92,96-99] and self-assembly that is intrinsically and uniquely anisotropic.

Recently, research has expanded on this theme of colloidal manipulation and assembly through liquid crystal elastic forces to investigate the behavior of colloids within patterned director fields [68,101,102]. Spatially modulated colloidal transport has been demonstrated previously in liquid crystals with intrinsically periodic structures, such as cholesterics [62,103]. An example of such work is the study of colloidal mobility through cholesteric finger textures described in the previous chapter. Here, I address the possibility of engineering such modulation through patterned anchoring by exploiting the periodic director field configurations that form within arrays of obstacles within microfluidic devices. These studies build on research on colloidal transport in simple liquids in microfluidic devices containing engineered arrays of obstacles that drive the particles on precisely controlled paths that depend on the particle size [100, 104-118]. We find similarities in the behavior of the colloids in the nematic with that in the isotropic liquids but also some notable differences. Most significantly, the velocity of the colloids through the array displays a pronounced modulation that we identify as the consequence of the combined effects of a spatially varying effective drag viscosity and elastic forces between the colloids and the obstacles.

4.2 Experimental Procedures

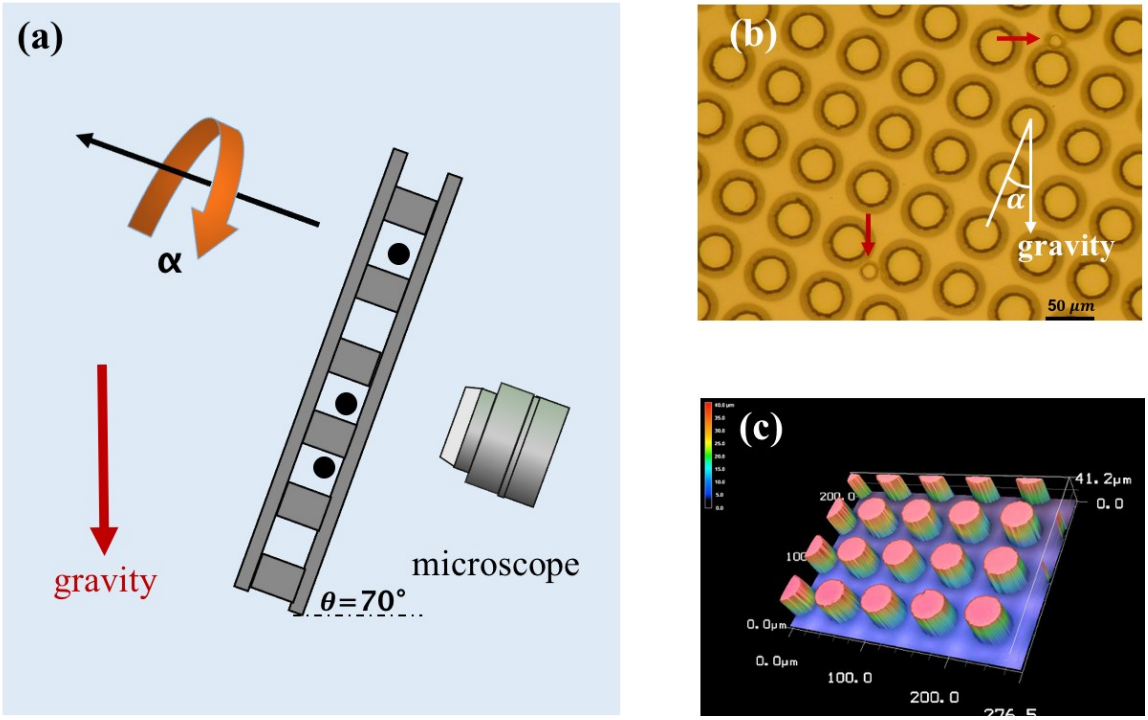

Figure 4.1. Schematic of experimental setup and structure of microfluidic device. (a) Microfluidic device was placed on the stage with tilt angle θ = 70°. (b) micrograph of micropost array filled with nematic 5CB and silica microspheres. Red arrows point to microspheres. (c) three-dimensional view of the periodic array of obstacles under confocal microscopy.

Colloidal transport through the microfluidic post arrays was characterized by classic "falling ball" experiments in which particles with a density larger than that of the surrounding fluid were driven through the array by gravity, as illustrated in Fig. 4.1(a). The arrays were fabricated from PDMS using the procedures described in Chapter 2. Briefly, a square lattice of circular holes arranged in a square lattice was created in a film of photoresist (SU8 2050, Microchem Corp., MA) that had been spin coated on a silicon wafer. This array was then employed as a mold for making the arrays of circular posts on a PDMS film. The height of the posts was determined by the thickness of photoresist, which was about 40 μm, as illustrated in Fig. 4.1(a), which displays an image of an array obtained from confocal microscopy. The diameter of the posts was 35 μm and their spacing in the square lattice was 60 μm. Since bare PDMS surfaces impose weak planar anchoring of the nematic director, the PDMS containing the post arrays was functionalized with N,N-Dimethyl-N-octadecyl-3-aminopropyltrimethoxysilyl chloride (DMOAP) to achieve strong homeotropic anchoring. We bonded the PDMS post arrays to a sheet of flat PDMS by oxygen plasma in order to create an enclosed environment. During the UV exposure the region of the PDMS containing the post array was shielded to preserve the DMOAP functionalization. The flat sheet of PDMS forming the top of the device was left unfunctionalized and hence imposed weak planar anchoring. Two small holes punched into the sheet prior to the bonding served as channels for introducing the 5CB. Untreated Silica spheres with density of $2 g/cm^3$ and diameter between $10 - 20\,\mu m$ were premixed with 5CB at low concentration, and the mixture was then introduced through the channels in the PDMS into the microfluidic device. Once filled,

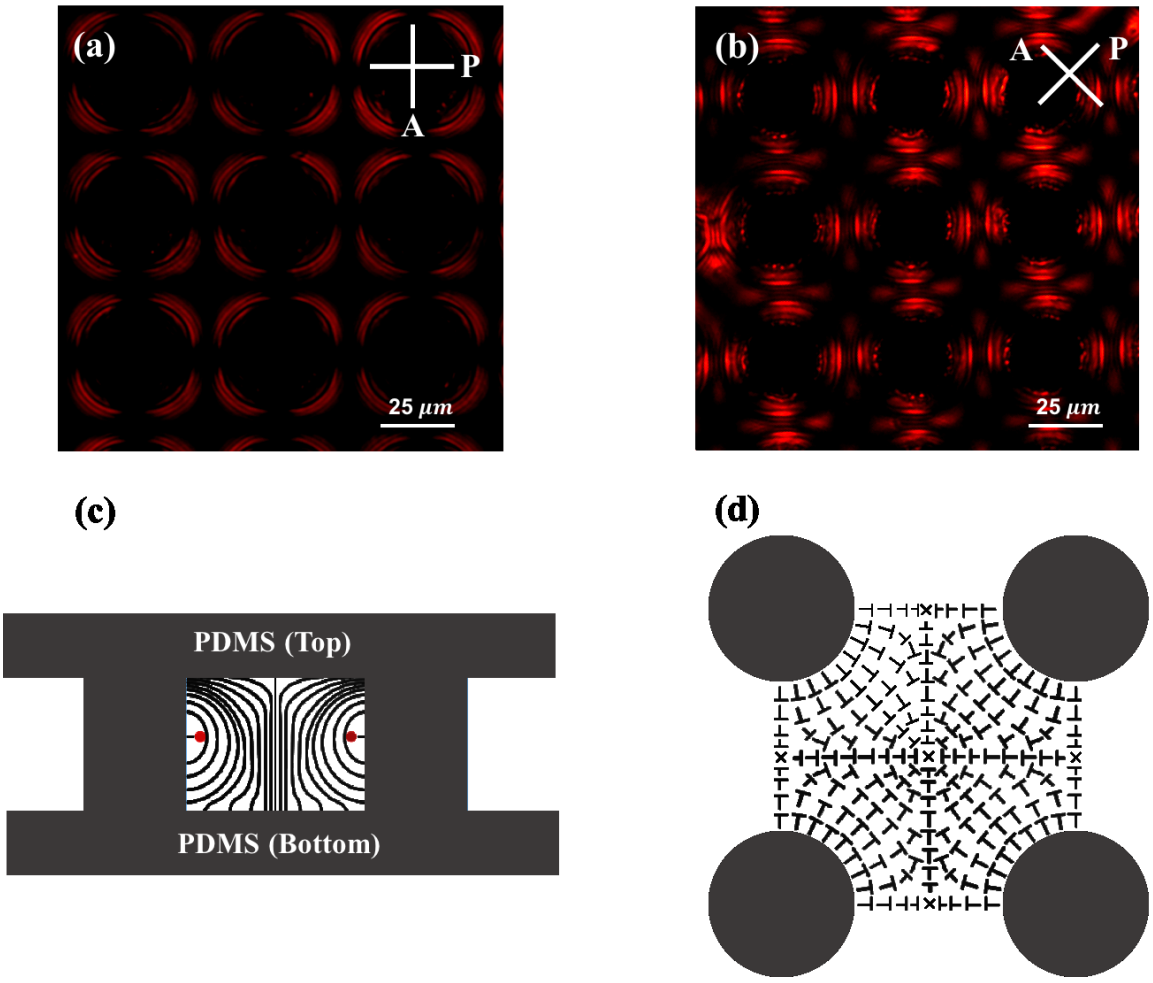

Figure 4.2. Director field of nematic 5CB within microfluidic device. (a-b) microscopic images under crossed polarizers. (c) side-view of 5CB director field between two posts. Red dots represent the +1/2 disclination rings. (d) top-view of director field underneath the top surface. Director field escapes into the vertical direction at the center of two posts and the center of four posts. Dark circles are PDMS cylinders.

the device was heated to 40 ℃ and allowed to cool slowly to erase any dependence of the director field on flow during the filling.

The anchoring conditions on the PDMS surfaces created a periodic director field configuration within the array that I characterized using polarization microscopy images like those shown in Figs. 4.2(a) and (b). Schematic representations of the director field are shown in Figs. 4.2(c)-(d). Due to the homeotropic anchoring on the posts, a strength ½ disclination ring encircles each post. I note that Cavallaro *et al*. [101] employed fluorescence confocal polarization microscopy and numerical modeling to determine the nematic director field within micropost arrays of similar geometry and also observed such disclination rings. (The geometries of the system Cavallaro *et al*. [101] studied and that of my devices were not identical in that theirs had homeotropic anchoring on all surfaces, while the top of my device had weak planar anchoring.)

To conduct the measurements, I mounted the microfluidic devices on a rotatable stage of an optical microscope (Nikon). The microscope was tilted so that the focal plane was at an angle $\theta = 70°$ with respect to gravity as shown in Fig. 4.1(a). By rotating the stage through an angle α, the direction of the component of gravity parallel to the focal plane could be varied with respect to the symmetry direction of the post array.

4.3. Experimental Results

4.3.1 Periodic Velocity Modulation along $\alpha = 0$

When the post arrays were oriented so that the gravitational force was parallel to a symmetry axis of the lattice ($\alpha = 0$), the colloidal particles could traverse the lattice unobstructed by translating along the interstitial region between columns of post as

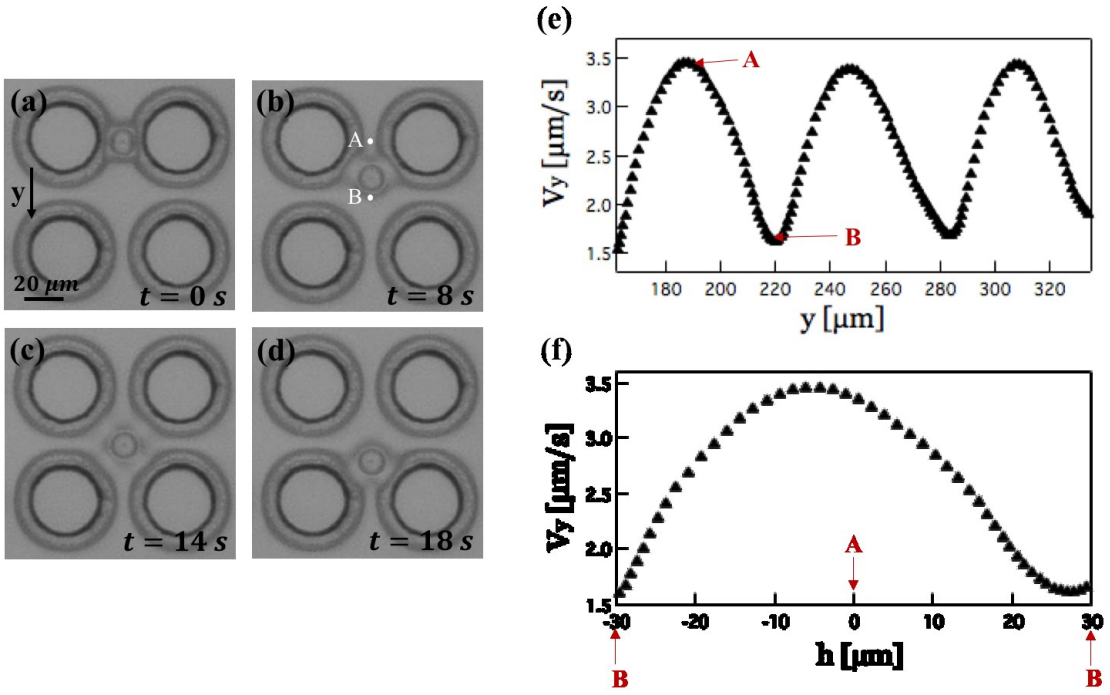

Figure 4.3. Microsphere translating through nematic 5CB within post array. (a-c) Micrographs of spheres moving inside the microfluidic channel. (e) Varying speed along y direction. **A** (center of two posts) and **B** (center of four posts) correspond to positions in (b). Origin of y is set as the particle position when we started to record the motion. Here we took three periods after the motion was stable (f) Varying speed within a period.

depicted in the series of micrographs in Figs. 4.3(a)-(d), which show a sphere with radius 6.08 μm descending through an array. However, interactions between the spheres and posts mediated by the liquid crystal, as well as the anisotropic viscosity of the nematic, led to a pronounced modulation in the velocity of the colloids following these paths. For example, Fig. 4.3(e) shows the velocity of the sphere shown in Figs. 4.3(a)-(d) as a function of position as it traverses three periods of the array. Fig. 4.3(f) shows the velocity through a single period on an expanded scale with vertical position h measured with respect to the position of the post centers indicated by the dashed line in Fig. 4.3(d). As the sphere approaches this height (h = 0), the speed increases, and reaches a maximum at the value h slightly less than 0. After passing between the posts, velocity decreases until it reaches a minimum when the sphere approaches the midway point between two rows of posts.

To understand the origin of this velocity modulation, I consider the forces on the sphere as is moves through the array: gravity, viscous drag, and elastically mediated interactions between the sphere and posts. Under the low Reynolds number conditions of the sphere motion ($Re \sim 10^{-6}$), these forces sum to zero,

$$\boldsymbol{F}_g + \boldsymbol{F}_{drag} + \boldsymbol{F}_{el} = 0 \tag{4.1}$$

Taking account of the buoyancy force and the tilt angle θ, $F_g = V_{SiO_2}\left(\rho_{SiO_2} - \rho_{5CB}\right)g \cdot \sin\theta$. Further, as discussed in Chapter 1, at sufficiently small velocity (i.e., small Ericksen number, $Er \sim 0.1$), the drag on a particle translating through a nematic liquid crystal can be approximated by Stokes drag,

$$\boldsymbol{F}_{drag} = -6\pi R\eta_{eff}\boldsymbol{v} \tag{4.2}$$

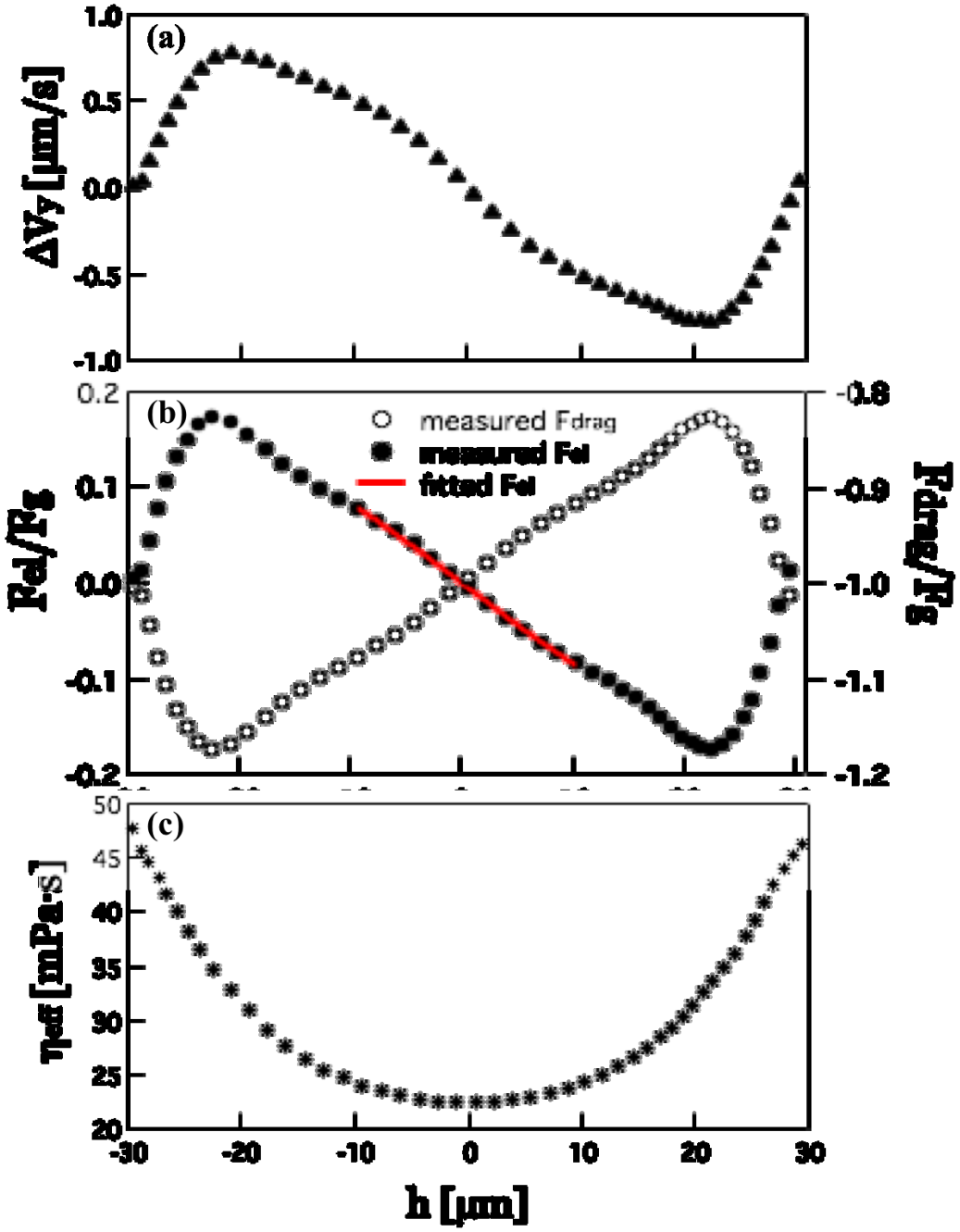

Figure 4.4. (a) The variation of Δv within one period for the sphere shown in Figs. 4.3(a)-(c). (b) The elastic force F_{el} (solid circles) and F_{drag} (open circles) at different positions within one period. The forces are normalized by the gravitational force. Red line plots the result of fitting Eq (4.15) to F_{el} between $h = -10\ \mu m$ and $h = 10\ \mu m$. (c) The variation of the effective drag viscosity within one period. The viscosity is symmetric about $h = 0$.

where $6\pi R$ is the geometric coefficient for a sphere with radius R, η_{eff} is the effective drag viscosity and $\boldsymbol{v}$ is the velocity of the sphere. Since the director field in the post array is spatially varying, the viscous drag in principle is spatially varying. We assume that both the effective viscosity and the particle-post interactions have the periodicity of the lattice and hence can be expressed as functions of h: $\eta_{eff} = \eta_{eff}(h)$ and $E_{el} = E_{el}(h)$. The same is thus the case for the elastic force, $F_{el} = -dE_{el}/dh = F_{el}(h)$. Therefore, Eq (4.1) can be written as:

$$F_g - 6\pi R\eta_{eff}(h)\, v(h) + F_{el}(h) = 0 \tag{4.3}$$

Here, each term is expressed as a scalar when we choose the positive y direction to be parallel to gravity.

Furthermore, images of spheres traversing the array, such as Figs. 4.3(a)-(d), indicate that the distortions of the director field induced by the sphere are symmetric about $h = 0$, implying,

$$\eta_{eff}(h) = \eta_{eff}(-h) \tag{4.4}$$

$$E_{el}(h) = E_{el}(-h) \tag{4.5}$$

$$F_{el}(h) = -F_{el}(-h) \tag{4.6}$$

Hence, if we consider the force equation, Eq (4.3), when the particle is at position $-h$, we have:

$$F_g - 6\pi R\eta_{eff}(-h)\, v(-h) + F_{el}(-h) = 0 \tag{4.7}$$

With Eq (4.4) and Eq (4.6), this expression can be written as:

$$F_g - 6\pi R\eta_{eff}(h)\, v(-h) - F_{el}(h) = 0 \tag{4.8}$$

And, subtracting this result from Eq (4.3), we get:

$$2F_{el}(h) = 6\pi R\eta_{eff}(h)\, \Delta v(h) \tag{4.9}$$

where $\Delta v(h) = v(h) - v(-h)$.

Results for $\Delta v(h)$ are plotted in Fig. 4.4(a). With these results and Eq (4.9), one can attain the spatially varying drag viscosity and elastic interactions experienced by the colloid as it traverses the array. Specifically, solving Eq (4.9) for $\eta_{eff}(h)$ and inserting it back into Eq (4.3), we get a relationship for the elastic force:

$$F_{el}(h) = -\frac{1}{1 - \frac{2v(h)}{\Delta v(h)}} F_g \tag{4.10}$$

Furthermore, the Stokes drag and effective viscosity are obtained as:

$$F_{drag}(h) = -F_g - F_{el}(h) = -\frac{2v(h)}{2v(h) - \Delta v(h)} F_g \tag{4.11}$$

$$\eta_{eff}(h) = \frac{F_g}{3\pi R\big(2v(h) - \Delta v(h)\big)} \tag{4.12}$$

Eqs (4.10)-(4.12) thus provide the elastic force, Stokes drag, and effective viscosity. The results for these quantities, obtained from the velocity data in Fig. 4.3, are shown in Figs. 4.4(b) and (c).

As expected from symmetry, $F_{el} = 0$ when $h = 0$ and $h = \pm H/2$, At any point in the particle's trajectory, the force is directed toward the closest row of posts, so that at $h < 0$ the force is downward (positive), and at $h > 0$ it is upward (negative). Over a broad range of positions centered at $h = 0$, the force is linear in the displacement from $h = 0$, indicating an effective Hookean interaction. To interpret the origin of this force, we consider the change to the director field when the sphere comes in proximity to a pair of posts. As the images in Figs. 4.3(b) and (d) indicate, the sphere distorts the director field in the volume of fluid between the sphere and posts depicted schematically in Fig.

4.5. We can approximate the size of this volume as $V = 2\pi R^2 l$, where l is the distance between the surfaces of the sphere and posts and is given by

$$l = \sqrt{\left(\frac{H}{2}\right)^2 + h^2} - R_p - R \tag{4.13}$$

We can further approximate the elastic energy density stored in this region as $E_{el} = KV(\nabla \boldsymbol{n})^2$, where K is the average Frank elastic constant, and $\nabla \boldsymbol{n}$ is the gradient in the director. The incompatible boundary conditions between the sphere and post surfaces suggest we approximate the gradient as $(\nabla \boldsymbol{n})^2 \approx l^{-2}$. Thus,

$$E_{el} = \frac{2\pi R^2 K}{l} \tag{4.14}$$

and,

$$F_{el} = -\frac{dE_{el}}{dh} = -\frac{2\pi R^2 K}{l^2}\frac{dl}{dh} \tag{4.15}$$

At small h, this elastic force reduces to a Hookean form,

$$F_{el}(h) = -\frac{4\pi R^2 K}{H\left(\frac{H}{2} - R - R_p\right)^2} h \tag{4.16}$$

Thus, in the limit of small h, the dependence of the distorted volume on sphere position leads to a Hookean restoring force. The solid line in Fig. 4.4(b) shows the result of fitting the force over the range $-10\,\mu m < h < 10\,\mu m$, using Eq (4.16), with K as the free parameter. The value obtained from the fit $K \approx 0.4$ pN. Compared with the order as the room-temperature average Frank elastic constant of 5CB, which is $K_{5CB} \approx 4$ pN [10,13], our fitted K is relatively small. We attributed this small value to the missing contribution to the elastic energy. As a matter of fact, the total elastic energy stored in particle-post system includes two terms: (i) the distortion energy stored in the volume between particle

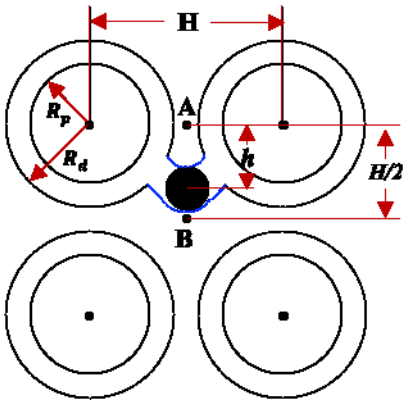

Figure 4.5. Schematic of particle-post system geometry. The circles enclosed by solid line are cylindrical posts, with radius R_p. The black dashed lines represent the outline of the defect ring around each post with a distance R_d from the post center, while the blue dashed lines represent the highly distorted area stretched by the sphere. Solid black circle is the silica microsphere. The period of array is H. Positions A and B are the same as previously labeled in Fig. 4.3: the center of two post ($h = 0$) and the center of four posts ($h = H/2$) respectively.

and post, which is expressed in Eq (4.14), and (ii) the elastic energy around the particle, which is exclusively decided by the director field on the particle surface. The second term is larger at $h = 0$ because of the tight confinement, while small at $h = \pm H/2$ because of loose confinement. Therefore, the elastic force caused by this energy behaves the opposite way as the force we consider in Eq (4.14), further reducing our estimation of real K magnitude.

The spatially varying viscous drag and effective viscosity are plotted in Figs. 4.4(b)-(c), respectively. The effective viscosity η_{eff} decreases as the sphere translates toward the passage way between two posts, reaching a minimum at $h = 0$, before increasing again after it passes through. The variation in the effective viscosity, $\eta_{eff}(\pm\frac{H}{2})/\eta_{eff}(0)$, is about 1.5. This magnitude of anisotropy is approximately equal to the variation in drag that colloids experience in 5CB when they move parallel versus perpendicular to the director. Due to the spatial variation in the director in the microfluidic array, the colloid experiences a changing local director field as it traverses the array, and this variation should contribute to the change in effective viscosity with position. However, given the relatively large variation in Fig. 4.4(c), we believe a second contribution is playing a role. Specifically, the microscopy images indicate that when the sphere is between two posts, at $h = 0$, the incompatible boundary conditions on the sphere and post surfaces suppress the nematic order between the sphere and posts further contributing to the relatively small effective drag viscosity in this region [66].

4.3.2 Interaction Between Colloid and Isolated Post

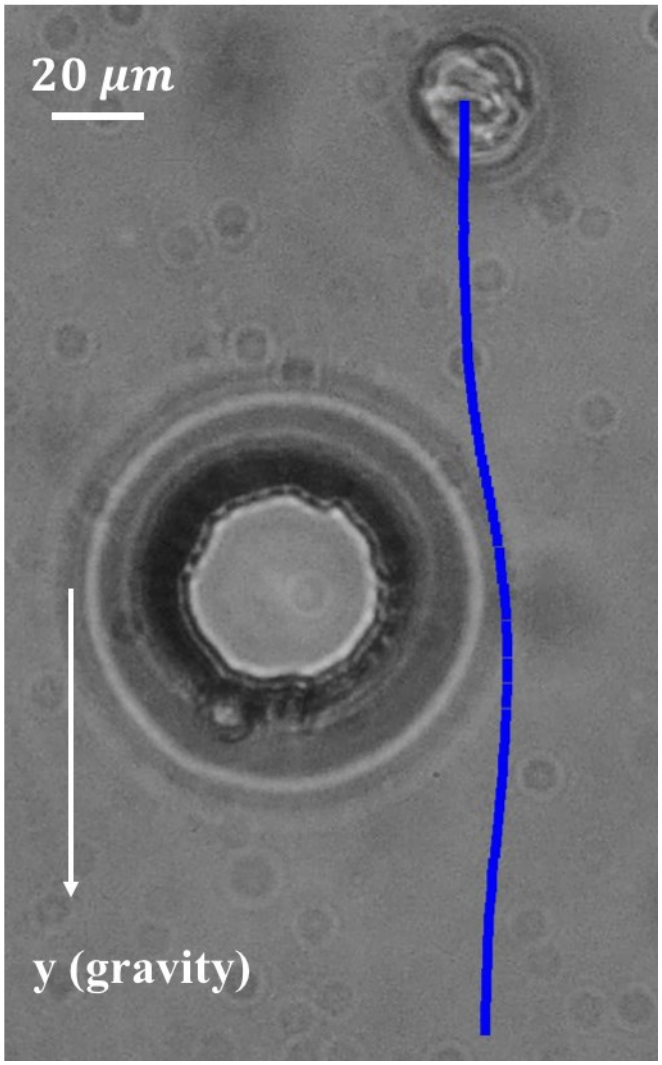

Figure 4.6. The trajectory of a microsphere translating near an isolated post. Blue line represents the trajectory.

A somewhat surprising aspect of the elastic interaction between the posts and sphere that is observed in the arrays is its attractive nature since naively one would expect the differing boundary conditions on the two (homeotropic on the posts, planar on the spheres) would lead to a repulsion, at least as small distances. To understand this interaction better, we performed additional measurements within arrays in which the lattice spacing (i.e., the distance between posts) was much larger to characterize the behavior of colloids near isolated posts. Fig. 4.6 displays the trajectory of silica sphere with radius 10 μm translating under the force of gravity in the vicinity of a post with radius of approximately 30 μm. When the sphere was far from the post, only the viscous drag force and gravity acted on particle, leading to constant velocity along the y direction. However, when the sphere was near the post, its trajectory deflected away from the post, consistent with a short-range repulsive interaction. The range in which this interaction is appreciable, inferred from the distance over which the sphere trajectory deviates from a straight line, is about 80 μm, which is about twice the spacing between the substrates, suggesting any longer-range interactions are screened by the substrates. This evidence for a repulsive interaction between an isolated post and sphere thus indicates how confinement within the lattice alters qualitatively the nature of the sphere-post interaction.

4.3.3 Directional Locking

As mentioned above, a key motivation for investigating the transport of colloidal particles in nematics within microfluidic post arrays was the transport behavior observed in such arrays containing a simple isotropic liquid. Specifically, as Drazer and coworkers [112-117] have explored in detail, when the angle α between the driving force (gravity)

and the columns of posts is varied continuously, the direction of propagation of the colloids through the lattice changes discretely, in a manner that depends on geometric considerations, specifically on the relative sizes of the posts, lattice spacing, and colloids. In order to understand how this behavior might be varied and potentially controlled through the interactions between the posts and colloids mediated by a nematic fluid, we investigated the propagation of the colloids through 5CB within the arrays as a function of α and compared the behavior to that seen in equivalent measurements performed in water.

Employing silica spheres with diameters around $15\ \mu m$, we found that the spheres exhibit directional locking by selecting among only three propagation directions through the lattice is α is varied from 0 to 45 degrees. These directions, which can be labeled based on their lattice vector $[p, q]$, as $[0,1]$,$[1,2]$ and $[1,1]$, are illustrated in Figs. 4.7(a)-(c). Fig. 4.7(d) shows the migration angle, defined as the angle between the propagation direction and the [0,1] direction as a function of α. When the angle between the force and [0,1] direction is small, the particle motion remains locked with the lattice in the [0,1] direction; when the angle between force and lattice [0,1] direction is close to $45°$, the particle direction is locked with the lattice in the [1,1] direction; while when the angle between the force and [0,1] direction is intermediate: the particle direction is locked to lattice [1,2] direction and exhibits a doubly periodic motion. The angle at which the particle direction transitions from being locked to [0,1] to locked to [1,2] is approximately $12°$, and the transition angle from [1,2] to [1,1] is approximately $25°$. We note that the Peclet number in the experiment can be estimated by

$$Pe = F_g R / k_B T \tag{4.17}$$

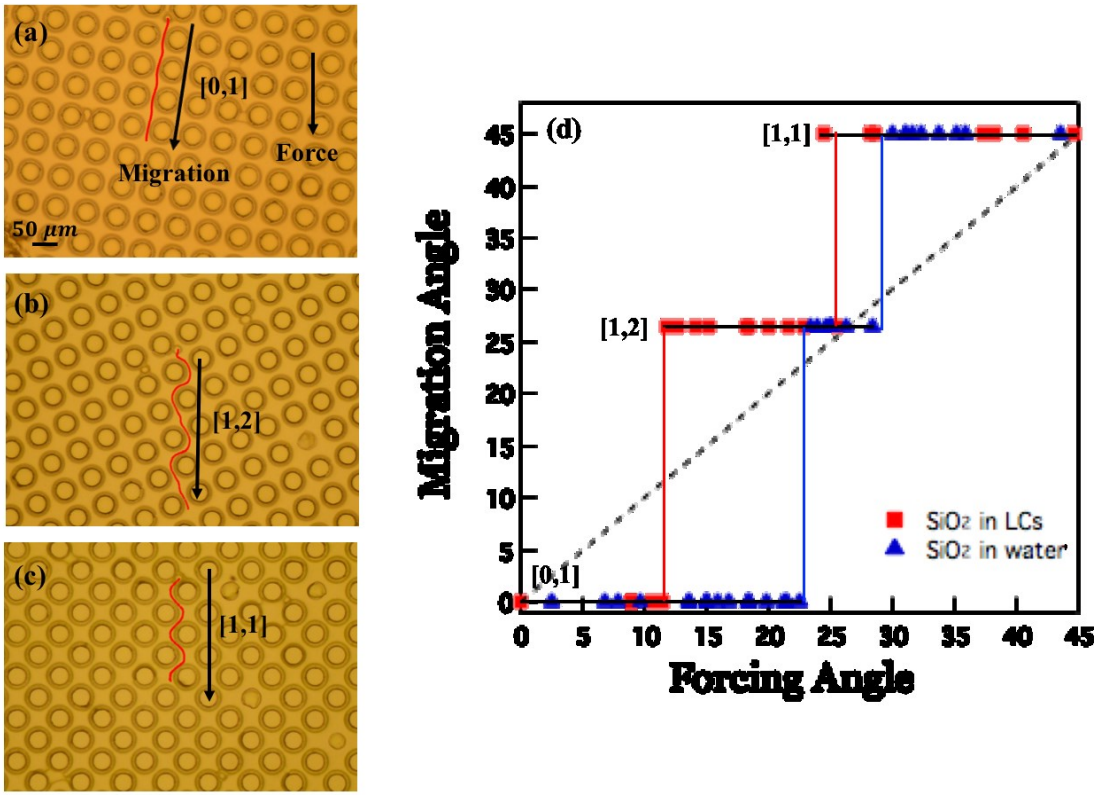

Figure 4.7. Directional locking of silica microspheres translating in post array within nematic 5CB. (a-c) illustrate three locking directions observed in the experiment. (a) migration direction locked into [0,1] (b) migration direction locked into [1,2] (c) migration direction locked into [1,1]. (d) average migration angle as a function of the forcing direction for microspheres in nematic 5CB and in water. Force angle is defined as the angle between force and the [0,1] direction. Migration angle is defined between the average direction of motion and the [0,1] direction. The dashed line represents equality between the migration angle and forcing angle.

where k_B is the Boltzman constant, and T is temperature. Based on the values above, $Pe \sim 2.4 \times 10^4$, indicating that diffusion is negligible and this particle motion is essentially deterministic.

For comparison, we performed the same set of measurements on silica spheres of the same size translating through an isotropic liquid (15 mM KOH aqueous solution). The results for the propagation directions are also shown in Fig. 4.7(d). In the isotropic liquid, the spheres assume the same three locking directions as in nematic 5CB; however, the transition angles from [0,1] to [1,2] and from [1,2] to [1,1] are different. Specifically, they are 23° and 30°, respectively, in the isotropic fluid. We can compare these numbers with theoretical calculations by Risbud and Drazer [112], who considered colloid propagation in a lattice of obstacles in which hydrodynamic interactions (which are time reversible) and short-range non-hydrodynamic interactions (which are not reversible) act between the particles and posts. Their calculations predict for the geometry in our experiment ($60\ \mu m$ lattice period, $35\ \mu m$ post diameter and $15\ \mu m$ diameter spheres) transitions from [0,1] to [1,2] propagation at about $\alpha = 22.6°$, and from [1,2] to [1,1] at about $\alpha = 30.3°$, which are very close to our measured results. The smaller transition angles in 5CB than in water can be attributed to the effects of the larger-range particle-post interaction in the liquid-crystal environment. In particular, the attractive elastic interaction quantified in Fig. 4.4(b) can be considered loosely like expanding the effective particle size, which the calculations of Risbud and Drazer indicate should lead to the transitions between locking directions at smaller angle, as seen in Fig. 4.7(d).

4.4 Conclusion

In conclusion, the experiments to investigate the mobility of colloidal particles in nematics through obstacles arrays have illustrated the form of particle-post interactions mediated by liquid crystals and the influence of these interaction on the directional locking behavior. Although a repulsive interaction is behavior of particles near isolated posts, geometric confinement leads to an attractive interaction instead when particles translate through the obstacle arrays. In particular, the spatially modulated mobility observed in the experiment has provided insight on the form of the particle-post interaction and the varying effective viscosity through the array. The unconventional attractive particle-post interaction also reshapes the response of the particles' migration behavior to the applied force, resulting in smaller transition angles compared with that in isotropic liquids. Experiments which explore new mechanisms of particles separation with the particle-post interactions seen in this study could test their potential for application.

Chapter 5

Rheo-XPCS study of yielding in Concentrated Colloidal Gels

5.1 Introduction

Any solid subjected to applied stress possesses an elastic limit above which it fails, either by fracturing or yielding. Signatures of yield at the nanoscale to microscale are irreversible changes to the material's structure. In amorphous solids, such as glasses, pastes, and gels, the intrinsic disorder makes identifying these microstructural changes difficult. Despite recent progress, particularly on yielding of glasses [119-122], understanding the microstructural dynamics associated with the transition from elastic response at low strain to nonlinear deformation and flow at high strain in disordered solids remains incomplete. Formulating such connections between microscopic properties and macroscopic mechanical response is a central challenge for soft-matter physics. In this chapter, I present an experimental approach that exploits the capabilities of coherent x-ray scattering with *in situ* shear to reveal details about the nanometer-scale structural dynamics of soft disordered solids underlying their bulk mechanical response. This work was conducted in collaboration with Prof. James Harden and Dr. Michael Rogers of the University of Ottawa.

Conventional small-angle x-ray and neutron scattering under *in situ* shear has

provided information about the average structural modifications of soft materials due to stress and flow [123-134]. However, a full understanding of the interdependence of microscopic properties and macroscopic rheology requires *in situ* information about the structural dynamics driven by stress. A promising technique for probing such dynamics is x-ray photon correlation spectroscopy (XPCS), introduced in Chapter 2, wherein fluctuations in coherent scattering intensity, or speckle patterns, directly monitor dynamical evolution in the microstructure. For a solidlike amorphous sample subject to an oscillatory shear strain in an XPCS measurement, the motion of constituent particles due to the strain will cause a decay in the intensity autocorrelation function $g_2(\boldsymbol{q}, t)$, due to the shear term described in Chapter 2. However, if the deformation is elastic and reversible, the scattering particles will return to their original position after a complete strain cycle, causing the speckle pattern to recover its original configuration. These "echoes" in the speckle pattern will cause $g_2(\boldsymbol{q}, t)$ to return to $g_2(\boldsymbol{q}, t)$, and the correlation function will peak at integer multiples of the oscillation period, as depicted in Fig. 5.1(a). However, if shearing induces irreversible rearrangements so that some particles fail to return to their original positions, the echo peak will be attenuated, like in Fig. 5.1(b), providing a measure of the microscopic irreversibility.

A similar approach to measure echoes with diffusing wave spectroscopy (DWS, dynamic light scattering in the highly multiply scattering limit) has been used to investigate shear-driven structural dynamics in foams, colloidal glasses, and other soft materials [135-140]. Recently, Laurati *et al.* reported a DWS study on concentrated colloidal gels under in *situ* oscillatory shear that showed evidence for plastic rearrangements correlated with the initial yielding of the gels [140]. Due to the multiple

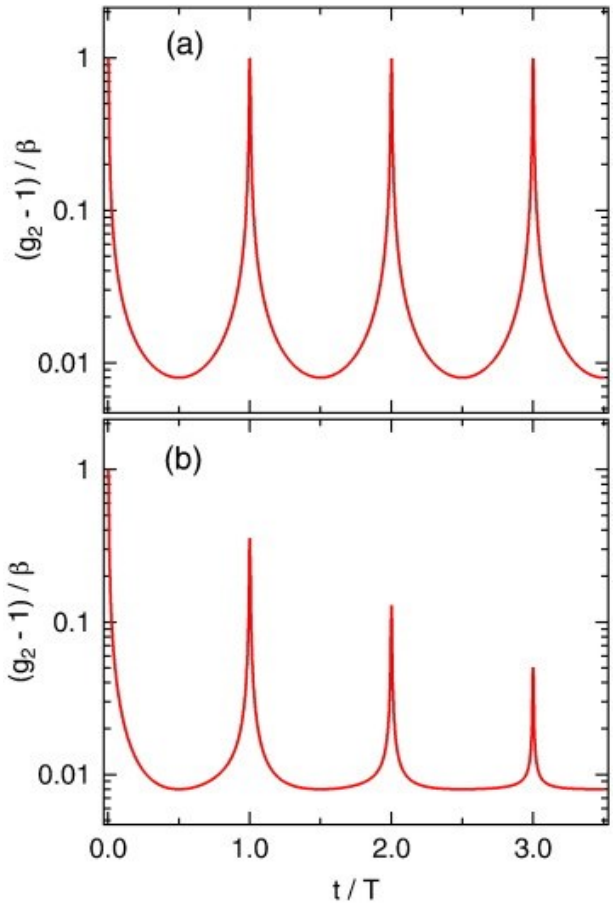

Figure 5.1: (a) Calculated XPCS intensity autocorrelation function from a material undergoing affine deformation due to an in situ oscillatory shear strain with period T. The lineshape is based on Eq. (5.6) with $q_{\|} = 0.025$ nm^{-1}, $\gamma_0 = 0.01$, and $H = 500$ μm. (b) Schematic of the correlation function depicting the attenuation of the echo peaks resulting from strain-induced irreversible microscopic rearrangements.

scattering in DWS, the technique is sensitive to motions over essentially a single length scale, which in Ref. [140] was approximately the particle radius. In this chapter, I describe XPCS experiments measuring shear echoes to track the irreversible rearrangements underlying the nonlinear rheology of a model concentrated nanocolloidal gel. Beyond providing nanometer-scale resolution of yielding behavior in the gel, the wave-vector dependence of $g_2(\boldsymbol{q},t)$ gives information about the shear-induced rearrangements over a range of length scales, thereby providing insight into the spatial-size distribution of the irreversible rearrangements.

5.2 Experiment Methods

5.2.1 Gel Characterization

The gel, provided by Prof. S. Ramakrishnan from Florida State University, was comprised of octadecyl-grafted silica nanocolloids with radius R $\simeq$ 16 nm and colloid volume fraction $\phi = 0.3$. This volume fraction placed the gel in the moderately concentrated regime, above the dilute regime ($\phi \leq 0.1$) where gel structures have fractal character but below the crossover to the attractive glass regime, which is thought to be around $\phi \sim 0.4$ [141]. The colloids were in the solvent decalin with added polystyrene with radius of gyration $R_g \simeq 3.5\,nm$ and concentration $c_P/c_P^* = 0.20$, where c_P^* is the overlap concentration. The nanoparticles experience an entropic depletion attraction due to the presence of the nonabsorbing polymer that causes them to form a gel at this ϕ and c_P/c_P^*. Specifically, for these values of R_g/R and ϕ, the gel transition occurs at a polymer concentration $c_P/c_P^* \simeq 0.09$ [142], so the gels in the experiment were far from the fluid-gel boundary.

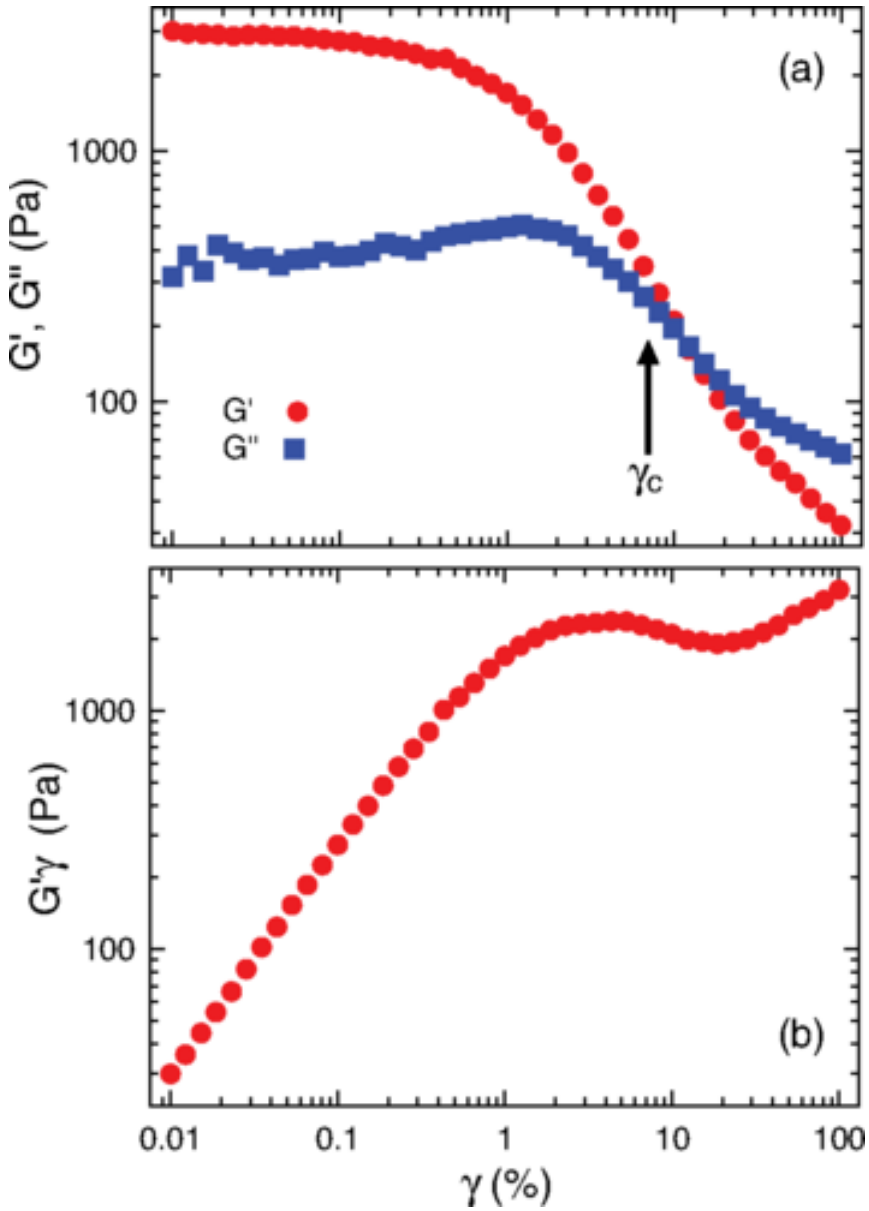

Figure 5.2: (a) Storage (red circles) and loss (blue squares) moduli and (b) elastic stress at $\nu = 0.318$ Hz as a function of strain amplitude. The arrow in (a) indicates the threshold strain above which the XPCS shear echo amplitude displays pronounced attenuation.

The phase behavior, structure, and bulk mechanical properties of such nanocolloidal depletion gels are well characterized [142-144]. Furthermore, these gels were employed in a previous XPCS study to track microscopic dynamics of recovery following a pre-imposed fluidizing shear [145]. The shear modulus, $G^*(v) = G'(v) + iG''(v)$ of the gel, shown in Fig. 5.2(a) as a function of strain amplitude γ at frequency $\nu = 0.318$ Hz, possesses nonlinear characteristics typical of soft disordered solids. At low γ, G' and G'' are roughly constant with $G' \gg G''$, indicating a solid-like elastic response. At larger γ, G' decreases rapidly and eventually crosses G'' indicating viscoplastic flow.

Fig. 5.2(b) shows the strain dependence of the product $G'\gamma$, known as the elastic stress, which is a representation of the strain-dependent rheology that facilitates identification of points of yielding [146]. Above a linear regime at low strain, where the $G'\gamma$ is proportional to γ, the stress-strain relation becomes sublinear, and $G'\gamma$ reaches a local maximum near $\gamma = 5\%$. Such maxima are common in the rheology of disordered soft solids, including in depletion gels similar the one in the current study [146], and their position is often used to locate the yield point. In fact, the nonlinear rheologies of attractive colloidal glasses and concentrated colloidal gels has been shown to display two such features as a function of strain, which are identified as two separate yielding processes in these materials [146-148]. For concentrated colloidal gels like in the present study, the second yield point is seen only above $\gamma = 100\%$, and hence outside the range shown in Fig. 5.2. As described below, the irreversible rearrangements that affect the XPCS shear echoes become apparent at strains near the first yield point at $\gamma \approx 5\%$, which is associated with initial bond-breaking events [146,147]. Hence, we focus on the

behavior at these smaller strains. Presumably, a second yielding process like that seen previously, which has been associated with cage breakup in the case of denser colloidal systems and cluster breakup in less dense systems [146,147], would be apparent in measurements on the gel that extended to $\gamma > 100\%$.

5.2.2 XPCS within *Situ* LAOS

To investigate the nanoscale structural rearrangements corresponding to the nonlinear rheology, we conducted small angle XPCS experiments under in *situ* oscillatory shear. Measurements were performed at beamline 8-ID-I of the Advanced Photon Source using 7.34-keV x-rays using a custom shear cell built by Prof. Harden. The gel was contained between parallel diamond windows with 500 μm spacing. A thin sheet of polyamide was attached to each window and was roughened to prevent wall slip. One window was held static and the other was attached to a stage that was translated by a voice coil linear actuator. An optical encoder with 50 nm precision, zero reference, and 32-kHz refresh rate was attached to the translating stage to enable precise application of arbitrary, time-dependent shear strains through computer control of the actuator. A 20×20 μm^2 partially coherent beam was incident on the sample normal to the windows, and measurements of the coherent scattering were made in transmission. In this configuration the incident beam was parallel to the shear-gradient direction, so that in the small-angle-scattering limit of the measurements the scattering wave vectors lay in the flow-vorticity plane. A direct-illuminated CCD area detector (Princeton Instruments, 1300×1340 pixels) located 4.07 m after the sample measured the scattering intensity over wave-vector magnitudes $0.03\ \text{nm}^{-1} < q < 0.22\ \text{nm}^{-1}$ in both the flow and vorticity

directions. For analysis, the detector pixels were partitioned according to **q** magnitude and direction with $\sim 10^3 - 10^4$ pixels (where the speckle size was approximately equal to 1 pixel) in each partition to ensure proper ensemble averaging. Fig. 5.3 shows an example of a CCD image of the scattering intensity from the gel with two such partitions highlighted.

A schematic representation of the oscillatory strain profile applied during the measurements is shown in Fig. 5.4. The strain followed a sinusoidal time dependence between extrema in its value. At each extremum the strain was held constant for a short period during which a scattering image was obtained. Periodically holding the strain fixed in this way eliminated smearing of the speckle pattern due to shearing during the x-ray exposures. In most cases, a measurement at a given strain amplitude and oscillation frequency included 256 images (128 oscillation periods) from which $g_2(\boldsymbol{q}, t)$ was determined. Prior to each measurement, several periods of oscillation were applied to avoid any transient effects. By analyzing the first half of the images and the second half separately [i.e., by calculating $g_2(\boldsymbol{q}, t)$ from the first 128 frames and from the second 128 frames separately], we confirmed that no systematic changes in the correlation function occurred during the measurement, indicating that the measurements probed the steady-state behavior under oscillatory shear. In addition, measurements of $g_2(\boldsymbol{q}, t)$ under quiescent conditions were performed before and after the measurements under shear, and no systematic effects from intervening shearing, such as shear-induced rejuvenation, were observed for any of the shear profiles applied in the experiment (strain amplitudes $\gamma \leq 30\%$). This robustness is consistent with previous studies of these depletion gels that showed the rheology and microstructure recovered essentially immediately after

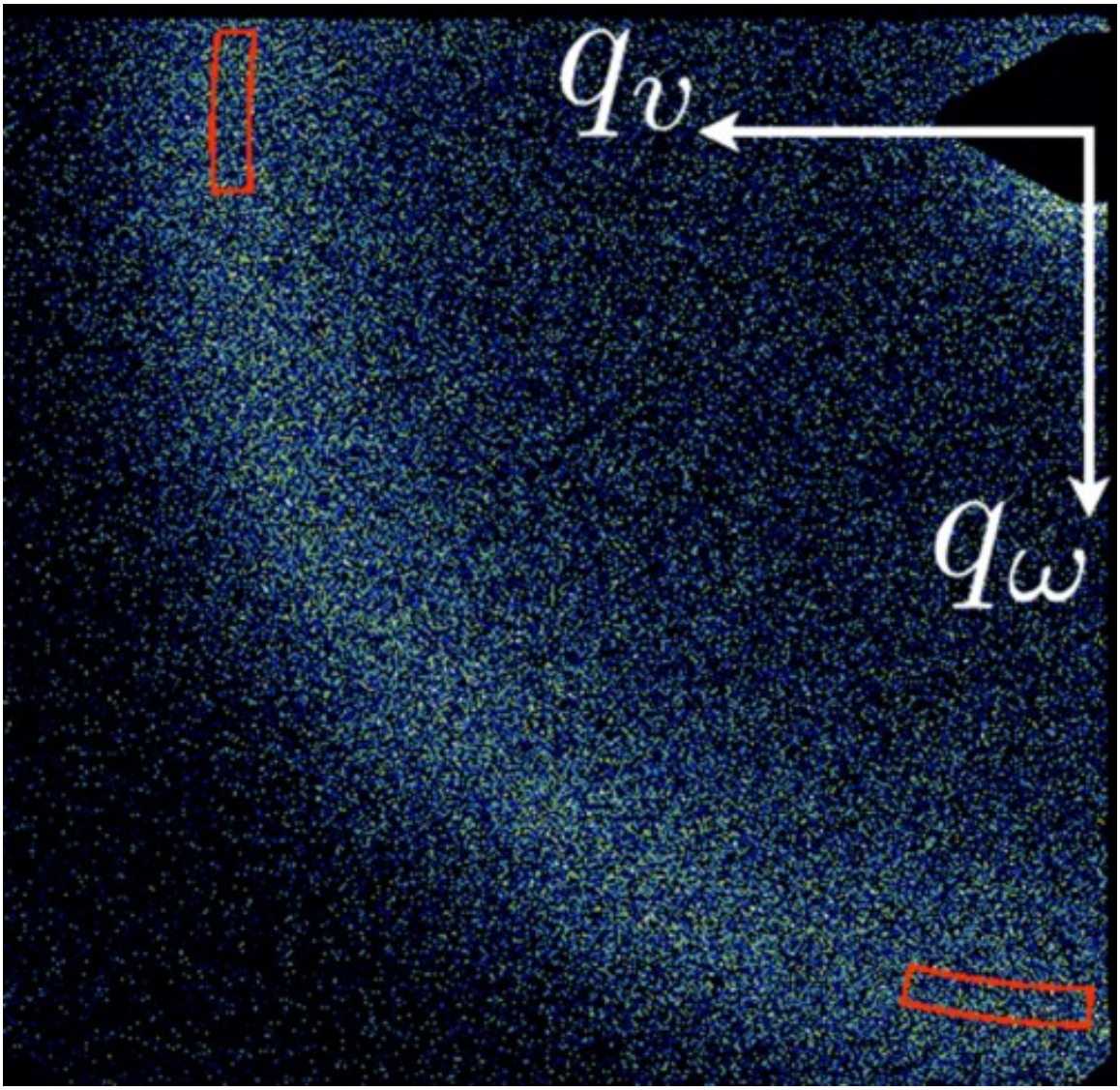

Figure 5.3: A CCD image of the x-ray scattering intensity. The incident beam position, corresponding to $q = 0$, is obscured by the shadow of the beamstop in the upper right. The wave-vector directions parallel to the flow direction qv and parallel to the vorticity direction $q\omega$ are indicated by arrows. Two examples of partitions delineating the pixels included in the analysis of $g_2(\boldsymbol{q}, t)$ at fixed wave-vector magnitude and direction are shown by the red boxes. These two partitions are located at $q = 0.19\ nm^{-1}$.

cessation of applied shear [149]. We also repeated several measurements during the course of the experiment. The repeated measurements showed good agreement, indicating no shear-driven sample evolution.

We note that the brief interruptions at the strain extrema for obtaining the x-ray images potentially complicate comparisons of the echo results with rheology and (incoherent) scattering studies that employ LAOS to investigate the nonlinear response of colloidal gels [140, 146]. However, we believe these complications are minor and valid comparisons can be made. Studies have shown that concentrated gels formed from colloids with short-range attraction obey the so-called Delaware-Rutgers rule [131], which states that for yielding concentrated suspensions with large structural relaxation times, the response during oscillatory deformation is dictated by the maximum shear rate (the product of frequency and strain amplitude) rather than the frequency of deformation [150]. Hence, for comparisons with LAOS measurements, one should consider the magnitude and the period of the sinusoidal part of the strain (neglecting the interruption) in the XPCS measurements.

5.3 Results

Fig. 5.5 displays examples of the intermediate scattering function $g_2(\boldsymbol{q}, t)$ during application of strain profiles with amplitudes $\gamma = 4\%$ and 12% at $q = 0.18\, nm^{-1}$, a wave vector near the interparticle structure factor peak in the scattering intensity, in a direction parallel to the vorticity direction. The strain rate between extrema corresponded to a sine wave with frequency 0.318 Hz and the hold time at each extremum was 0.5 s, during which a 0.25-s x-ray exposure was obtained, leading to a repeat time for the strain

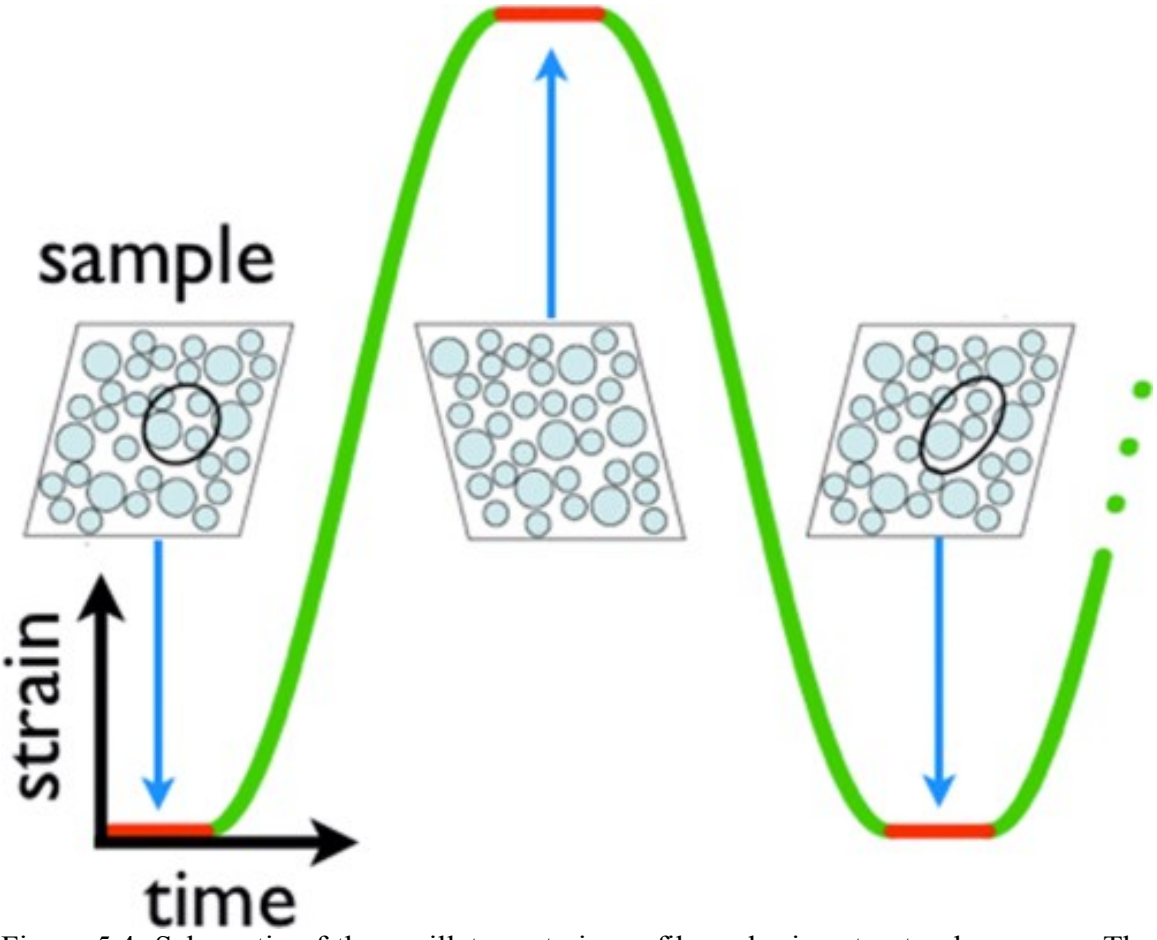

Figure 5.4: Schematic of the oscillatory strain profile and microstructural response. The strain followed a sinusoidal form (green) between extrema. At each extremum the strain was held constant for a short time (red) during which a coherent x-ray exposure was obtained. The cartoons of the amorphous solid illustrate the change in strain each half period and the recovery of the microstructure each full period. The circled particles highlight a region that undergoes irreversible rearrangement during the cycle.

of T = 4.14 s. For comparison, $g_2(\boldsymbol{q}, t)$ measured in the absence of shear is also shown. In this quiescent state, $g_2(\boldsymbol{q}, t)$ has a shape common to many disordered soft solids in which it maintains a large value at short delay times t, indicating a nominally static configuration, but decays at long delay times (t $\gtrsim$ 100 s) with a compressed-exponential form that can be associated with slow relaxation of heterogeneous residual stress [52, 151-154]. For the measurements under in *situ* shear, $g_2(\boldsymbol{q}, t)$ displays periodic peaks corresponding to echoes in the speckle pattern. As illustrated schematically in Fig. 5.4, the change in strain between extrema leads to gradients in the particle displacements that alter the speckle pattern completely [56, 155] even for modest values of strain. Thus, $g_2(q, t) \approx 1$ at $t = \left(n + \frac{1}{2}\right) T$, where n is an integer. However, at delay times separated by an integer number of repeat times $t = nT$, the strain returns and the speckle pattern is recovered, causing $g_2(\boldsymbol{q}, t)$ to increase above one. At $\gamma = 4\%$, $g_2(\boldsymbol{q}, t = nT)$ traces $g_2(\boldsymbol{q}, t)$ measured under quiescent conditions, indicating that the particles undergo no shear-induced irreversible rearrangements. At $\gamma = 12\%$, $g_2(\boldsymbol{q}, t = nT)$ decays rapidly, revealing significant irreversible rearrangement in the gel.

Fig. 5.6 displays $g_2(\boldsymbol{q}, t = nT)$ at $q = 0.18\, nm^{-1}$ along the vorticity direction at several γ as a function of the number of delay cycles n. [We emphasize that $g_2(\boldsymbol{q}, n)$ is a measure of the speckle correlations in images separated by n periods of oscillation in steady state.] The attenuation of the echo peaks increases sharply between $\gamma = 6\%$ and 8%, indicating a transition to irreversible, nanoplastic deformation above a threshold strain $\gamma_c \approx 7\%$. The arrow in Fig. 5.2 indicates the approximate value of γ_c. We note that this critical strain for the onset of microscopic irreversibility is close to yield point identified in the macroscopic rheology. However, we also note that that the storage

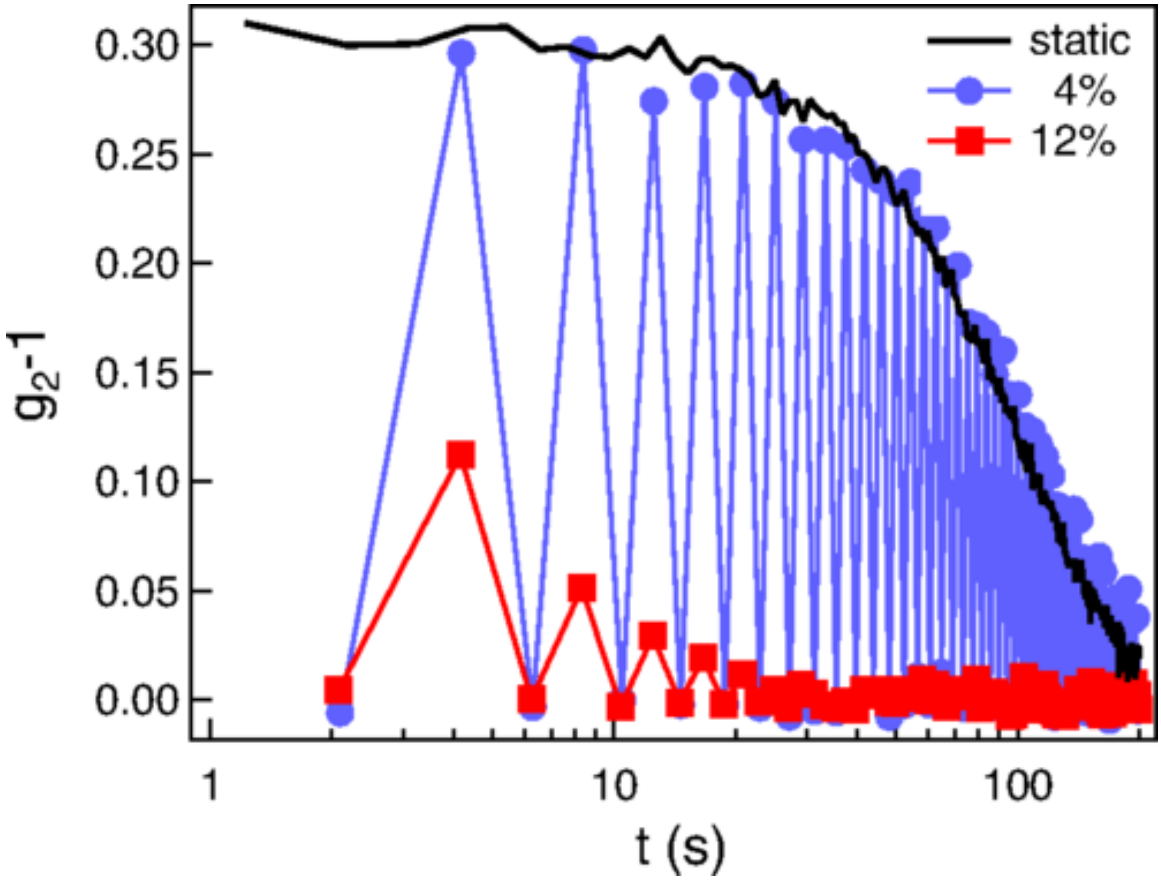

Figure 5.5: Echoes in the intensity autocorrelation function during application of oscillatory strain with amplitudes γ = 4%(blue circles) and 12% (red squares) measured in the vorticity direction at q = 0.18 nm−1. The applied strain between extrema followed a sine wave with frequency 0.318 Hz and the hold time at each extremum was 0.5 s, leading to a repeat time of 4.14 s. The blue and red lines are guides to the eye. The echoes at γ = 4% track the intensity autocorrelation of the quiescent gel (black line), indicating that shear plays no role in decorrelation at this strain amplitude.

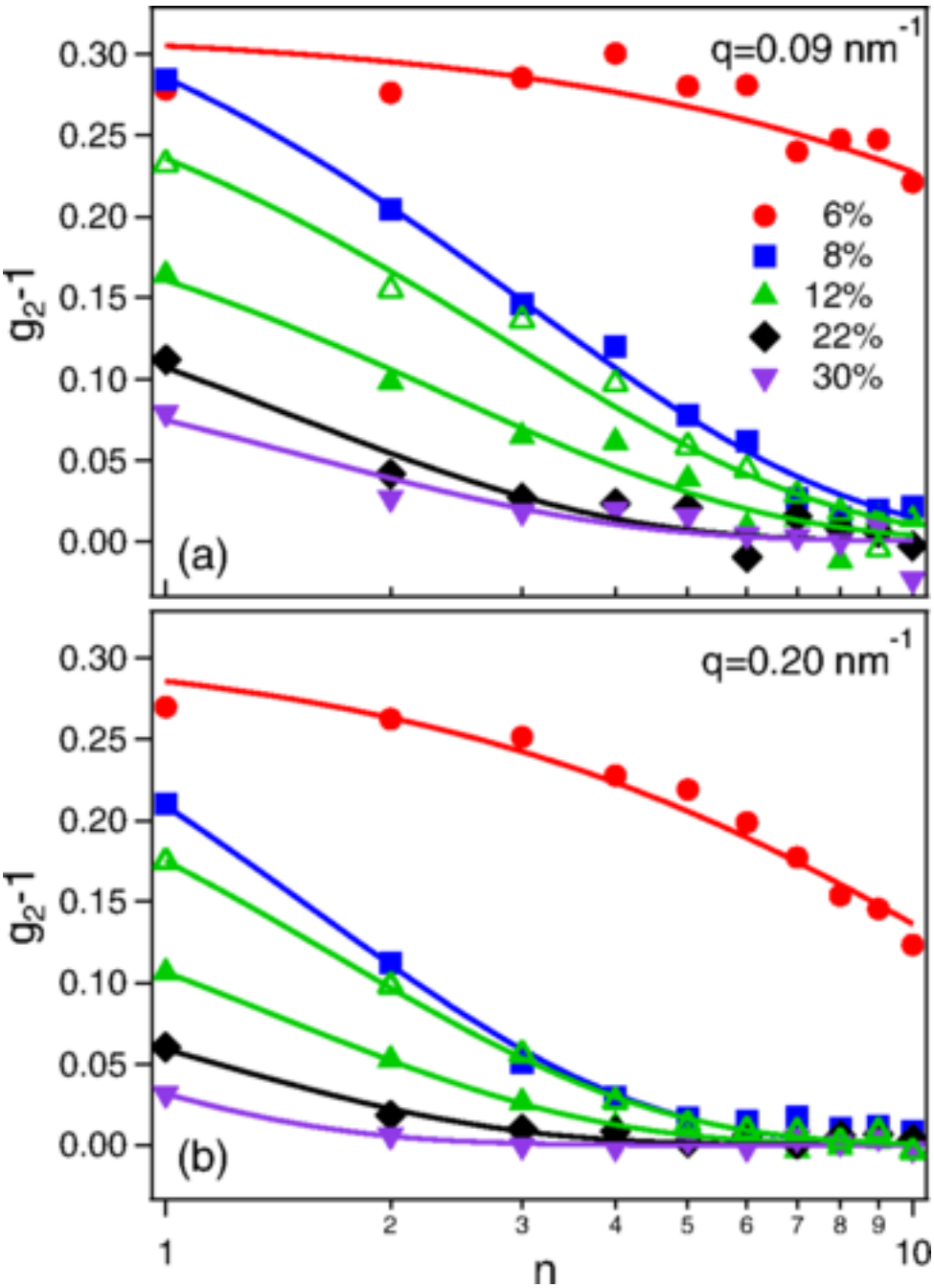

Figure 5.6: Echo-peak amplitudes at wave vectors along the vorticity direction at (a) $q = 0.09\ nm^{-1}$ and (b) $q = 0.20\ nm^{-1}$ as a function of delay cycle for strains γ = 6% (red circles), 8% (blue squares), 12% (green triangles), 22% (black diamonds), and 30% (purple inverted triangles). Also shown are the amplitudes at γ = 12% along the flow direction (open green triangles). Solid lines are the results from fitting an exponential decay to the echo-peak amplitude.

modulus $G'(v)$ displays significant strain softening and the loss modulus goes through a peak at considerably lower γ, revealing that there is a range of strains that cause nonlinear but fully reversible deformations. Studies of glasses and granular materials have observed that reversible plastic events are prevalent at strains below those causing irreversible events and in some cases these events can be linked to the onset of a nonlinear stress response [156, 157]. Our results on the nanocolloidal gel, an attractive system, indicate that this behavior is general to both repulsive and attractive systems. Also shown in Fig. 5.6 are the echo-peak amplitudes at one strain above the threshold ($\gamma = 12\%$) for q parallel to the flow direction. Surprisingly, the attenuation is anisotropic, with the echoes decaying more rapidly as a function of n for $\boldsymbol{q}$ along the vorticity direction than along the flow direction; however, the results along both directions indicate $\gamma_c \approx 7\%$ for the onset of irreversibility.

The solid lines in Fig. 5.6 are results from fitting exponential decays to the peak amplitudes:

$$g_2(\boldsymbol{q}, n) = 1 + \beta \exp(-\Gamma n) \tag{5.1}$$

where $\beta \simeq 0.30$ is the Siegert factor determined from separate measurements on a static sample (aerogel). We find that an exponential decay accurately describes the peak amplitudes at all γ and q, in both the flow and vorticity directions, for which the decay is sufficiently rapid to dominate the intrinsic, quiescent decay in $g_2(\boldsymbol{q}, t)$. Fig. 5.7 shows the decay rate Γ as a function of wave-vector amplitude at $\gamma = 8\%$ for $\boldsymbol{q}$ parallel to the flow and vorticity directions. Consistent with the results in Fig. 5.6, the rate is larger along the vorticity direction than along the flow direction. However, the static scattering intensity $\mathrm{I}(q)$, shown in Fig. 5.8 for q along the two directions, is fully isotropic,

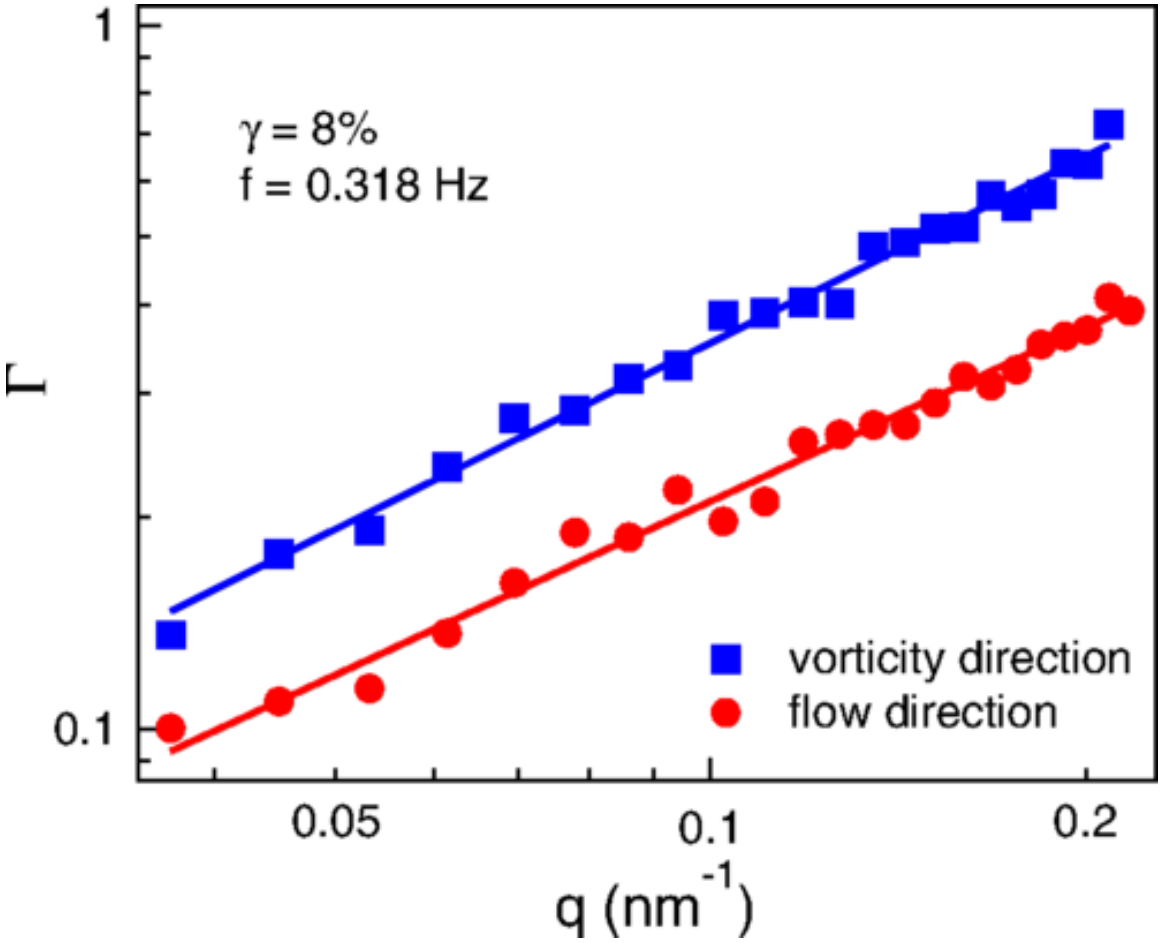

Figure 5.7: Echo-decay rate Γ (in 1/cycle) at γ = 8% as a function of wave-vector amplitude for wave vectors in the flow direction (red circles) and the vorticity direction (blue squares). Solid lines indicate the result of power-law fits, which give exponents $\alpha = 0.82 \pm 0.03$ (red) and $\alpha = 0.88 \pm 0.03$ (blue).

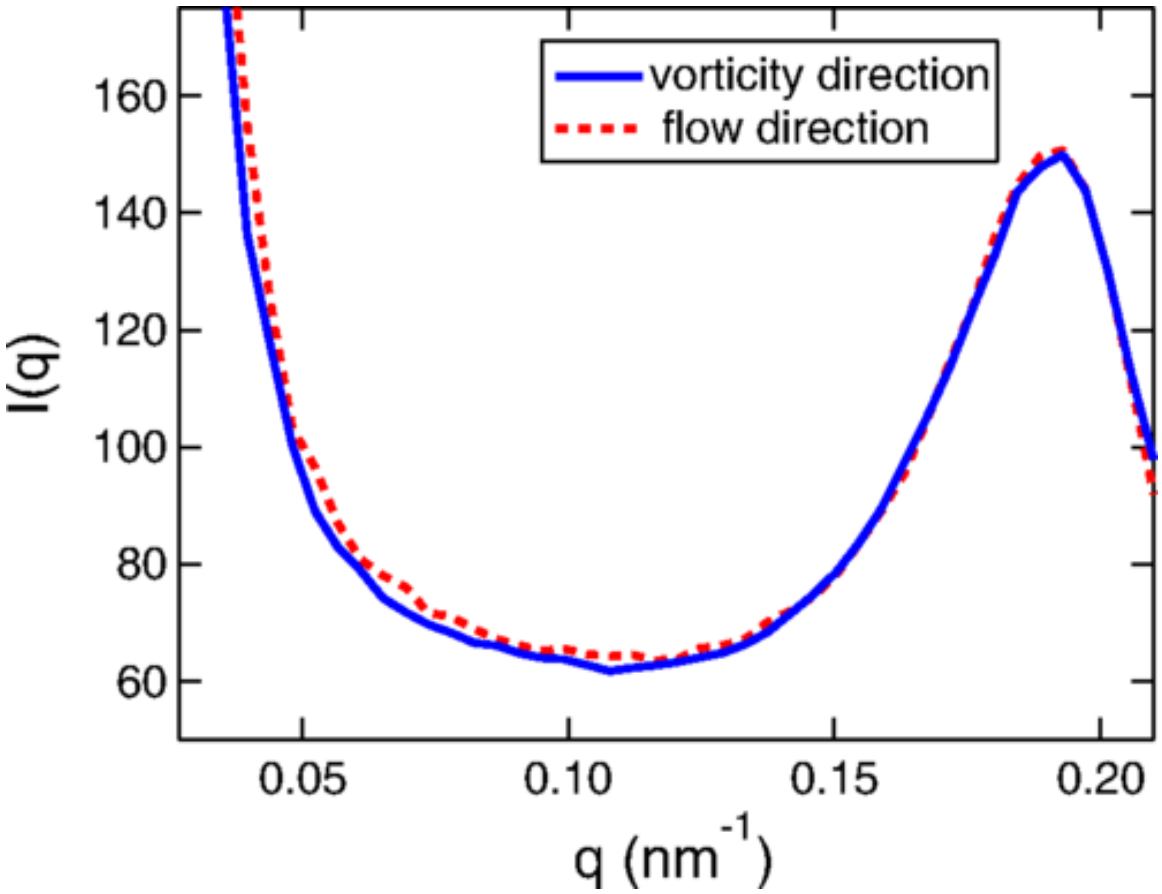

Figure 5.8: Static x-ray scattering intensity as a function of q along the flow (red dashed line) and vorticity (blue solid line) directions at $\gamma = 8\%$.

indicating no corresponding signatures of shear-induced anisotropy in the structure. In both q directions, the decay rate scales as a weak power law with wave vector, $\Gamma(q) \sim q^{\alpha}$ with $\alpha = 0.82 \pm 0.03$ in the flow direction and $\alpha = 0.88 \pm 0.03$ in the vorticity direction, as shown by the power-law fits in Fig. 5.7. Such power-law behavior is seen at all γ for which Γ could be accurately determined. Although the value of α varied somewhat between measurements, perhaps due to sample heterogeneity, it showed no clear systematic dependence on strain profile. The average value was $\alpha = 0.7 \pm 0.2$.

5.4 Discussion

5.4.1 Length Scale of Structural Response to Shear

As Fig. 5.8 demonstrates, the imposed oscillatory shear creates no noticeable anisotropy in the gel structure over the range of wave vectors probed with small-angle x-ray scattering. A prominent structural signature seen in dilute gels in the fractal regime ($\phi < 0.1$) is the formation of large-scale, shear-induced anisotropies that manifest distinct scattering profiles known as butterfly patterns at lower $\boldsymbol{q}$ in static light scattering [133,134]. (These patterns can also be observed for gels with larger concentration in the higher-$\boldsymbol{q}$ range of small-angle x-ray and neutron scattering, but only at considerably larger strain amplitudes than those probed here [131].) While we cannot completely rule out such a large-length-scale structural response in the concentrated gel under study, we believe it is unlikely. As Masschaele *et al.* have shown in a study on yielding in two-dimensional gels [158], the characteristic scale of structural deformations becomes increasingly localized as gel concentration increases, and the typical spatial scale is only a few particle diameters in the concentrated regime. Further, effective theories based on

mode-coupling ideas have successfully predicted many features of yielding in concentrated colloidal gels [159, 160]. These theories consider only local structural properties, specifically those contained in the static structure factor $S(\boldsymbol{q})$, and issues such as large-scale heterogeneity, the connectivity of the gel structure, and bond percolation are not taken into account. Hence their success suggests that these nonlocal properties ultimately have only a weak effect on the structural dynamics associated with yielding in concentrated gels. Finally, the motion associated with the rigid rotation of large-scale clusters like that pictured to create the anisotropic low-$\boldsymbol{q}$ scattering profiles at lower concentration would cause immediate complete decorrelation of $g_2(\boldsymbol{q}, n)$ in the range of q accessed with XPCS, in stark contrast to what we observe. Thus, from the structural and dynamical information provided in this XPCS study, we can infer that the shear-induced structural response of the concentrated gel near the first yield point involves primarily small-scale structural rearrangements.

5.4.2. Model for The Shear-induced Structural Dynamics

The observed exponential decay in $g_2(\boldsymbol{q}, n)$ provides insight into the nature of the irreversible rearrangements underlying the nonlinear mechanical behavior of the gel. In particular, the fact that $g_2(\boldsymbol{q}, n)$ decays fully to one with no sign of persistent correlations implies that shear causes essentially the entire sample within the scattering volume eventually to undergo irreversible rearrangement. That is, when viewed over multiple shear cycles, the irreversible rearrangements are not isolated to a portion of the sample as one might expect, for example, with shear banding.

One possible interpretation for such non-localized dynamics would invoke a

stress-induced effective diffusivity of the colloidal particles [161, 162]. While such motion would lead to an exponential decay in $g_2(\boldsymbol{q}, n)$, the decay rate would vary with wave vector as $\Gamma \sim q^2$, perhaps modulated by the structure factor $S(\boldsymbol{q})$ in analogy with de Gennes narrowing. In contrast, the much weaker power-law dependence of Γ on q in Fig. 5.7, with no influence of features in $S(q)$ like the large interparticle structure-factor peak near $q = 0.19\, nm^{-1}$, is incompatible with a picture of effective diffusion. Instead, we can understand the exponential decay in $g_2(\boldsymbol{q}, n)$ through a model of heterogeneous dynamics in which regions of the sample comprising a volume fraction f undergo irreversible rearrangements during a shear cycle. The coherent scattering from these regions becomes randomized, while that from the remainder of the sample remains unchanged. In this case, the intermediate scattering function $g_1(\boldsymbol{q}, t)$, which as mentioned above is related to $g_2(\boldsymbol{q}, t)$though the Siegert relation $g_2(q, t) = 1 + \beta\, {g_1}^2(\boldsymbol{q}, t)$, is a mixture of contributions from scattering from these dynamic and static components, much like in a heterodyne measurement [163]. Following such a heterodyne analysis, the dynamics during a cycle leads g_1 to a decrease such that $g_1(\boldsymbol{q}, n = 1) = (1 - f) g_1(\boldsymbol{q}, 0)$ [164]. Further, if the regions that rearrange in a given cycle are located randomly in the sample, independent of the locations of previous events, then the fraction of sample that remains unaltered over n cycles is $(1 - f)^n$. Thus, for such rearrangements with no history, $g_1(\boldsymbol{q}, n) = (1 - f)^n g_1(\boldsymbol{q}, 0)$ or, since $g_1(q, 0) = 1$,

$$g_1(\boldsymbol{q}, n) = (1 - f)^n \tag{5.2}$$

which leads directly to an exponential form for $g_2(\boldsymbol{q}, n)$ like in Eq (5.1) with $\Gamma = 2f$.

Thus, within this model the q dependence of Γ is that of $2f$. To interpret this dependence, we note any irreversible event that decorrelates g_2 at a wave vector q must

cause the particles to rearrange their positions on a length scale $l \gtrsim q^{-1}$. Hence, if an event contributes to attenuating g_2 at some q, it does so for all larger q as well. Therefore, since $f \sim \Gamma \sim q^{\alpha}$, the fraction of the sample involved in events during each shear cycle that rearrange the positions of particles over a length scale l greater than some given length l_0 varies as $f(l > l_0) \sim {l_0}^{-\alpha}$. The fraction in which the scatterers are rearranged on a length scale l thus scales as

$$f(l) \sim l^{-\alpha+1} \tag{5.3}$$

This model leads to an interpretation of the anisotropy in Γ in Fig. 5.7: The different decay rates imply that the motion within rearranging regions is on average anisotropic (larger along the vorticity direction than the flow direction), but this anisotropy is self-similar and the power-law size distributions in the two directions differ by only a scale factor.

Further, assuming that the linear size of a region L undergoing rearrangement scales with l, then the fraction of the sample involved in events of size L similarly varies as $f(L) \sim L^{-(\alpha+1)}$. Since each event of linear size L occupies a volume V that scales as L^3, the number of events hence scales with their linear size as $N(L) \sim L^{-(\alpha+4)}$. Thus, the number of events varies with their volume as

$$N(V) \sim V^{-\frac{\alpha+4}{3}} \tag{5.4}$$

or, taking $\alpha = 0.7 \pm 0.2$, $N(V) \sim V^{-\xi}$ with $\xi = 1.56 \pm 0.06$. Such a power-law distribution of event sizes indicates a nonequilibrium critical transition in the gel at yielding. Many physical phenomena involving disorder, from earthquakes to Barkhausen noise to fluid-interface depinning, exhibit power-law statistics in their response to a driving force, and ideas of nonequilibrium critical phenomena provide a unifying

perspective for this behavior. Indeed, power-law distributions have been observed in the nonlinear mechanical response in numerical simulations of glasses [164, 165] and in experiments on disordered crystals [166-168] and metallic glasses [169, 170], where the measured quantities were fluctuations in energy or stress σ that scaled as $N(\sigma) \sim \sigma^{-\tau}$ with τ in the range 1.5–1.6. The remarkably similar values of τ and the exponent ξ we obtain suggest that the spatial size of plastic events scales with the energy dissipated by them, $\xi = \tau$.

5.4.3 Echo Lineshapes

Additional information can be obtained from studies combining XPCS with LAOS that not only compare speckle patterns obtained stroboscopically each oscillation, as in the experiment described in the previous section, but that also characterize the full lineshape of $g_2(\boldsymbol{q}, t)$ at a temporal resolution that is large compared to the oscillation frequency. In particular, such lineshapes, when they deviate from the shape corresponding to an affine deformation, could give insight into nonaffine response to the shear. The expected shape of $g_2(\boldsymbol{q}, t)$ during LAOS on a material that does undergo affine and reversible deformation can be found by generalizing the results discussed in Chapter 2 (specifically, Eq (2.14) and Eq (2.15)) to the case of a sinusoidal strain, $\gamma(t) = \gamma_0 \cos(\omega t + \varphi)$,

$$\left|g_{1,S}(q,t,\varphi)\right|^2 = \frac{1}{H^2}\int_0^H \int_0^H cos\left[q_{\parallel}\gamma_0\big(\cos(\varphi) - \cos(\omega t + \varphi)\big)(y_2 - y_1)\right]\mathrm{d}y_1\mathrm{d}y_2$$

$$= \frac{\sin^2\left(q_{\parallel}\gamma_0 H\big(\cos(\varphi) - \cos(\omega t + \varphi)\big)\right)}{\left(\frac{q_{\parallel}\gamma_0 H\big(\cos(\varphi) - \cos(\omega t + \varphi)\big)}{2}\right)^2}$$

$$= \left[\frac{\sin\left[q_{\parallel}\gamma_0 H sin\left(\frac{\omega t}{2}\right) \sin\left(\frac{\omega t}{2}+\varphi\right)\right]}{q_{\parallel}\gamma_0 H sin\left(\frac{\omega t}{2}\right) \sin\left(\frac{\omega t}{2}+\varphi\right)} \right]^2 \tag{5.5}$$

In practice, an XPCS measurement under steady-state LAOS will span multiple cycles of the shear, so that $g_2(\boldsymbol{q},t)$ will be determined from an average over pairs of scattering images in which the first image is obtained at different points in the oscillation. Thus, $g_2(\boldsymbol{q},t)$ will be an average over the phase φ,

$$g_2(\boldsymbol{q},t) - 1 = \frac{\beta}{2\pi}\int_0^{2\pi} \left[\frac{\sin\left[q_{\parallel}\gamma_0 H sin\left(\frac{\omega t}{2}\right) \sin\left(\frac{\omega t}{2}+\varphi\right)\right]}{q_{\parallel}\gamma_0 H sin\left(\frac{\omega t}{2}\right) \sin\left(\frac{\omega t}{2}+\varphi\right)} \right]^2 \mathrm{d}\varphi$$

$$= \frac{\beta}{\Delta}\left(J_1(2\Delta)\cdot[\pi\Delta H_0(2\Delta) - 1] + \Delta J_0(2\Delta)\cdot[2 - \pi H_1(2\Delta)]\right.$$

(5.6)

where $\Delta = q_{\parallel}\gamma_0 H sin\left(\frac{\omega t}{2}\right)$, and $J_n(x)$ and $H_n(x)$ are the Bessel function of the first kind and the Struve function, respectively. Fig. 5.1(a) above displays an example of $g_2(\boldsymbol{q},t)$ calculated from Eq (5.6). As noted above, the extreme sharpness of the echo peaks, whose width is set by $(q_{\parallel}\gamma_0 H)^{-1}$, creates a challenge in measurements that seek to resolve the lineshape since a very high temporal resolution relative to the oscillation frequency is required.

As a test of the validity of Eq (5.6) in describing the XPCS intensity autocorrelation function from a material undergoing affine oscillatory deformation, Fig. 5.9 displays $g_2(\boldsymbol{q},t)$ from measurements on a dilute colloidal suspension in the highly viscous liquid polyglycerol subjected to an oscillatory shear at two strain amplitudes. The plots focus on the initial decay in $g_2(\boldsymbol{q},t)$ (rather than the echo peaks) to avoid complications from slow diffusion of the colloids that affects the correlations at larger

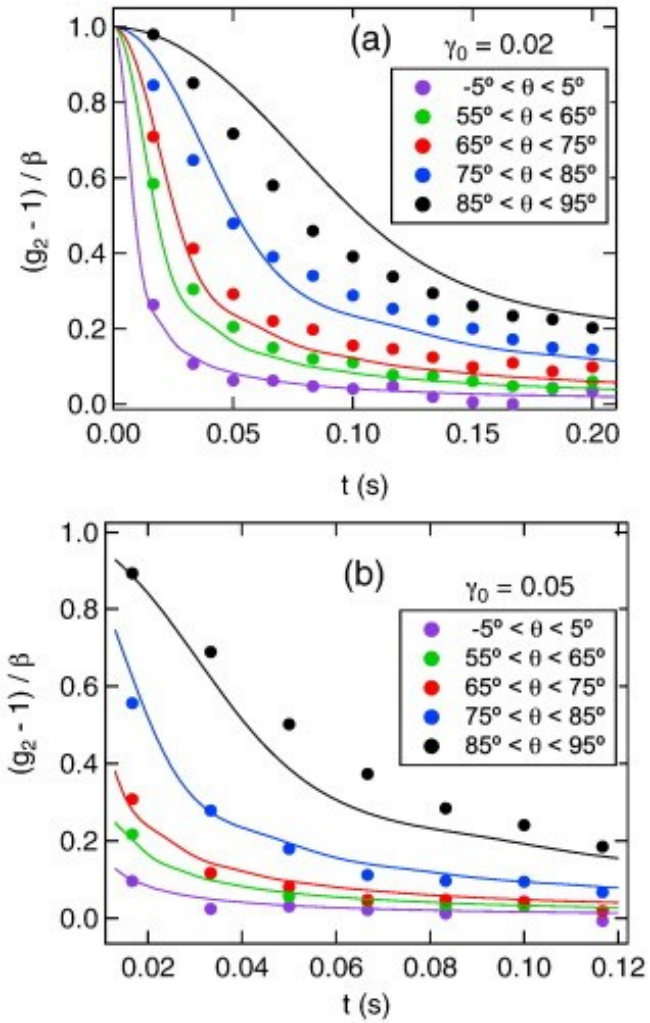

Figure 5.9: XPCS intensity autocorrelation function measured on a dilute colloidal suspension in viscous polyglycerol undergoing in situ oscillatory shear strain with ω = 2 s^{-1} at (a) γ_0 = 0.02 and (b) γ_0 = 0.05. Results are shown at wave-vector magnitude q = 0.024 nm^{-1} at varying ranges of angle θ between q and the flow direction, $q_{\parallel} = q\cos\theta$. The solid lines are the results of calculations based on Eq (5.16) and are compared with the data using no free parameters. (The sample thickness was H= 500 μm.)

delay times. The correlation function is shown for a single wave-vector magnitude, $q = 0.024\, nm^{-1}$, over varying ranges of angle θ between q and the flow direction ($q_{\|} = qcos\theta$). The solid lines in the figure are the results of calculations using Eq (5.6) and are compared with the data using no free parameters. The calculated lineshapes correspond closely to the data except at wave vectors close to the vorticity direction ($\theta \approx 90^{\circ}$). These discrepancies are not surprising since near the vorticity direction the transit and shear terms have comparable decay rates, making the validity of their factorization questionable. Also, near the vorticity direction the comparison between calculated and measured lineshapes is particularly sensitive to any misalignments that introduce uncertainty in θ. These issues aside, the otherwise good agreement between the calculated and measured lineshapes in Fig. 5.9 indicates that the XPCS correlation functions can accurately assess the deformation of materials during LAOS when the strain is affine.

A scientifically more interesting measurement is in which this agreement breaks down, thereby providing a microscopic perspective on nonaffine shear response. As an illustration of such a break down, Fig. 5.10 displays $g_2(\boldsymbol{q}, t)$ from a measurement on the same concentrated nanocolloidal gel as in the experiment described above during *in situ* oscillatory shear strain. In the measurement the detector frame rate, 60 fps, was much higher than the oscillation frequency, $\nu \approx 0.136$ Hz, to assure good temporal resolution. The strain amplitude, $\gamma_0 = 0.01$, was in the regime below the yield point where the echo peaks showed negligible attenuation but where the macroscopic rheology showed strain softening and enhanced dissipation. The wave-vector magnitude, $q = 0.2\, nm^{-1}$, was near the gel's structure factor peak, and hence the scale of the motions being probed was

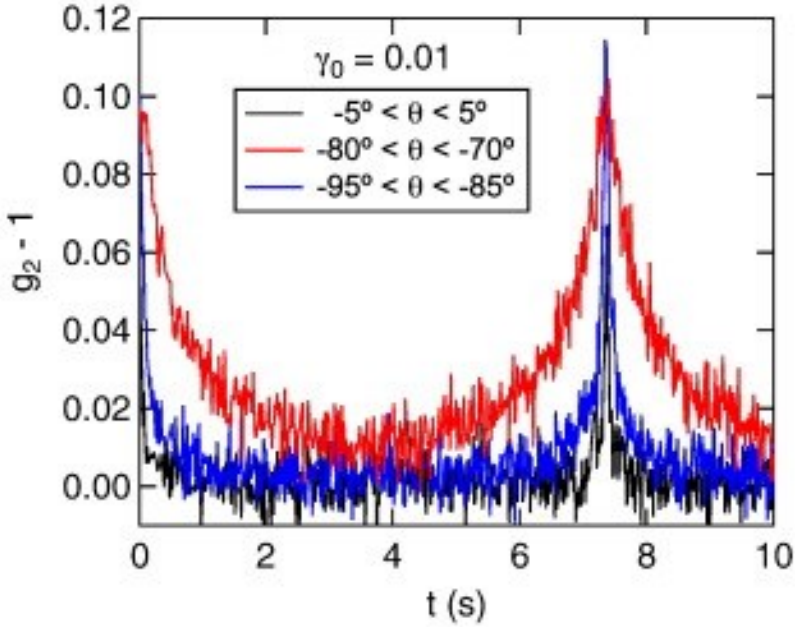

Figure 5.10: XPCS intensity autocorrelation function measured on a concentrated nanocolloidal gel undergoing in situ oscillatory shear strain with γ_0 = 0.01 and ω = 0.85 s^{-1}. Results are shown at q = 0.2 nm^{-1}, a wave-vector near interparticle structure factor peak, over three different ranges of angle θ between q and the flow direction as indicated in the legend.

on the order of the interparticle spacing. Unlike with affine deformations, where echo peaks broaden as the angle θ between the wave vector and the flow direction increases (and hence $q_{\|}$ decreases), in Fig. 5.10 the echo peak is broadest at an oblique angle, $\theta \approx 70^{\circ}$, indicating a nonaffine distortion. Such behavior in the concentrated gel is perhaps not surprising since particle interactions likely prevent perfectly affine strain at these length scales. However, as Fig. 5.10 illustrates, XPCS with LAOS can provide information about these distortions in nanostructured soft materials at the particle scale, which with appropriate modeling could lead to quantitative insight into the microscopic origins of their nonlinear rheology.

5.5 Conclusion

In conclusion, measurements of the XPCS echo peaks on a concentrated colloidal gel under oscillatory shear reveal a threshold strain for irreversible particle rearrangements that is near a (first) local maximum in the elastic stress, a signature of a yield point in gel rheology. The gel also displays strain softening well below this threshold, indicating a range of strains at which the rheology is nonlinear but the microscopic deformations are reversible. This behavior has been noted previously in repulsive systems and now this result generalizes it to systems with attractive particle interactions. Further, the wave-vector dependence of the XPCS echoes not only demonstrates that nanocolloidal gels undergo a nonequilibrium critical transition at yielding, but also uniquely provides direct characterization of the spatial-size distribution of the critical events on a nanometer scale. An interesting future experiment would obtain

both exponents ξ and τ on the same system to test the scaling between the energy and spatial size of plastic events.

Another challenge for rheo-XPCS concerns measurements incorporating LAOS. As the work described in section 5.4.3 above illustrates, XPCS with in situ LAOS can uncover the microscopic features of nonaffine deformations associated with nonlinear rheology. However, quantitative understanding of such results, like those illustrated in Fig. 5.7, will require the development of approaches for modeling the echo lineshapes. A potentially fruitful strategy that could deepen the interpretation of LAOS and other rheo-XPCS measurements would be to incorporate cross correlation analysis of speckle patterns that quantify not only time correlations of the intensity at fixed q but also time correlations between intensities at different wave vectors [171,172]. In the case of materials under in situ deformation and flow, the structural distortions associated with strain can be expressed as a continuous transformation of points in reciprocal space [54] that should have signatures in the time-dependent speckle pattern that such cross-correlation methods could capture.

More generally, the wealth of nanostructured soft solids with pronounced nonlinear rheology that are amenable to interrogation via XPCS with *in situ* shear should make further application of x-ray speckle echo an important tool for this field. Indeed, beyond accessing structural dynamics at nanometer scales, other demonstrated advantages of XPCS, such as the abilities to measure opaque samples and to interrogate heterogeneous dynamics with micrometer-sized beams, should have particular value in probing nonlinear structural response of soft materials under shear.

Bibliography

[1] P. G. de Gennes and J. Prost, *The physics of liquid crystals*. Clarendon Press, Oxford Press, 1993.

[2] S. P. Meeker, W. C. K. P., J. Crain, and E. M. Terentjev. "Colloid-liquid-crystal composites: an unusual soft solid". *Phys. Rev. E* **61** (6): R6083-R6086, 2000.

[3] D. Demus, J. Goodby, G. W. Gray, H. W. Piess, and V. Vill, *Physical Properties of Liquid Crystals*. Wiley-VCH, 1999.

[4] C. Fan, and M. J. Stephen, "Isotropic-nematic phase transition in liquid crystals". *Phys. Rev. L* **25** (8): pp 500-503, 1970

[5] M. Ginovska, H. Kresse, D. Bauman, G. Czechowski, and J. Jadzyn. "Static and dynamic dielectric behavior of mesogenic compunds of different polarity in the vicinity of the isotropic to nematic phase transition". *Phys. Rev. E* **69**, 022701, 2004.

[6] B. V. Roie, J. Leys, K. Denolf, C. Glorieux, G. Pitsi, and J. Thoen. "Weakly first-order character of the nematic-isotropic phase transition in liuqid crystals". *Phys. Rev. E* **72**, 041702, 2005.

[7] A. Sanchez-Castillo, M. A. Osipov, and F. Gieselmann. "Orientational order parameters in liquid crystals: A comparative study of x-ray diffraction and polarized Raman spectroscopy results". *Phys. Rev. E* **81**, 021707, 2010.

[8] N. Vieweg, C. Jansen, M. K. Shakfa, M. Scheller, N. Krumbholz, R. Wilk, M. Mikulics, and M. Koch. "Molecular properties of liquid crystals in the terahertz frequency range". *Optics Express* **18** (6): pp 6097-6107, 2010.

[9] T. Ishikawa, and O. D. Lavrentovich. “Dislocation profile in cholesteric finger texture”. *Phys. Rev. E* **60** (5): R5037-R5039, 1999.

[10] F. C. Frank. “I. Liquid crystals: On the theory of liquid crystals”. *Discuss. Faraday Soc.* **25**: pp 19-28, 1958

[11] R. G. Priest. “Theory of the Frank elastic constants of nematics liquid crystals”. *Phys. Rev. A* **7** (2): pp 720-729, 1973.

[12] G. Barbero, A. Sparavigna and A. Strigazzi. “The structure of the distortion free-energy density in nematics: second-order elasticity and surface terms”. *Il Nuovo Cimento D* **12** (9): pp 1259-1272, 1990.

[13] M.J. Bradshaw, E.P. Raynes, J.D. Bunning, T.E. Faber. “The Frank constants of some nematic liquid crystals”. *Journal de Physique*, **46** (9): pp.1513-1520, 1985.

[14] B. Jerome. “Surface effects and anchoring in liquid crystals”. *Rep. Prog. Phys*. **54**: pp 391-451, 1991.

[15] J. Nehring, A. R. Kmetz, and T. J. Scheffer. “Analysis of weak-boundary-coupling effects in liquid-crystal displays”. *Journal of Applied Physics* **47** (3): pp 850-857, 1976.

[16] M. Kleman. “Defects in liquid crystals”. *Rep. Prog. Phys.* **52**: pp 555-654, 1989.

[17] M. Kleman and O. D. Lavrentovich. *Soft Matter Physics: An Introduction (Partially Ordered Systems).* Springer, New York, 2003.

[18] N. Schopohl, and T. J. Sluckin. “Defect core structure in nematic liquid crystals”. *Phys. Rev. L* **59** (22): pp 2582-2584, 1987.

[19] N. J. Mottram & T. J. Sluckin. “Defect-induced melting in nematic liquid crystals”. *Liquid Crystals*, **27** (10): pp 1301-1304, 2000.

[20] H. Stark. “Physics of colloidal dispersions in nematic liquid crystals”. *Physics Reports* **351** (6): pp 387-474, 2001.

[21] M. Kleman, and O. D. Lavrentovich. “Topological point defects in nematic liquid crystals”. *Philosophical Magazine*, **86** (25-26): pp 4117-4137, 2006.

[22] E. M. Terentjev. “Disclination loops, standing alone and around solid particles, in nematics liquid crystals”. *Phys. Rev. E* **51** (2): pp 1330-1338, 1995.

[23] M. Tasinkevych, N. M. Silvestre and M. M. Telo da Gama. “Liquid crystal boojum-colloids“. *New J. Phys.* **14**, 073030, 2012.

[24] J. B. Rovner, C. P. Lapointe, D. H. Reich and R. L. Leheny. “Anisotropic stokes drag and dynamic lift on cylindrical colloids in a nematic liquid crystal” *Phys. Rev. L*, **105**, 228301, 2010.

[25] M. Miesowicz. “The three coefficents of viscosity of anisotropic liquids”. *Nature* **158**: pp 27, 1946.

[26] J. A. Janik. “PROFESSOR MARIAN MIESOWICZ, 1907–1992: A Scientific Appreciation”. *Liquid Crystals Today*, **2** (2): pp 6-6, 1992.

[27] A. G. Chmielewshi. “Viscosity coefficients of some nematic liquid crystals”. *Mol. Cryst. Liq. Cryst.*, **132** (3-4): pp 339-352, 1986.

[28] J. Happel, and H. Brenner. *Low Reynolds Number Hydrodynamics*. Klüwer, Dordrecht, Netherlands, 1991.

[29] J. L. Ericksen. “Anisotropic fluids”. *Arch. Rational Mech. Anal.,* **4** (231), 1959.

[30] J. L. Ericksen. “Inequalities in Liquid Crystal Theory”. *Physics of Fluids* **9**: pp 1205-1027, 1966.

[31] F. M. Leslie, “Some constitutive equations for anisotropic fluids”. *Quart. J. Mech. Appl. Math.,* **19**: pp 357-370, 1966

[32] F. M. Leslie, “Some constitutive equations for liquid crystals”. *Arch*. *Rational Mech. Anal*., ***28***: pp *265-283, 1968.*

[33] J. C. Loudet, P. Hanusse, and P. Poulin. “Stokes drag on a sphere in a nematic liquid crystal”. *Science* **306** (5701): pp 1525, 2004.

[34] J. B. Rovner, D. H. Reich and R. L. Leheny. “Anistropic Stokes Drag and Dynamics Lift on Spheres Sedimenting in a Nematic Liquid Crystal”. *Langmuir* **29** (7): pp 2104-2107, 2013.

[35] R. W. Ruhwandl and E. M. Terentjev. “Friction drag on a particle moving in a nematic liquid crystal”. *Phys. Rev. E* **54** (5): pp 5204-5210, 1996.

[36] Mewis, J. and N. J. Wagner. *Colloidal Suspension Rheology*. New York, Cambridge University Press, 2012.

[37] Larson, R. G. *The Strucure and Rheology of Complex Fluids.* New York, Oxford University Press, 1999.

[38] E. Zaccarelli. “Colloidal gels: equilibrium and non-equilibrium routes”. *J. Phys. Condens. Matter* **19**, 323101, 2007.

[39] V. Trappe and P. Sandkühler. “Colloidal gels—low-density disordered solid-like states”. *Curr. Opin. Colloid Interface Sci*. **8**, 494, 2004.

[40] T. Vicsek. *Fractal Growth Phenomena*. World Scientific, Singapore, 1992.

[41] K. Dawson, G. Foffi, M. Fuchs, W. Götze, F. Sciortino, M. Sperl, P. Tartaglia, T. Voigtmann, and E. Zaccarelli. “Higher-order glass-transition singularities in colloidal systems with attractive interactions”. *Phys. Rev. E* **63**, 011401, 2000.

[42] K. N. Pham, A. M. Puertas, J. Bergenholtz, S. U. Egelhaaf, A. Moussaïd, P. N. Pusey, A. B. Schofield, M. E. Cates, M. Fuchs, and W. C. K. Poon. "Multiple Glassy States in a Simple Model System". *Science* **296**, 104, 2002.

[43] T. Eckert and E. Bartsch. "Re-entrant Glass Transition in a Colloid-Polymer Mixture with Depletion Attractions". *Phys. Rev. Lett*. **89**, 125701, 2002 .

[44] X. Lu, S. G.J. Mochrie, S. Narayanan, A. R. Sandy, and M. Sprung. "How a Liquid Becomes a Glass Both on Cooling and on Heating". *Phys. Rev. Lett*. **100**, 045701, 2008.

[45] E. Zaccarelli and W. C. K. Poon. "Colloidal glasses and gels: The interplay of bonding and caging". *Proc. Natl. Acad. Sci. U.S.A*. **106**, 15203, 2009.

[46] Y. Mao, M. E. Cates, H. N. W. Lekkerkerker. "Depletion force in colloidal systems". *Physica A* **222** (1-4): pp 10-24, 1995.

[47] A. P. Deshpande, J. M. Krishnan, and P. B. Sunil Kumar. *Rheology of complex fluids.* Springer, 2010.

[48] R. G. Larson. *The Structure and Rheology of Complex Fluids*. Oxford University Press, 1999.

[49] B. E. Warren. *X-ray Diffraction*. Dover, 1990.

[50] J. C. Dainty. *Laser Speckle and Related Phenomena*. Springer, 1975.

[51] G. Grübel, A. Madsen, A. Robert. Chapter 18 in *Soft Matter Characterization*. Springer, 2008.

[52] R. L. Leheny. "XPCS: nanoscale motion and rheology". *Curr. Opin. Colloid Interface Sci.* **17**: pp 3–12, 2012.

[53] N. A. Dudokovic, C. F. Zukoski. "Nanoscale dynamics and aging of fibrous peptide-based gels". *J Chem Phys* **141**, 164905, 2014.

[54] G. G. Fuller, J. M. Rallison, R. L. Schmidt, L. G. Leal. "The measurement of velocity gradients in laminar flow by homodyne light-scattering spectroscopy". *J Fluid Mech* **100**: pp 555–75, 1980.

[55] B. J. Ackerson, N. A. Clark. "Dynamic light scattering at low rates of shear". *J Phys France* **42**: pp 929–36, 1981.

[56] W. R. Burghardt, M. Sikorski, A. R. Sandy, S. Narayanan. "X-ray photon correlation spectroscopy during homogenous shear flow". *Phys Rev E* **85**, 021402, 2012.

[57] H. Stark and D. Ventzki. "Non-linear Stokes drag of spherical particles in a nematic solvent". *Europhys. Lett,* **57**: pp 60–66, 2002.

[58] O. D. Lavrentovich, "Transport of particles in liquid crystals". *Soft Matter* **10**: pp 1264-1283, 2014.

[59] T. Turiv, I. Lazo, A. Brodin, B. I. Lev, V. Reiffenrath, V. G. Nazarenko and O. D. Lavrentovich, "Effect of Collective Molecular Reorientations on Brownian Motion of Colloids in Nematic Liquid Crystal". *Science* **342**: pp 1351–1354, 2013.

[60] J. S. Lintuvuori, K. Stratford, M. E. Cates and D. Marenduzzo, "Colloids in Cholesterics: Size-Dependent Defects and Non-Stokesian Microrheology". *Phys. Rev. L*, **105**, 178302, 2010.

[61] M. Melle, S. Schlotthauer, C. K. Hall, E. Diaz-Herrera and M. Schoen. "Disclination lines at homogeneous and heterogeneous colloids immersed in a chiral liquid crystal". *Soft Matter* **10**: pp 5489–5502, 2014.

[62] M. C. M. Varney, Q. Zhang, M. Tasinkevych, N. M. Silvestre, K. A. Bertness and I. I. Smalyukh. "Periodic dynamics, localization metastability, and elastic interaction of colloidal particles with confining surfaces and helicoidal structure of cholesteric liquid

crystals". *Phys. Rev. E* **90**, 062502, 2014.

[63] I. I. Smalyukh, B. I. Senyuk, P. Palffy-Muhoray, O. D. Lavrentovich, H. Huang, E. C. Gartland, Jr., V. H. Bodnar, T. Kosa, and B. Taheri. "Electric-field-induced nematic cholesteric transition and three-dimensional director structures in homeotropic cells". *Phys. Rev. E* **72**, 061707, 2005.

[64] P. Oswald, J. Baudry, and S. Pirkl. "Static and dynamic properties of cholesteric fingers in electric field". *Physics Reports* **337**: pp 67-96, 2000.

[65] C. Lapointe, A. Hultgren, D. M. Silevitch, E. J. Felton, D. H. Reich and R. L. Leheny, "Elastic Torque and the Levitation of Metal Wires by a Nematic Liquid Crystal". *Science* **303**: pp 652–655, 2004.

[66] N. V. Madhusudana and R. Pratibha, "Elasticity and Orientational Order in Some Cyanobiphenyls: Part IV. Reanalysis of the Data". *Mol. Cryst. Liq. Cryst.* **89**: pp 249–257, 1982.

[67] O. P. Pishnyak, S. Tang, J. R. Kelly, S. V. Shiyanovskii and O. D. Lavrentovich, "Levitation, Lift, and Bidirectional Motion of Colloidal Particles in an Electrically Driven Nematic Liquid Crystal". *Phys. Rev. L* **99**, 127802, 2007.

[68] C. P. Lapointe, D. H. Reich and R. L. Leheny, "Manipulation and Organization of Ferromagnetic Nanowires by Patterned Nematic Liquid Crystals". *Langmuir* **24**: pp 11175–11181, 2008.

[69] A. Sengupta, C. Bahr and S. Herminghaus, "Topological microfluidics for flexible micro-cargo concepts". *Soft Matter* **9**: pp 7251–7260, 2013.

[70] D. Andrienko, M. P. Allen, G. Skacej and S. Zumer. “Defect structures and torque on an elongated colloidal particle immersed in a liquid crystal host”. *Phys. Rev. E*, **65** (4), 041702, 2002.

[71] Y. D. Gu, N. L. Abbott. “Observation of Saturn-ring defects around solid microspheres in nematic liquid crystals”. *Phys. Rev. Lett.* **85** (22): pp 4719-4722, 2000.

[72] F. R. Hung. “Quadrupolar particles in a nematic liquid crystal: Effects of particle size and shape”. *Phys. Rev. E* **79** (2), 021705, 2009.

[73] F. R. Hung, O. Guzman, B. T. Gettelfinger, N. L. Abbott and J. J. de Pablo. “Anisotropic nanoparticles immersed in a nematic liquid crystal: Defect structures and potentials of mean force”. *Phys. Rev. E*, **74** (1), 011711, 2006.

[74] C. P. Lapointe, T. G. Mason and I. Smalyukh. “Shape-Controlled Colloidal Interactions in Nematic Liquid Crystals”. *Science* **326** (5956): pp 1083-1086, 2009.

[75] T. C. Lubensky, D. Pettey, N. Currier and H. Stark. “Topological defects and interactions in nematic emulsions”. *Phys. Rev. E* **57** (1): pp 610-625, 1998.

[76] J. B. Rovner, D. S. Borgnia, D. H. Reich and R. L. Leheny. “Elastic and hydrodynamic torques on a colloidal disk within a nematic liquid crystal”. *Phys. Rev. E* **86**, 041702, 2012.

[77] C. Lapointe, N. Cappallo, D. H. Reich and R. L Leheny. “Static and dynamic properties of magnetic nanowires in nematic fluids (invited)”. *J. Appl. Phys*.**97** (10), 10Q304, 2005.

[78] V. G. Nazarenko, A. B. Nych and B. I. Lev. “Crystal structure in nematic emulsion”. *Phys. Rev. Lett*. **87** (7), 075504, 2001.

[79] I. Musevic, M. Skarabot, U. Tkalec, M. Ravnik and S. Zumer. “Two-dimensional nematic colloidal crystals self-assembled by topological defects”. *Science* **313** (5789): pp 954-958, 2006.

[80] M. Skarabot, M. Ravnik, S. Zumer, U. Tkalec, I. Poberaj, D. Babic, N. Osterman and I. Musevic. “Two-dimensional dipolar nematic colloidal crystals”. *Phys. Rev. E* **76** (5), 051406, 2007.

[81] U. Ognysta, A. Nych, V. Nazarenko, I. Musevic, M. Skarabot, M. Ravnik, S. Zumer, I. Poberaj and D. Babic. “2D interactions and binary crystals of dipolar and quadrupolar nematic colloids”. *Phys. Rev. Lett.* **100** (21), 217803, 2008.

[82] O. D. Lavrentovich, I. Lazo and O. P. Pishnyak. “Nonlinear electrophoresis of dielectric and metal spheres in a nematic liquid crystal”. *Nature* **467** (7318): pp 947-950, 2010.

[83] S. Khullar, C. F. Zhou and J. J. Feng. “Dynamic evolution of topological defects around drops and bubbles rising in a nematic liquid crystal”. *Phys. Rev. Lett.* **99** (23), 237802, 2007.

[84] C. P. Lapointe, S. Hopkins, T. G. Mason and I. I. Smalyukh. “Electrically Driven Multiaxis Rotational Dynamics of Colloidal Platelets in Nematic Liquid Crystals”. *Phys. Rev. Lett.* **105** (17), 178301, 2010.

[85] O. P. Pishnyak, S. V. Shiyanovskii and O. D. Lavrentovich. “Inelastic Collisions and Anisotropic Aggregation of Particles in a Nematic Collider Driven by Backflow”. *Phys. Rev. Lett.* **106** (4), 047801, 2011.

[86] B. T. Gettelfinger, J. A. Moreno-Razo, G. M. Koenig, J. P. Hernandez-Ortiz, N. L. Abbott and J. J. de Pablo. “Flow induced deformation of defects around nanoparticles and nanodroplets suspended in liquid crystals”. *Soft Matter* **6** (5): pp 896-901, 2010.

[87] A. Jakli, B. Senyuk, G. Liao and O. D. Lavrentovich. “Colloidal micromotor in smectic A liquid crystal driven by DC electric field”. *Soft Matter* **4** (12): pp 2471-2474, 2008.

[88] I. Lazo and O. D. Lavrentovich. “Liquid-crystal-enabled electrophoresis of spheres in a nematic medium with negative dielectric anisotropy”. *Philosophical Transactions of the Royal Society of London A: Mathematical, Physical and Engineering Sciences* **371** (1988), 2013.

[89] M. Škarabot, Ž. Lokar and I. Muševič. “Transport of particles by a thermally induced gradient of the order parameter in nematic liquid crystals”. *Phys. Rev. E* **87** (6), 062501, 2013.

[90] G. Foffano, J. S. Lintuvuori, A. Tiribocchi and D. Marenduzzo. “The dynamics of colloidal intrusions in liquid crystals: a simulation perspective”. *Liquid Crystals Reviews* **2** (1): pp 1-27, 2014.

[91] Y. Sasaki, Y. Takikawa, V. S. R. Jampani, H. Hoshikawa, T. Seto, C. Bahr, S. Herminghaus, Y. Hidaka and H. Orihara. “Colloidal caterpillars for cargo transportation”. *Soft Matter* **10** (44): pp 8813-8820, 2014.

[92] S. Hernàndez-Navarro, P. Tierno, J. A. Farrera, J. Ignés-Mullol and F. Sagués. “Reconfigurable Swarms of Nematic Colloids Controlled by Photoactivated Surface Patterns”. *Angew. Chem* **126** (40): pp 10872-10876, 2014.

[93] A. Eremin, P. Hirankittiwong, N. Chattham, H. Nádasi, R. Stannarius, J. Limtrakul, O. Haba, K. Yonetake and H. Takezoe. “Optically driven translational and rotational motions of microrod particles in a nematic liquid crystal”. *Proceedings of the National Academy of Sciences* **112** (6), 1716-1720, 2015.

[94] B. Senyuk, D. Glugla, I. I. Smalyukh. “Rotational and translational diffusion of anisotropic gold nanoparticles in liquid crystals controlled by varying surface anchoring”. *Phys. Rev. E* **88** (6), 062507, 2013.

[95] M. C. M. Varney, Q. Zhang and I. I. Smalyukh. “Stick-slip motion of surface point defects prompted by magnetically controlled colloidal-particle dynamics in nematic liquid crystals”. *Phys. Rev. E* **91** (5), 052503, 2015.

[96] N. M. Silvestre, P. Patricio and M. M. T. da Gama. “Key-lock mechanism in nematic colloidal dispersions”. *Phys. Rev. E* **69** (6), 061402, 2004.

[97] F. R. Hung, B. T. Gettelfinger, G. M. Koenig, N. L. Abbott and J. J. de Pablo. “Nanoparticles in nematic liquid crystals: Interactions with nanochannels”. *J. Chem. Phys.* **127** (12), 124702, 2007.

[98] M. Rahimi, T. F. Roberts, J. C. Armas-Pérez, X. Wang, E. Bukusoglu, N. L. Abbott and J. J. de Pablo. “Nanoparticle self-assembly at the interface of liquid crystal droplets”. *Proceedings of the National Academy of Sciences* **112** (17): pp 5297-5302, 2005.

[99] J. K. Whitmer, X. Wang, F. Mondiot, D. S. Miller, N. L. Abbott and J. J. de Pablo. “Nematic-Field-Driven Positioning of Particles in Liquid Crystal Droplets”. *Phys. Rev. Lett.* **111** (22), 227801, 2013.

[100] J. Han and H. G. Craighead. “Separation of Long DNA Molecules in a Microfabricated Entropic Trap Array”. *Science* **288** (5468): pp 1026-1029, 2000.

[101] M. Cavallaro, Jr., M. A. Gharbi1, D. A. Beller, S. Cˇopar, Z. Shi, T. Baumgart, S. Yang, R. D. Kamien, and K. J. Stebe. “Exploiting imperfections in the bulk to direct assembly of surface colloids”. *PNAS* **110**: pp 18804-18808, 2013.

[102] M. Gu, I. I. Smalyukh and O. D. Lavrentovich. “Directed vertical alignment liquid crystal display with fast switching”. Appl. Phys. L. 88 (6), 2005.

[103] K. Chen, L. P. Metcalf, D. P. Rivas, D. H. Reich and R. L. Leheny. “Anisotropic colloidal transport and periodic stick-slip motion in cholesteric finger textures”. Soft Matter 11, 4189, 2015

[104] L. R. Huang, E. C. Cox, R. H. Austin and J. C. Sturm. “Continuous Particle Separation Through Deterministic Lateral Displacement”. *Science* **304** (5673): pp 987-990, 2004.

[105] P. T. Korda, M. B. Taylor and D. G. Grier. “Kinetically Locked-In Colloidal Transport in an Array of Optical Tweezers”. *Phys. Rev. Lett.* **89** (12), 128301, 2002.

[106] M. P. MacDonald, G. C. Spalding and K. Dholakia. “Microfluidic sorting in an optical lattice”. *Nature* **426** (6965): pp 421-424, 2003.

[107] D. W. Inglis, K. L. Morton, J. A. Davis, T. J. Zieziulewicz, D. A. Lawrence, R. H. Austin and J. C. Sturm. “Microfluidic device for label-free measurement of platelet activation”. *Lab on a Chip* **8** (6): pp 925-931, 2008.

[108] A. M. Lacasta, J. M. Sancho, A. H. Romero and K. Lindenberg. “Sorting on Periodic Surfaces”. *Phys. Rev. Lett.* **94** (16), 160601, 2005.

[109] A. Gopinathan and D. G. Grier. “Statistically Locked-In Transport through Periodic Potential Landscapes”. *Phys. Rev. Lett.* **92** (13), 130602, 2004.

[110] J. P. Gleghorn, J. P. Smith and B. J. Kirby. “Transport and collision dynamics in periodic asymmetric obstacle arrays: Rational design of microfluidic rare-cell immunocapture devices”. *Phys. Rev. E* **88** (3), 032136, 2013.

[111] J. D. P. Thomas and K. D. Dorfman. “Tilted post arrays for separating long DNA”. *Biomicrofluidics* **8** (3), 034115, 2014.

[112] S. R. Risbud and G. Drazer. “Directional locking in deterministic lateral-displacement microfluidic separation systems”. *Phys. Rev. E* **90** (1), 012302, 2014.

[113] M. Balvin, E. Sohn, T. Iracki, G. Drazer and J. Frechette. “Directional Locking and the Role of Irreversible Interactions in Deterministic Hydrodynamics Separations in Microfluidic Devices”. *Phys. Rev. Lett.* **103** (7), 078301, 2009.

[114] T. Bowman, J. Frechette and G. Drazer. “Force driven separation of drops by deterministic lateral displacement”. *Lab on a Chip* **12** (16): pp 2903-2908, 2012.

[115] J. Herrmann, M. Karweit and G. Drazer. “Separation of suspended particles in microfluidic systems by directional locking in periodic fields”. *Phys. Rev. E* **79** (6), 061404, 2009.

[116] R. Devendra and G. Drazer. “Gravity Driven Deterministic Lateral Displacement for Particle Separation in Microfluidic Devices”. *Anal. Chem.* **84** (24): pp 10621-10627, 2012.

[117] Z. Li and G. Drazer. “Separation of Suspended Particles by Arrays of Obstacles in Microfluidic Devices”. *Phys. Rev. Lett.* **98** (5), 050602, 2007.

[118] C. F. Chou, O. Bakajin, S. W. P. Turner, T. A. J. Duke, S. S. Chan, E. C. Cox, H. G. Craighead, R. H. Austin. “Sorting by diffusion: An asymmetric obstacle course for continuous molecular separation”. *Proceedings of the National Academy of Sciences* **96** (24), 13762-13765, 1999.

[119] M. L. Falk and J. Langer. “Deformation and failure of amorphous, solidlike materials”. *Annu. Rev. Condens. Matter Phys.* **2**, 353, 2011.

[120] N. C. Keim and P. E. Arratia. “Mechanical and Microscopic Properties of the Reversible Plastic Regime in a 2D Jammed Material”. *Phys. Rev. L* **112**, 028302, 2014.

[121] N. V. Priezjev. “Heterogeneous relaxation dynamics in amorphous materials under cyclic loading”. *Phys. Rev. E* **87**, 052302, 2013.

[122] D. Fiocco, G. Foffi, and S. Sastry. “Oscillatory athermal quasistatic deformation of a model glass”. *Phys. Rev. E* **88**, 020301, 2013.

[123] R. G. Egres, F. Nettesheim, and N. J. Wagner. “Rheo-SANS investigation of acicular-precipitated calcium carbonate colloidal suspensions through the shear thickening transition”. *J. Rheol.* **50**, 685, 2006.

[124] I. Bihannic, C. Baravian, J. F. L. Duval, E. Paineau, F. Meneau, P. Levitz, J. P. de Silva, P. Davidson, and L. J. Michot, “Orientational Order of Colloidal Disk-Shaped Particles under Shear-Flow Conditions: a Rheological−Small-Angle X-ray Scattering Study”. *J. Phys. Chem. B* **114**, 16347, 2010.

[125] M. P. Lettinga, P. Holmqvist, P. Ballesta, S. Rogers, D. Kleshchanok, and B. Struth. “Nonlinear Behavior of Nematic Platelet Dispersions in Shear Flow”. *Phys. Rev. Lett.* **109**, 246001, 2012.

[126] C. R. L´opez-Barr´on,L.Porcar, A. P. R. Eberle, andN. J.Wagner. “Dynamics of Melting and Recrystallization in a Polymeric Micellar Crystal Subjected to Large Amplitude Oscillatory Shear Flow”. *Phys. Rev. Lett.* **108**, 258301, 2012.

[127] A. M. Philippe, C. Baravian, M. Jenny, F. Meneau, and L. J. Michot. “Taylor-Couette Instability in Anisotropic Clay Suspensions Measured Using Small-Angle X-ray Scattering”. *Phys. Rev. Lett.* **108,** 254501, 2012.

[128] F. E. Caputo, W. R. Burghardt, K. Krishnan, F. S. Bates, and T. P. Lodge. “Time-resolved small-angle x-ray scattering measurements of a polymer bicontinuous microemulsion structure factor under shear”. *Phys. Rev. E* **66**, 041401, 2002.

[129] L. M. C. Dykes, J. M. Torkelson, and W. R. Burghardt. “Shear-Induced Orientation in Well-Exfoliated Polystyrene/Clay Nanocomposites”. *Macromolecules* **45**, 1622, 2012.

[130] A. P. R. Eberle, N. Martys, L. Porcar, S. R. Kline,W. L. George, J. M. Kim, P. D. Butler, and N. J. Wagner. “Shear viscosity and structural scalings in model adhesive hard-sphere gels”. *Phys. Rev. E* **89**, 050302, 2014.

[131] J. Min Kim, A. P. R. Eberle, A. Kate Gurnon, L. Porcar, and N. J. Wagner. “The microstructure and rheology of a model, thixotropic nanoparticle gel under steady shear and large amplitude oscillatory shear (LAOS)”. *J. Rheol.* **58**, 1301, 2014.

[132] J. Kim, D. Merger, M. Wilhelm, and M. E. Helgeson. “Microstructure and nonlinear signatures of yielding in a heterogeneous colloidal gel under large amplitude oscillatory shear ”. *J. Rheol.* **58**, 1359, 2014.

[133] P. Varadan and M. J. Solomon. “Shear-Induced Microstructural Evolution of a Thermoreversible Colloidal Gel”. *Langmuir* **17**, 2918, 2001.

[134] H. Hoekstra, J. Mewis, T. Narayanan, and J. Vermant. “Multi Length Scale Analysis of the Microstructure in Sticky Sphere Dispersions during Shear Flow”. *Langmuir* **21**, 11017, 2005.

[135] P. H´ebraud, F. Lequeux, J. P. Munch, and D. J. Pine. “Yielding and Rearrangements in Disordered Emulsions”. *Phys. Rev. Lett,* **78**, 4657, 1997.

[136] R. H¨ohler, S. Cohen-Addad, and H. Hoballah. “Periodic Nonlinear Bubble Motion in Aqueous Foam under Oscillating Shear Strain”. *Phys. Rev. Lett.* **79**, 1154, 1997.

[137] G. Petekidis, A. Moussa¨ıd, and P. N. Pusey. “Rearrangements in hard-sphere glasses under oscillatory shear strain”. *Phys. Rev. E* **66**, 051402, 2002.

[138] V. Viasnoff and F. Lequeux. “Aging and effective delays in colloidal glasses under shear”. arXiv:cond-mat/0305389.

[139] P. A. Smith, G. Petekidis, S. U. Egelhaaf, and W. C. K. Poon. “Yielding and crystallization of colloidal gels under oscillatory shear”. *Phys. Rev. E* **76**, 041402, 2007.

[140] M. Laurati, S. U. Egelhaaf, and G. Petekidis. “Plastic rearrangements in colloidal gels investigated by LAOS and LS-Echo”. *J. Rheol.* **58**, 1395, 2014.

[141] A. P. R. Eberle, R. Casta˜neda-Priego, J. M. Kim, and N. J. Wagner. “Dynamical Arrest, Percolation, Gelation, and Glass Formation in Model Nanoparticle Dispersions with Thermoreversible Adhesive Interactions”. *Langmuir* **28**, 1866 2012.

[142] S. A. Shah, Y.-L. Chen, K. S. Schweizer, and C. F. Zukoski. “Viscoelasticity and rheology of depletion flocculated gels and fluids”. *J. Chem. Phys.* **119**, 8747, 2003.

[143] S. A. Shah, Y.-L. Chen, S. Ramakrishnan, K. S. Schweizer, and C. F. Zukoski. “Microstructure of dense colloid–polymer suspensions and gels”. *J. Phys.: Condens. Matter* **15**, 4751, 2003.

[144] S. Ramakrishnan, Y.-L. Chen, K. S. Schweizer, and C. F. Zukoski. “Elasticity and clustering in concentrated depletion gels”. *Phys. Rev. E* **70**, 040401, 2004.

[145] B. Chung, S. Ramakrishnan, R. Bandyopadhyay, D. Liang, C. F. Zukoski, J. L. Harden, and R. L. Leheny. “Microscopic Dynamics of Recovery in Sheared Depletion Gels”. *Phys. Rev. Lett.* **96**, 228301, 2006.

[146] M. Laurati, S. U. Egelhaaf, and G. Petekidis. “Nonlinear rheology of colloidal gels with intermediate volume fraction”. *J. Rheol.* **55**, 673, 2011.

[147] K. N. Pham, G. Petekidis, D. Vlassopoulos, S. U. Egelhaaf, W. C. K. Poon, and P. N. Pusey. “Yielding behavior of repulsion- and attraction-dominated colloidal glasses”. *J. Rheol.* **52**, 649, 2008.

[148] N. Koumakis and G. Petekidis. “Two step yielding in attractive colloids: transition from gels to attractive glasses”. *Soft Matter* **7**, 2456, 2011.

[149] S. Ramakrishnan, V. Gopalakrishnan, and C. F. Zukoski. “Clustering and Mechanics in Dense Depletion and Thermal Gels”. *Langmuir* **21**, 9917, 2005.

[150] D. Doraiswamy, A. N. Mujumdar, I. Tsao, A. N. Beris, S. C. Danforth, and A. B. Metzner. “The Cox–Merz rule extended: a rheological model for concentrated suspensions and other materials with a yield stress”. *J. Rheol.* **35**, 647, 1991.

[151] J.-P. Bouchaud and E. Pitard. “Anomalous dynamical light scattering in soft glassy gels”. *Eur. Phys. J. E* **6**, 231, 2001.

[152] L. Cipelletti, L. Ramos, S. Manley, E. Pitard, D. A. Weitz, E. E. Pashkovski, and M. Johansson. “Universal non-diffusive slow dynamics in aging soft matter”. *Faraday Discuss.* **123**, 237, 2003.

[153] A. Madsen, R. L. Leheny, H. Guo, M. Sprung, and O. Czakkel. "Beyond simple exponential correlation functions and equilibrium dynamics in x-ray photon correlation spectroscopy". *New J. Phys.* **12**, 055001, 2010.

[154] L. Mohan, R. T. Bonnecaze, and M. Cloitre. "Microscopic Origin of Internal Stresses in Jammed Soft Particle Suspensions". *Phys. Rev. Lett.* **111**, 268301, 2013.

[155] A. Fluerasu, P. Kwasniewski, C. Caronna, F. Destremaut, J.-B. Salmon, and A. Madsen. "Dynamics and rheology under continuous shear flow studied by x-ray photon correlation spectroscopy". *New J. Phys.* **12**, 035023, 2010.

[156] S. Slotterback, M. Mailman, K. Ronaszegi, M. van Hecke, M. Girvan, and W. Losert. "Onset of irreversibility in cyclic shear of granular packings". *Phys. Rev. E* **85**, 021309, 2012.

[157] I. Regev, T. Lookman, and C. Reichhardt. "Onset of irreversibility and chaos in amorphous solids under periodic shear". *Phys. Rev. E* **88**, 062401, 2013.

[158] K. Masschaele, J. Fransaer, and J. Vermant. "Direct visualization of yielding in model two-dimensional colloidal gels subjected to shear flow". *J. Rheol.* **53**, 1437, 2009.

[159] V. Kobelev and K. S. Schweizer. "Nonlinear elasticity and yielding of depletion gels". *J. Chem. Phys*. **123**, 164902, 2005.

[160] V. Gopalakrishnan and C. F. Zukoski. "Yielding Behavior of Thermo-reversible Colloidal Gels". *Langmuir* **23**, 8187, 2007.

[161] K. Miyazaki, D. R. Reichman, and R. Yamamoto. "Supercooled liquids under shear: Theory and simulation". *Phys. Rev. E* **70**, 011501, 2004.

[162] R. Besseling, E. R. Weeks, A. B. Schofield, and W. C. K. Poon. "Three-dimensional imaging of colloidal glasses under steady shear". *Phys. Rev. Lett.* **99**, 028301, 2007.

[163] F. Livet, F. Bley, F. Ehrburger-Dolle, I. Morfin, E. Geissler, and M. Sutton. "X-ray intensity fluctuation spectroscopy by heterodyne detection". *J. Synchrotron Radiat.* **13**, 453, 2006.

[164] N. P. Bailey, J. Schiøtz, A. Lemaˆıtre, and K.W. Jacobsen. "Avalanche size scaling in sheared three-dimensional amorphous solid". *Phys. Rev. Lett.* **98**, 095501, 2007.

[165] K. M. Salerno, C. E. Maloney, and M. O. Robbins. "Avalanches in strained amorphous solids: does inertia destroy critical behavior? ". *Phys. Rev. Lett.* **109**, 105703, 2012.

[166] M.-C. Miguel, A. Vespignani, S. Zapperi, J. Weiss, and J.-R. Grasso. "Intermittent dislocation flow in viscoplastic deformation". *Nature (London)* **410**, 667, 2001.

[167] D. M. Dimiduk, C. Woodward, R. LeSar, and M. D. Uchic. "Scale-free intermittent flow in crystal plasticity". *Science* **312**, 1188, 2006.

[168] M. Zaiser. "Scale invariance in plastic flow of crystalline solids". *Adv. Phys*. **55**, 185, 2006.

[169] G. Wang, K. Chan, L. Xia, P. Yu, J. Shen, and W. Wang. "Self-organized intermittent plastic flow in bulk metallic glasses". *Acta Mater.* **57**, 6146, 2009.

[170] B. A. Sun, H. B. Yu, W. Jiao, H. Y. Bai, D. Q. Zhao, and W. H. Wang. "Plasticity of ductile metallic glasses: A self-organized critical state". *Phys. Rev. Lett.* **105**, 035501, 2010.

[171] P. Wochner, C. Gutt, T. Autenrieth, T. Demmer, V. Bugaev, A. D. Ortiz, A. Duri,

F. Zontone, G. GrŸbel, H. Dosch. “X-ray cross correlation analysis uncovers hidden local symmetries in disordered matter”. *Proc Natl Acad Sci* **106**: pp 11511–4, 2009.

[172] R. P. Kurta, B. I. Ostrovskii, A. Singer, O. Y. Gorobtsov, A. Shabalin, D. Dzhigaev, O. M. Yefanov, A. V. Zozulya, M. Sprung, I. A. Vartanyants. “X-ray cross-correlation analysis of liquid crystal membranes in the vicinity of the hexatic–smectic phase transition”. *Phys. Rev. E* **88**, 044501,2013.

Vita

Kui Chen was born on March 21, 1990 in Suzhou, Anhui Province, China. He was admitted by University of Science and Technology of China in Hefei in 2007 and received BS degrees in Physics in 2011. In the same year he attended the Ph.D. program in Physics and Astronomy Department in Johns Hopkins University, focusing on the condensed matter field. In the following year, he began to study the colloidal transport in liquid crystals and rheology and dynamics of soft disordered solids under the supervision of Prof. Leheny.